TESIS DE LA UNIVERSIDAD DE ZARAGOZA

2014

18

Mauricio Yilmer Carmona García

Numerical Analysis of Melting and Holding Furnaces in Secondary Aluminum Production

Departamento
Instituto Universitario de Investigación Mixto CIRCE

Director/es
Cortés Gracia, Cristóbal

ISSN 2254-7606

Prensas de la Universidad
Universidad Zaragoza

Universidad Zaragoza
1542

Tesis Doctoral

NUMERICAL ANALYSIS OF MELTING AND HOLDING FURNACES IN SECONDARY ALUMINUM PRODUCTION

Autor

Mauricio Yilmer Carmona García

Director/es

Cortés Gracia, Cristóbal

UNIVERSIDAD DE ZARAGOZA

Instituto Universitario de Investigación Mixto CIRCE

2014

Ph.D. Thesis

NUMERICAL ANALYSIS OF MELTING AND HOLDING FURNACES IN SECONDARY ALUMINUM PRODUCTION

By Mauricio Yilmer Carmona García

January 2014

Advisor:

Cristóbal Cortés Gracia, Ph.D.

Instituto CIRCE

Escuela de Ingeniería y Arquitectura

Universidad de Zaragoza

Numerical analysis of melting and holding furnaces in secondary aluminum production

Mauricio Yilmer Carmona García

Thesis submitted in partial fulfillment of the requirements for the degree of Doctor of Philosophy

University of Zaragoza, Spain

Abstract

In this thesis, two different aluminum furnaces are analyzed numerically: 1) a new prototype of melting furnace; 2) a new prototype of holding furnace. These devices are a key factor in secondary aluminum production. Models used take into account heat conduction in solid parts, convection in air and molten aluminum, interactions between gas-liquid-solid zones, phase change of the load and radiation heat transfer. With the objective to develop a calculating tool to assist in the design and scaling-up of industrial furnaces, several calculation strategies are tested concerning their computational economy and their accuracy in computing different key parameters. Estimations of temperatures in furnaces are compared with experimental measurements taken in real prototypes in typical operation cycles.

Análisis numérico de hornos de fundición y mantenimiento en producción de aluminio secundario

Mauricio Yilmer Carmona García

Tesis realizada para cumplir con los requisitos del grado de Doctor

Universidad de Zaragoza, España

Resumen

En esta tesis, dos hornos de aluminio diferentes se analizan numéricamente: 1) un nuevo prototipo de horno de fundición; 2) un nuevo prototipo de horno de mantenimiento. Estos dispositivos son claves en la producción de aluminio secundario. Los modelos utilizados tienen en cuenta la conducción de calor en las partes sólidas, la convección en el aire y de aluminio fundido, las interacciones entre las zonas de gas-líquido-sólido, cambio de fase de la carga y la transferencia de calor por radiación. Con el objetivo de desarrollar una herramienta de cálculo para asistir en el diseño y escalado de hornos industriales, se evalúan diferentes estrategias de cálculo concernientes a la economía computacional y su precisión de cálculo de diferentes parámetros importantes. Las estimaciones de las temperaturas en los hornos se comparan con las mediciones experimentales realizadas en prototipos reales en ciclos de operación típicos.

To Sofia, a very special daughter

Today I can tell you certainly that with perseverance all your dreams can become true

Para Sofía, una hija muy especial

Hoy puedo decirte con certeza que con perseverancia todos tus sueños pueden hacerse realidad

Acknowledgments

First and foremost, I want to express my gratitude, regard and deep sense of admiration to my thesis supervisor, Dr. Cristóbal Cortés, for giving me the opportunity to work with him, showing his faith in my abilities and correcting me in the right moments. I appreciate all the scientific discussions I had with him, his guidance, help and advices during my PhD studies, which allowed to focus my efforts on the right path. Above all, I acknowledge his efforts to give me the best possible conditions and support me, in his own way, in all my personal situations. It is my pleasure to thank him for all this time, working with Dr. Cortés has been a wonderful experience and a truly honor.

I would like to acknowledge to the Dr. José Huertas and Dr. Juan Tibaquirá at the early stages of my research career. From whom I received a rigorous training before my PhD studies that opened my mind to a scientific world.

I thank all the colleagues of the group of thermal systems of CIRCE for sharing their time and knowledge with me. I did not have the opportunity to work with all of them, but I greatly benefited from their expertise and experience. I wish to express my sincere gratitude for make me feel welcome from the arrival day so far. My mates have always given me a healthy academic environment and more than a warm working atmosphere. For me, it is important to express my gratitude to my colleagues of the UTA, for the stimulating discussions and constructive criticism of our work. Specifically, I would like to thank to my friends and co-workers Juan Antonio Ramirez and Carlos Herce for their support and useful debates, both in academics and personal aspects, enlightening me on the challenges that I found no matter how difficult the problems were. Thanks to Alberto Carrion, because he was always there when I needed. I will always be indebted to them.

Throughout my stay in Zaragoza, I met several friends who made my life there an unforgettable experience. It is impossible to list all these people, but I thank the companionship and the shared moments with each one. I can point out that those days sharing a meal with people from more than ten nationalities and different point of views is something invaluable for me. I cherish all the moments spent with them and shall always be a part of my memories. My special gratitude to Mauricio Antelis, Victor Acosta and Cesar Cadena for the moments shared along the years.

Thank to my God for the wonderful life that he give me, for the opportunity to fight for my targets and for giving me the means to reach them, for this amazing travel and for all the people that I found in the road. Thanks for give me your hand, even when I have believed that I don't need it. You are the strongest support in my life. Thank you, because this thesis is the end of the most important travel in my life, through this, I have been able to grow on different levels. Thus, I want to express my most humble gratitude to you.

Above everything, my PhD thesis would not have been possible without the support, encouragement and love of my family members. I am grateful with my wife Andrea, for joining me on this journey and trust blindly in me. For giving me space to accomplish this task and caring lovingly to our daughter over the years. Your love, understanding and support means more to me than you will ever know. Definitely, I couldn't have done it without you. The greatest thanks are for my daughter Sofía, for the compression that only you know how to give me. For giving me the balance that I need, I always find rest on your smile and new adventures in the worlds that your mind creates, your existence gives me the strength to keep going. I want to thank you especially for encouraging me in all of my pursuits and inspiring me to follow my dreams. I am especially grateful to my parents, who supported me in all senses. I know that they believe in me and want the best for me; I also know that with this achievement they are happier than me. Thanks for teaching me to pursue happiness, to believe in myself and give me all in the life even the life itself. I will never be able to repay their unconditional support and the personal sacrifices that they have made, those that made it possible for me to finish this large path of education. I am here because of you, for helping me through my study years.

Thanks Dad, for show me how the hard work is. Thanks Mom, for teaching me to be "quenched and tempered" in difficult times. My special thanks are due to my brother Uriel and my sister Johana for the support and unconditional love; you have done this separation more bearable. So much to catch up…, I want them back in my arms again. I would like to thank to Castaño, Castrillón and Ovalle for their unwavering friendship, I know you are waiting for me. I feel lucky and it is an honor that you call me "friend". Now I think in my best friend Gallón (R.I.P.), I know he'd be proud of me (always on my mind my brother), thank you for share a part of your life with me. Your son Diego has the same happiness that you shared with all us. Finally, thanks to all my family and friends.

I would like to express my heartfelt gratitude to all these people, because this is not just a personal sacrifice, but also involved all the people around me; they always endorsed my initiatives and are my robust support, but I acknowledge that I embarked in this journey without consulting them.

This PhD Thesis is based on investigation activities partially funded by the EU 7th Framework Program, project NMP 2009 LARGE3 - No. 246335, *New designs of ecological furnaces* – EDEFU (http://www.edefu.eu). Experimental facilities and tests were provided and accomplished by Corporación Tecnalia and Giesserei Instandsetzung Service (GIS 2003), that kindly provided experimental data. Help of the personnel of Tecnalia in Irún-San Sebastián and GIS 2003 in Vilanova i la Geltrú-Barcelona is kindly acknowledged.

Also, I want to acknowledge to the Santander Bank, it would have been impossible started my PhD studies without their financial support in the frame of the grants to Latin American students.

Mauricio Yilmer Carmona García

Contents

List of Figures

List of Tables

List of symbols and abbreviations

Nomenclature

A	pure substance A
A^*	mushy variable/modify the source term in momentum equation
A_k	area of surface k
B	pure substance B
c	specific heat
C^*	mushy zone constant
C_i	Concentration of pure substance B in an alloy
E	Eutectic point
E_K	emissive power of surface k
F_{kj}	view factor
g	≈ 9.81 m/s^2 acceleration due to gravity
h	enthalpy
h_{av}/h_{eff}	heat transfer coefficients
h_{conv}	heat transfer coefficients by convection
h_{rad}	heat transfer coefficients by radiation
h_{SL}	latent heat of fusion
J_K	radiosity of surface k
k	thermal conductivity
L	Liquid
LF	Liquid Fraction
P	Pressure
P_i	Point i
S	Solid
SF	Solid Fraction

SS	Solid Solution
S_h	Source term in energy equation
S_u	Source term in momentum equation
T	Temperature
t	time
t_c	thickness
T_E	eutectic temperature
T_L	Liquidus temperature
T_{melt}	melting temperature
T_M	Mushy temperature
T_S	Solidus temperature
u	fluid velocity
V	Volume
x	Variable assimilated to the space *x*
y	Variable assimilated to the space *y*
z	Variable assimilated to the space *z*
w	any thermal property of the mixture

Nondimensional numbers

Nu	Nusselt number	$\left(Nu = \frac{ht_c}{k}\right)$
Pr	Prandtl number	$\left(Pr = \frac{c\mu}{k}\right)$
Ra	Rayleigh number	$\left(Ra = \frac{\beta \Delta T g L_c^3}{\upsilon^2} Pr\right)$

Greek symbols

α	solid α
α_k	absorptivity of surface *k*
β	solid β
Δt	time step
δ_{kj}	visibility between surfaces *k* and *j*
ε	emissivity

ε_k	emissivity of surface *k*
ε_T	small temperature value (≈ 0.05 ºC).
γ	Liquid Fraction
ρ_k	reflectivity of surface *k*
ρ	density
σ	Stefan-Boltzmann's constant (5.672 x 10^{-8} ($W/m^2.K^4$))
τ	stress tensor

Subscripts

av	average
conv	convection
E	Eutectic point
eff	effective
eq	equivalent
i	subscript index, *i = 1, 2, 3*
j	subscript index, *j = 1, 2, 3*
k	subscript index, *k = 1, 2, 3*
L	Liquidus
LP	Liquidus Phase
M	Mushy
rad	radiation
res	resistance
S	Solidus
SP	Solidus Phase

Acronyms

2D	Two-Dimensional
3D	Three-Dimensional
BEM	Boundary Element Method
CFD	Computational Fluid Dynamics
CO_2e	Equivalent Carbon Dioxide

DC	Direct Current
DNS	Direct Numerical Simulation
EAF	Electric Arc Furnaces
EDEFU	EDEFU project: New Designs of Ecological Furnaces
ESR	Electro-Slag Remelting
EU	European Union
FEM	Finite Element Method
FVM	Finite Volume Method
IAI	International Aluminium Institute
IR	Infrared
LES	Large Eddy Simulation
LTE	Local Thermodynamic Equilibrium
OES	Optical Emission Spectroscopy
PCM	Phase Change Materials
RANS	Reynolds Averaged Navier-Stokes
S2S	Surface-to-Surface radiation model
UBC	Used Beverage Cans
UDF	User Defined Function
URANS	Unsteady Reynolds Averaged Navier-Stokes
U.S./USA	United States of America
VOF	Volume of Fluid

1. Scope, aims and outline

This thesis describes the numerical study of the thermal behavior of two different prototypes of furnaces used in secondary aluminum production. The first prototype is a melting furnace heated by a plasma torch, and the second prototype is a holding furnace heated by electrical resistances. The numerical analysis is accomplished with the computational fluid dynamic (CFD) approach by means of a commercial code. The models presented can be used to estimate the melting rate, molten fraction of the load, energy requirements, heat losses and temperature distribution in the load and refractory parts.

The aim of the simulations is to develop a calculating tool to assist in the design, scaling-up and control of industrial furnaces used in aluminum secondary production with good compromise of the computational resources and accuracy. It is also proposed that the use of CFD can provide accurate information about thermal variables, many of them very difficult to determine experimentally, such as load and refractory temperatures and their time evolution, patterns of movement inside the molten load and distribution of heat losses. These results can be used in order to understand the physics involved in the process.

Chapter 2 is an introduction of the aluminum features, production and utilization. After that, the role of the secondary aluminum production in the global market is presented. Also, the stages of aluminum secondary production are presented, including details of the melting and holding furnaces used, and their present-day technologies. Finally, a motivation of the current thesis is presented.

Since the core of such a simulation must include a model for the phase change of the load material, an overview of the numerical methods used in phase change problems and the state of the art of the related simulations are presented in Chapter 3. The governing equations and the radiation heat transfer model used for the numerical simulations in the present thesis are also presented in this chapter.

In chapter 4, simulations of a new aluminum melting furnace heated by a plasma torch are presented; these simulations reproduce an experimental test carried out in a real prototype. Models used are 2D axisymmetric and take into account heat conduction in solid parts, convection in air and molten aluminum, interactions between gas-liquid-solid zones and radiation heat transfer. Several calculation strategies are tested concerning their computational economy and their accuracy in computing different key parameters. Results show that interactions gas-liquid-solid have an important effect. Firstly, a proper account of heat transfer and losses requires solving the conjugated problem comprising refractory walls and heated load. Secondly, thermal interaction with air cavities seems to determine the convective movement of the molten load and therefore inner-load temperature patterns and their time evolution.

An experimental prototype of holding furnace heated by an electrical resistances system is numerically simulated in Chapter 5. Models used take into account the same complexities presented in the simulations of the melting furnace, but in this case the models are 3D. As a first approach, the symmetry of the geometry is used to reduce the computational resources and only a quarter of domain is initially simulated. Nevertheless the predicted velocities for the flow in the molten load suggest that the patterns induced by the convection effects have a three dimensional behavior. For this reason a new simulation with the full domain is carried out. Both simulations predict almost the same temperatures and energy distributions with different patterns of flow in the molten load.

Finally, a summary, general discussion on the major results and conclusions are presented in Chapter 6. New contributions and recommendations for continuing research are also included.

2. Introduction

2.1 Aluminum characteristics

Aluminum has become increasingly important in the production of automobiles and trucks, packing of food and beverages, buildings and construction, transmission of electricity, development of transportation infrastructures, production of defense and aerospace equipment, manufacture of machinery and tools, and production of durable consumer products. This tendency is due to the special properties of aluminum such as its light weight, high corrosion resistance, good formability and non-toxicity (Totten and MacKenzie, 2003a). The main physical properties of aluminum appear in Table 2.1, and their main mechanical properties are shown in Table 2.2.

Table 2.1. Main physical characteristics of aluminum (Totten and MacKenzie, 2003b)

Properties	
Crystalline structure	fcc
Atomic weight	26.98154
Specific mass at 20ºC (g/cm^3)	2.69890
Solidification shrinkage (%)	6.5
Fusion temperature (ºC)	660.4
Ebullition temperature (ºC)	2494
Linear thermal dilation coefficient, from 20ºC up to 400ºC (ºC x 10^6)	26.4
Specific heat at 25ºC (J/kgºC)	900.0
Latent heat of fusion (kJ/kg)	397.0
Combustion heat (MJ/kg)	31.07
Volumetric electric conductivity (% IACS)	64.94
Thermal conductivity at 25 ºC (W/m ºC)	247

Table 2.2. Main mechanical properties of pure aluminum (Totten and MacKenzie, 2003b)

Property	**Annealed**	**Hard-drawn (90%)**
Tensile strength (MPa)	40-50	120-140
Yield point (MPa)	15-20	100-120
Brinell hardness (kgf/mm^2)	12-16	27
Stretch	50-70	8-12

Despite that the tensile strength and the yield point of pure aluminum are fairly low, which reduces the applicability of this metal in structural uses, aluminum alloys can achieve tensile strengths over 600MPa after heat treatment. The specific weight of the aluminum is about one-third of the specific weight of iron or copper. Due to these general good properties, the aluminum is the second most used metal in the world.

2.2 Aluminum production

Aluminum is the most abundant metal in the earth crust. Nevertheless, in nature, aluminum does not exist as a metal because of the high chemical affinity for oxygen. Chemical processing has always been necessary to extract pure alumina (aluminum oxide, Al_2O_3) from the other ingredients associated with it in the deposit. The primary natural ore for aluminum is bauxite, a mineral consisting primarily of hydrated aluminum oxides. Aluminum is recovered from bauxite by a selective leaching sequence known as the Bayer process, which dissolves most of the aluminum while leaving impurities behind. The aluminum is recovered from the leach solution by precipitating it as aluminum hydroxide. The hydroxide is then dried and calcined to generate purified alumina. The calcined alumina is fed to electrolytic cells containing a molten salt electrolyte based on cryolite (Na_3AlF_6). The alumina dissolves in the cryolite and is electrolyzed to generate molten aluminum metal and carbon dioxide gas. This process called the Hall-Heroult process has been the sole approach for producing primary aluminum metal since the late 1800s and will likely continue in this role for decades to come (Schlesinger, 2006, Totten and MacKenzie, 2003a). Figure 2.1 shows a diagram of the Bayer and Hall-Heroult processes.

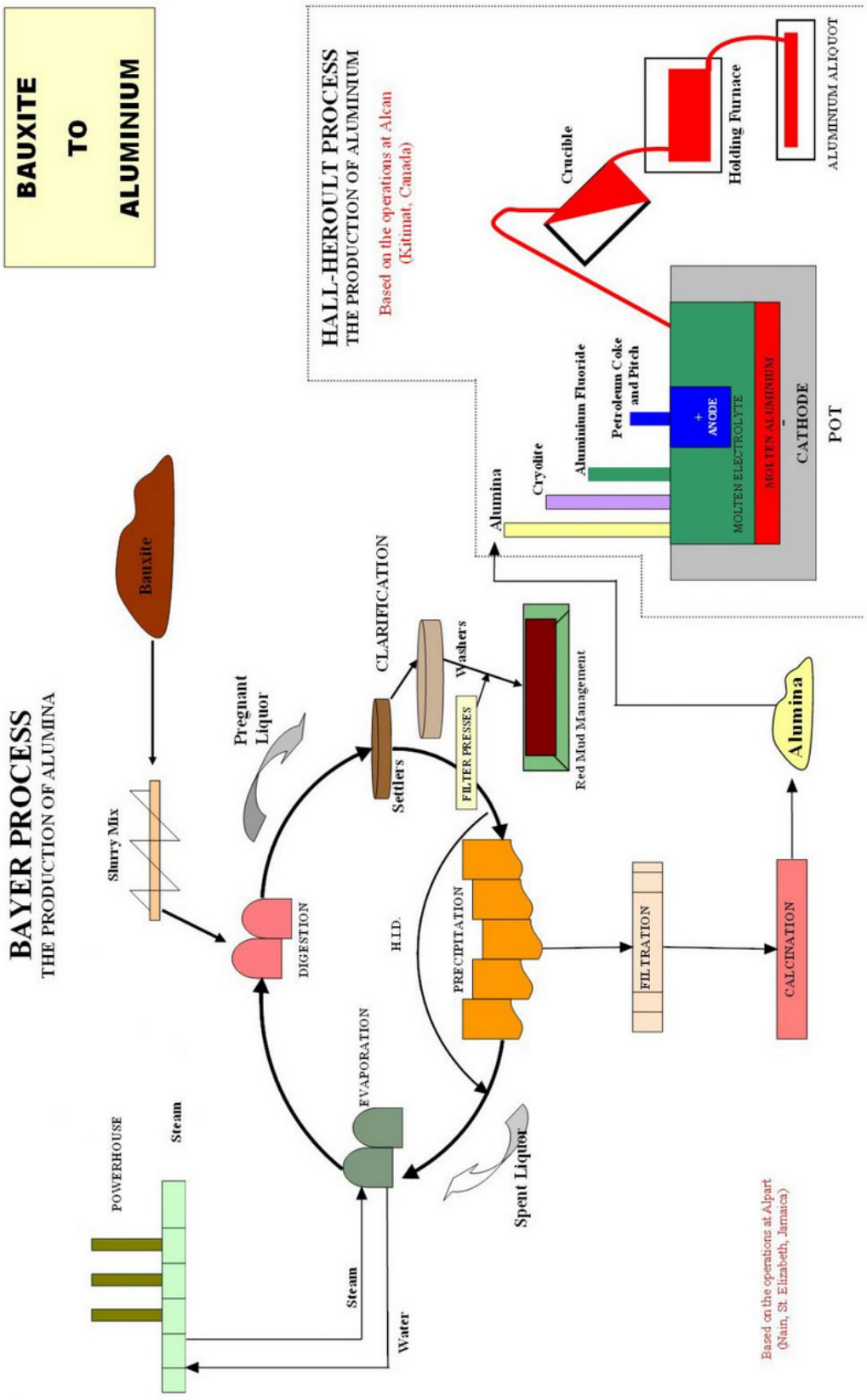

Figure 2.1. Scheme of the Bayer and Hall-Heroult processes (JBI, 2013)

Production of aluminum metal has previously focused on its recovery from naturally occurring raw materials. However, in recent decades an increasingly large fraction of the world's aluminum supply has come from a different source. This is the aluminum scrap recovered from industrial waste and discarded postconsumer items. The treatment of this scrap to produce new aluminum metal and alloys is known as recycling, and metal produced this way is frequently named ***secondary*** (Schlesinger, 2006).

2.3 Aluminum utilization

Around 54 million tonnes of aluminum, from primary and recycled sources, ended up in finished products in 2011. Three quarters of all the aluminum ever produced (since the 1880s) is still in productive use, in fact 90% of aluminum goes into products with long life times. About 32% is located in buildings in the form of facades, windows, doors etc., 28% as electrical cable and machinery and 28% within moving objects such as cars, commercial vehicles, trains and ships. In 2011 this stock had grown to about 727 million tonnes (approximately 1 billion tonnes today). The global stock of aluminum in productive use is growing every year, in 2011 by 40 million tones. More than a third of all the aluminum currently produced originates from recycled and two-thirds from primary metal; making the secondary production a key element of the aluminum market. Aluminum recycling is divided in two categories: (a) new scrap arises during the manufacturing of aluminum semi-fabricated and final products; (b) old scrap refers to those products collected after disposal by consumers. Old scrap is often more contaminated than new scrap. End-of-life vehicles, demolished buildings and constructions, discarded packaging material, home and office appliances, as well as machinery equipment are all potential sources of old aluminum scrap (Tsesmelis, 2012). A special mention receives the old scrap with low thickness and reduced contamination, which is called light-gauge scraps; typical examples are the used beverage cans (UBCs), aluminum chips or aluminum foils. Figure 2.2 shows the aluminum mass flow model presented by the international aluminium institute (IAI) for the year 2011.

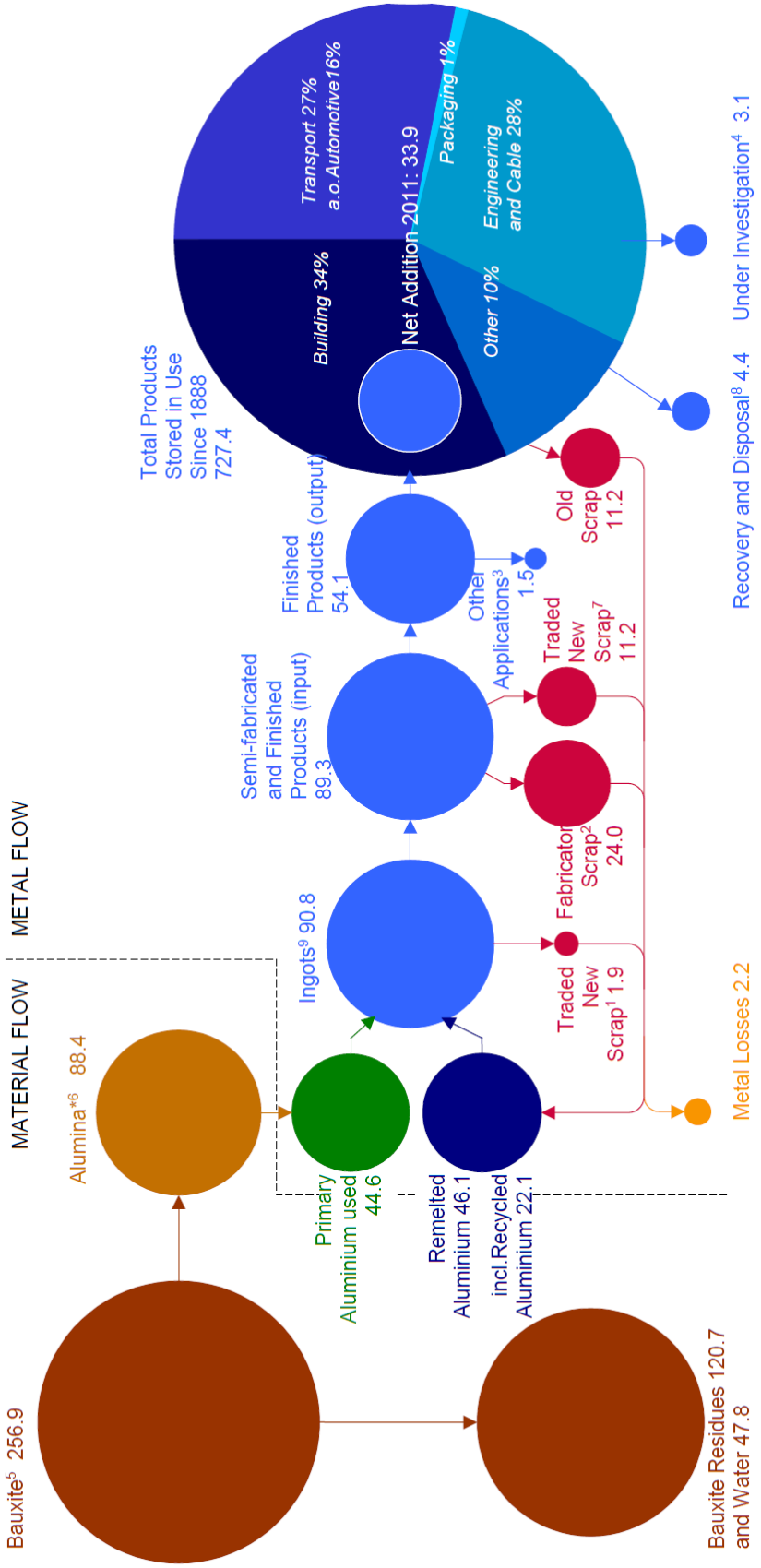

Values in millions of metric tonnes. Values might not add up due to rounding. *Change in stocks not shown.
1 Aluminium in skimmings; 2 Scrap generated by foundries, rolling mills and extruders. Most is internal scrap and not taken into account in statistics;
3 Such as deoxidation aluminium (metalproperty is lost); 4 Area of current research to identify final aluminium destination (reuse, recycling, recovery or disposal);
5 Calculated based on IAI LCI report - update 2010. Includes,depending on the ore, between 30% and 50% alumina; 6 Calculated. Includes on a global average 52% aluminium;
7 Scrap generated during the production of finished products from semis; 8 Either incinerated with/without energy recovery, material recovery or disposal;
9 Estimated stock decrease 440,000 tonnes

Figure 2.2. Global aluminum mass flow for the year 2011 (Tsesmelis, 2012)

Figure 2.3 shows a diagram of the aluminum production and life cycle to illustrate the capacity of aluminum to reach the statistical data presented.

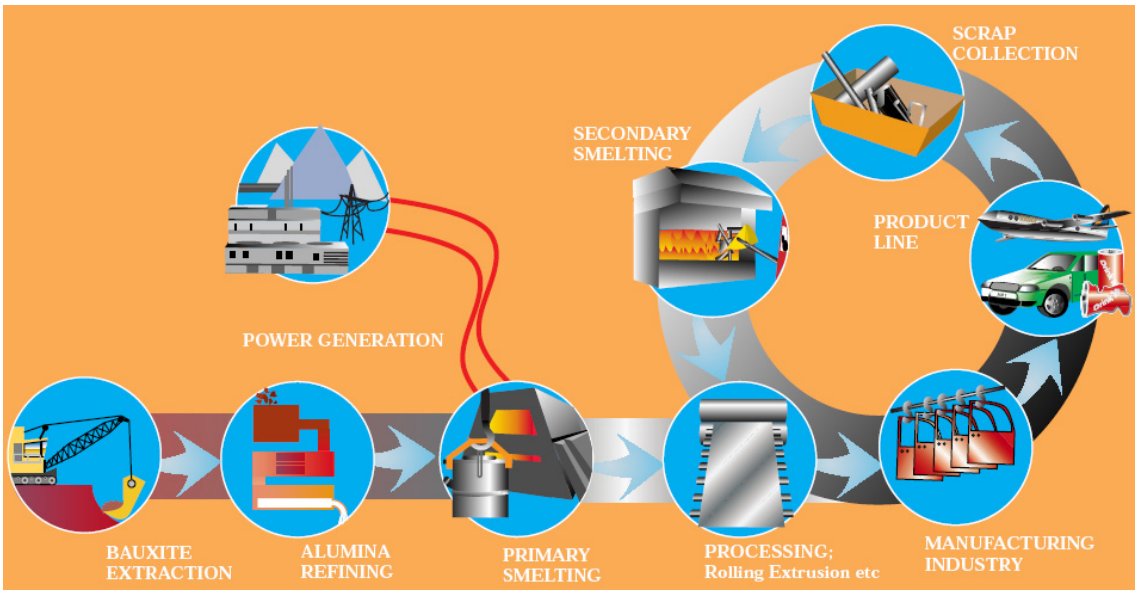

Figure 2.3. Diagram of aluminum production and life cycle (Word-aluminium, 2013)

The market for aluminum products is generally separated into seven segments: building and construction, transportation, consumer durables, electrical, machinery and equipment, packaging, and other. Figure 2.4 shows the aluminum consumption and the total aluminum in use by sectors for the year 2010.

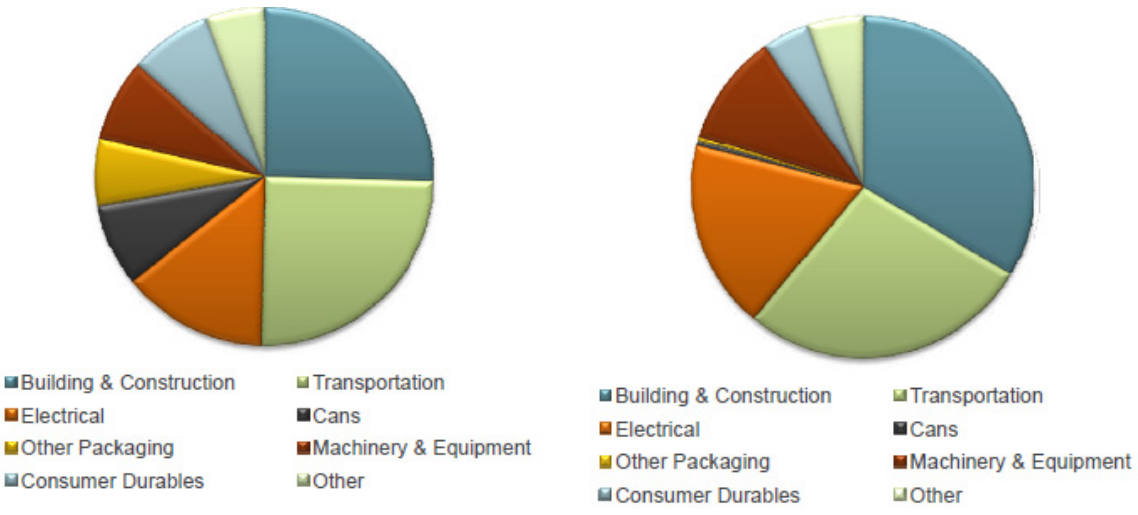

Figure 2.4. Aluminum consumption (left) and total aluminum in use (right) by sectors – 2010 (Bayliss, 2012)

2.4 Secondary aluminum perspectives

2.4.1 Advantages

The secondary metallurgy of aluminum allows an economy of raw materials and energy. The recycled aluminum production has a gain of 95% in energy compared with primary aluminum (Bayliss, 2012, Green, 2007, Schlesinger, 2006, Totten and MacKenzie, 2003b, Tsesmelis, 2012). Aluminum scrap has considerable market value because most of the energy required for the production of primary aluminum is embodied in obtain the metal itself, and consequently in the scrap. Therefore, the energy needed to melt aluminum scrap is only a fraction of that required for primary aluminum production.

Another positive aspect of aluminum recycling is the environmental impact. Compared with the production of primary aluminum, recycling of aluminum products emits only 5% of the greenhouse gas so that recycling used aluminum products currently saves 100 million tonnes of CO_2e (equivalent carbon dioxide) per year. On the other hand, primary aluminum production generates solid waste at every step in the process. The most significant of these is the red mud residue created during alumina purification; the production of one metric ton of primary aluminum requires about four metric tons of bauxite and it produces around two metric tons of red mud. With the generation of red mud, the production of primary aluminum also releases fluorides. The mining of bauxite is also an activity that causes problems to the environment, because this activity devastates forests and needs space to dispose of the wastes. While aluminum recycling generates solid wastes as well (primarily the dross and salt slag created during remelting), the volumes are much smaller (Schlesinger, 2006, Totten and MacKenzie, 2003b).

Furthermore, primary aluminum production requires a mining operation, a Bayer-process plant to produce purified alumina, and an electrolytic pot line to extract aluminum metal from the alumina. The equipment used for recycling is less complex and thus less expensive; also the process can be adjusted to the demand, sources of combustibles or electricity supply.

Finally, the aluminum has a great recycling potential. On the one hand, from a technical point of view, if scrap is pre-treated and/or sorted appropriately, the recycled aluminum can be utilized for almost all aluminum applications. Aluminum can be recycled over and over again without any loss of its inherent properties. Almost all the aluminum alloys can be recycled, either separately or in combination with others alloys (Schlesinger, 2006). These characteristics have enabled the high percentage of metal still in use of the total production, some having been through countless loops of its lifecycle. On the other hand, for most countries, there is a well-established market for recycled aluminum with firmly defined distribution chains.

For all these advantages, the recycled rate of aluminum has been increased. Today secondary metallurgy is a major aspect of continued aluminum use and it is a growing industry.

2.4.2 Production

The high intrinsic value of aluminum scrap has always been the main impetus for recycling, independent of any legislative or political initiatives. For some products, in addition to this obvious economic dimension, growing environmental concerns and heightened social responsibility, over the last decade in particular, have served to boost recycling activity in order to conserve resources and to avoid littering. In 1990 the total aluminum production was around 28 million tonnes and today the total is close to 69 million tonnes (with around 20 million tonnes recycled from scrap). By 2020 metal demand is projected to have increased to around 110 million tonnes (with around 35 million tonnes recycled from scrap). Figure 2.5 shows the global share of primary and recycled aluminum production from 1950 to the current day and the estimated production until 2020 (Word-aluminium, 2013).

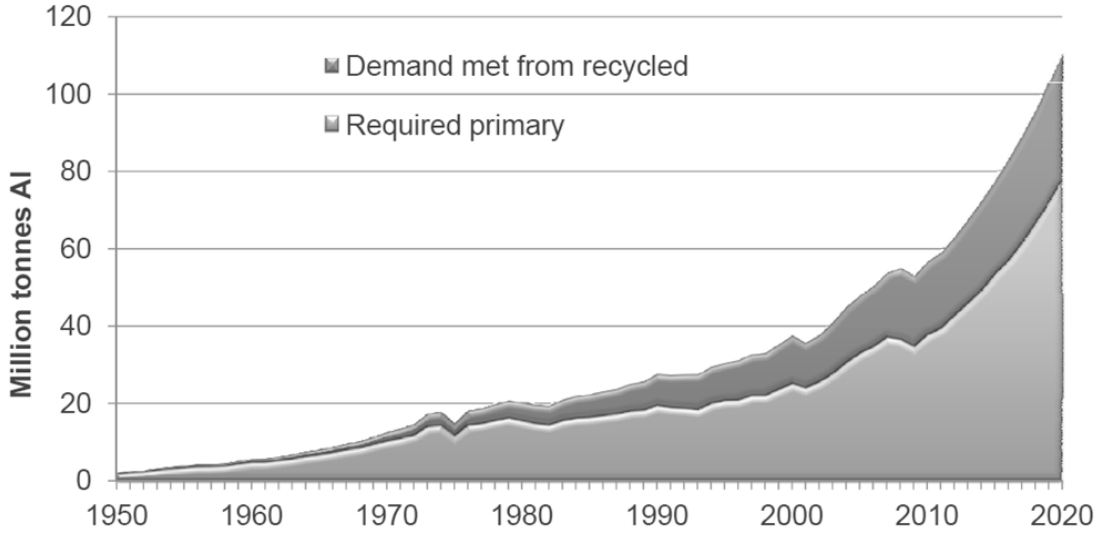

Figure 2.5. Global share of primary and recycled aluminum production-current day and estimated production until 2020 (Word-aluminium, 2013)

The aluminum industry recycles all the aluminum scrap it can obtain. Primary aluminum producers and the producers of semi-fabricated and fabricated products generally collect and recycle all of the aluminum scrap they generate (new scrap) and therefore the success of a recycling system depends on the degree to which used products are collected at the end of their lives. Collection rates vary depending on the product in question, waste management systems in place and on society's understanding of the value of aluminum scrap and its compromise to conserve that value. Table 2.3 lists the average percent of the input aluminum turned into scrap by manufacturing operations in different industrial sectors (new scrap). Figure 2.6 shows a scheme of the product life and recycling rate for aluminum products in various sectors, which is associated to the availability of old scrap.

Table 2.3. Generated new scrap by market sector (Schlesinger, 2006)

Market	**Scrap/input material (%)**
Building and construction	20
Transportation: aerospace	60
Transportation: auto and light truck	25
Transportation: trucks, buses and trailers	25
Transportation: rail	25
Transportation: other	25
Consumer durables	20
Electrical	10
Machinery and equipment	15
Containers and packaging: foil	10
Containers and packaging: other	25
Other	25

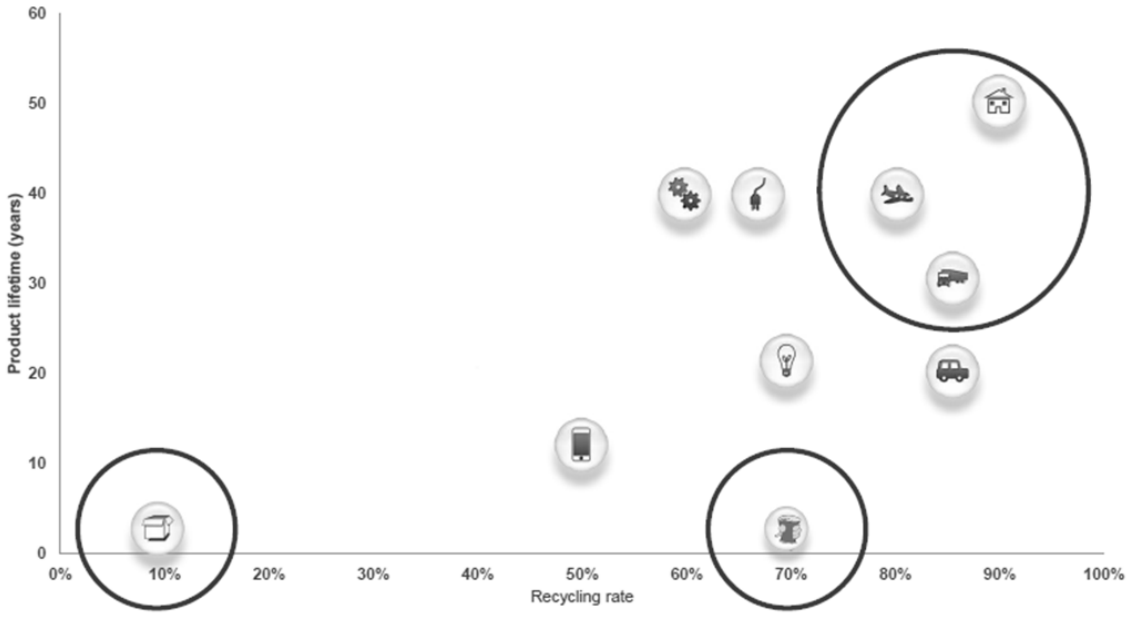

Figure 2.6. Product lifetimes vs. recycling rates (Tsesmelis, 2012)

Globally, aluminum achieves among the highest material recycling rates for end of life products, with up to 90% for transport and construction applications. Only a few package products presents low recycling rate. The metal's economic scrap value and

ability to be recycled continuously makes the aluminum beverage can the most recycled container in the world, with a global average recycling rate of 70% and a rate of over 90% in some countries.

The amount of aluminum produced from old scrap has grown from one million tonnes in 1980 to 10 million tonnes in 2009. Since the 1980s the transportation sector has been the most important resource for recycled aluminum from end-of-life products. As aluminum construction products often have lifetimes running into decades, scrap from building applications has only become available in the 2000s and only in the quantities put into such applications when the buildings were constructed, over 30 years ago. Today recycled aluminum produced from old scrap originates 42% from transport, 28% from packaging, 11% from engineering and cables and only 8% from building applications, due to their long life times (Word-aluminium, 2013).

The collection and sorting of aluminum scrap, especially old scrap, is often a complex scheme involving millions of households, local and regional authorities, small and medium collectors and metal merchants. Waste and environmental policies can also have strong influences on the effectiveness of collection schemes. Today, around 50% of the scrap is old scrap (Word-aluminium, 2013). The supply of old scrap is affected by the amount of short-life products; so, UBCs are, in most cases, the main source of old scrap (approximately 50% of old scrap). Figure 2.7 shows the evolution of the recycling rate of aluminum cans from 1995 to 2010 in different countries. Global aluminum industry will work to encourage a global aluminum UBC recycling target of 75% by 2015. The performance of this plan is good: 72% in 2010, up from 57% in 2003 (Bayliss, 2012). Figure 2.8 shows the evolution of the averaged, recycling rate of aluminum cans in the world from 1995 to 2010, while the aluminum beverage can collection rate of different countries in 2008 appears in Figure 2.9.

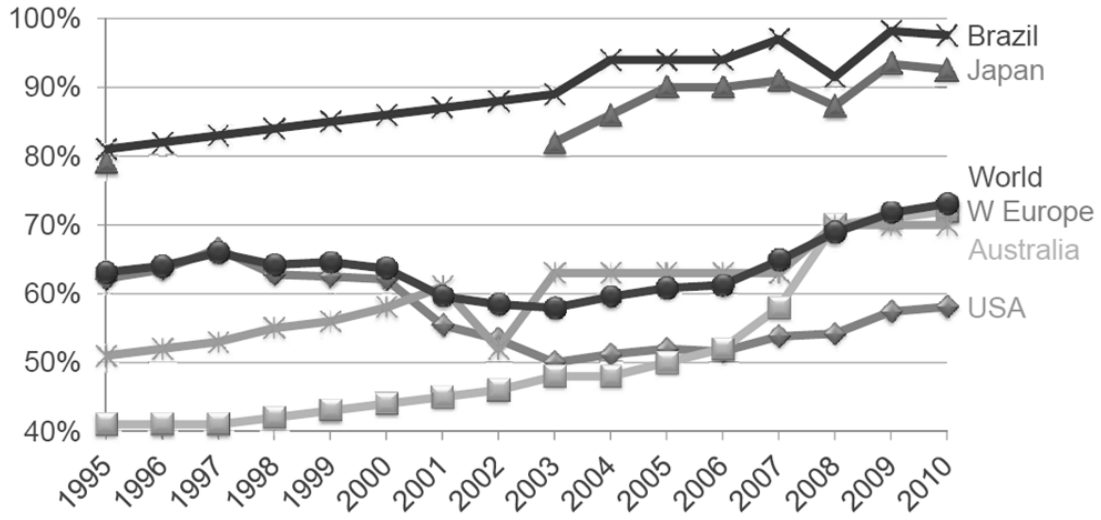

Figure 2.7. Regional UBC recycling rates, 1995-2010 (Bayliss, 2012)

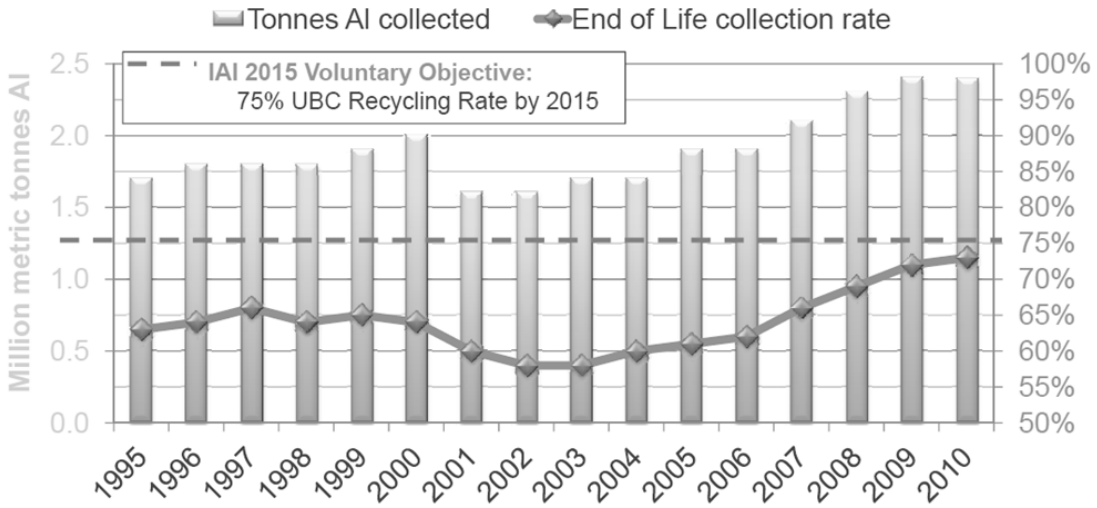

Figure 2.8. Global UBC recycling rate and collection volume, 1995-2010 (Bayliss, 2012)

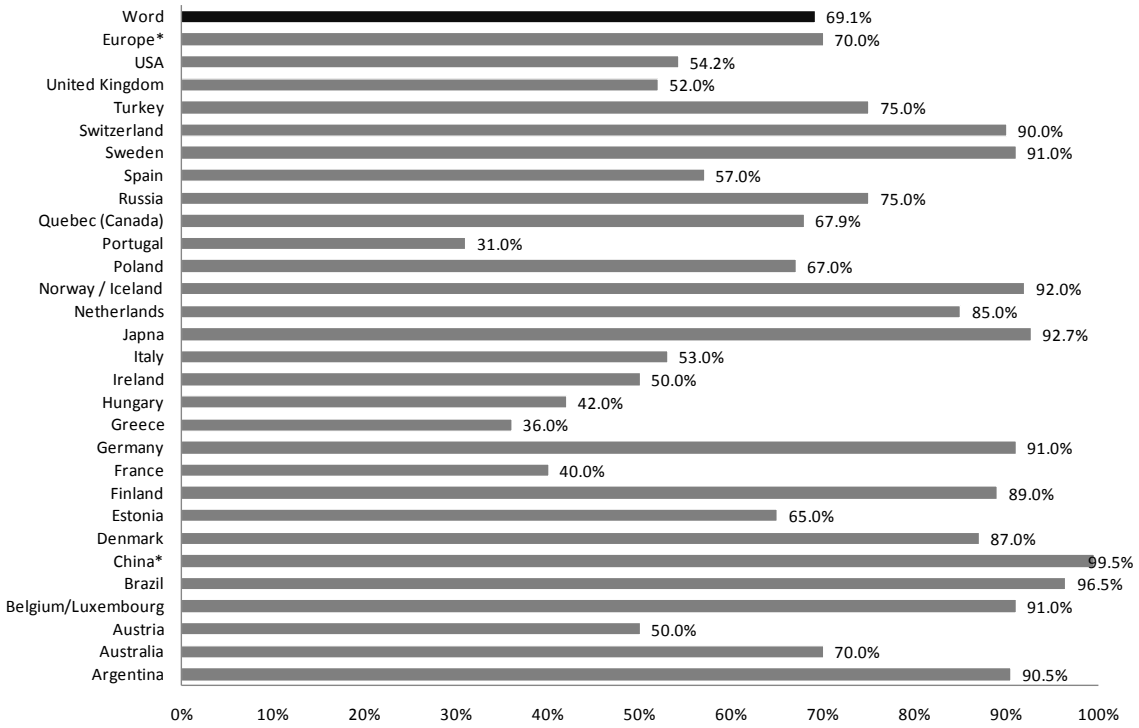

**Includes unregistered collection*

Figure 2.9. UCB collection rate different countries: 2008 – Adapted from Word-aluminium (2013)

2.4.3 Final products

The recycled product may be the same as the original product, but is more often a completely different product. The greatest part of the UBCs is collected to produce new beverage cans. Most of the remaining old scrap is used to produce cast alloys for automotive or aerospace industry (Totten and MacKenzie, 2003b). Depending on the origins of the scrap, remelted wrought alloys remain largely in the same production process as input material for either rolled products or extruded products. Casting alloys are the products of the refining process using mixed new and/or old scrap. Some refiners also produce a small amount of aluminium alloys as de-oxidation agent for the steel making industry. As input material to the foundries, casting alloys are processed through pressure die-casting, gravity die-casting and sand casting into various cast products. One of the major sectors using aluminum castings is the automotive industry and applications include fuel engine blocks, cylinder heads, transmission cases, energy absorbers, safety parts, suspension parts, components of steering system and wheels.

Aluminum castings are also widely used in building and construction as components of equipment and on-site facilities, and in the engineering sectors as components of both heavy and fine machines and tools (Word-aluminium, 2013).

2.4.4 Recycling plants in the world

There are no quality differences between a product entirely made of primary metal and a product made of recycled metal. However, due to the overall limited availability of aluminum scrap, recycled aluminum is used where it is deemed most efficient in economic and ecological terms.

According to Schlesinger (2006), the successful recycling of aluminum depends on several factors:

- A plentiful and recurring supply of the metal, concentrated sufficiently in one area to justify the cost of collecting it
- An infrastructure for collecting the scrap metal, removing impurities, and delivering it to a recycling facility
- A method for recycling the metal that is economically competitive with production of the metal from primary ores
- A market for the recycled metal, should its composition or quality differ from that of primary metal

Despite these limitations, many recycling plants are disposed across the world. Figure 2.10 shows the number of recycled plants for the year 2008.

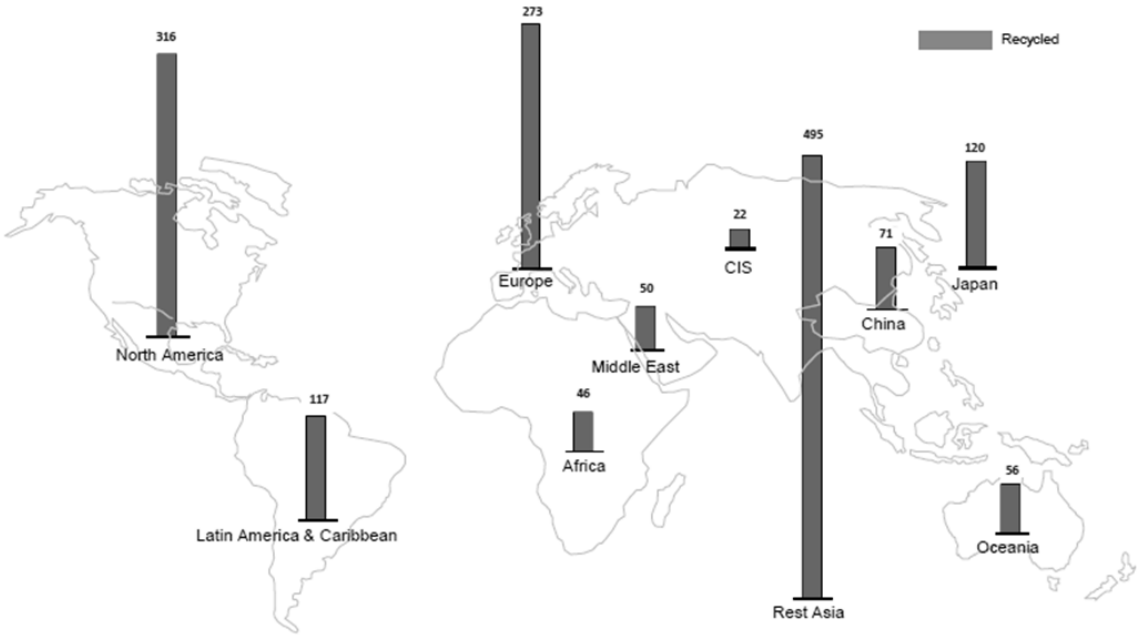

Figure 2.10. Number of recycling plants – 2008 (Word-aluminium, 2013)

United States of America and Japan are the most traditional recycling centers. Increasing recycling activities are evident in China, India and Russia. Latin America, the Middle East, Oceania and Africa focus on primary aluminum production while recycling plays a minor role, mainly due to lower domestic scrap availability. In addition, much of the aluminum scrap in some of these countries (for example, Australia and Canada) is exported to other regions where a major recycling sector exists (Word-aluminium, 2013).

2.4.5 Prospect

The increasing demand for aluminum and the long lifetime of many products, limiting their availability for short term recovery but maximizing their in-use benefits, mean that the overall mass of primary metal consumed will continue to be around double that of recycled metal, for the foreseeable future. However, improving the overall collection rates of used products is an essential element in the pursuit of sustainable development. Industry continues the recycle of all the aluminum collected from end-of-life products as well as from fabrication and manufacturing process scrap. With a growing number of industry initiatives and the help of appropriate authorities, local communities and society as a whole, the amount of aluminum collected could be increased further. Furthermore, the amount of end-of-life aluminum products will be increased in coming

years, as a result of the use of aluminum over 30 years ago in industries with high life time. By these reasons, the secondary production of aluminum presents great perspectives in the global market.

2.5 Stages of secondary aluminum process

Depending on its source, aluminum scrap may contain a range of impurities. The composition of new scrap is well known and in principle new scrap does not need any pretreatment process before it is remelted, although cutting to size might be necessary. Old scrap is collected after a consumer cycle, either separately or mixed, and it is often contaminated to a certain degree, depending highly on its origin and collection systems (Muchová and Eder, 2010). The level and type of contaminants in the scrap is essential to determine the pretreatment, the furnace and even the process to implement in the aluminum recovery. The European standard on aluminum scrap (EN 139209) covers all scrap types present in the practice.

Table 2.4 shows the main scrap categories with their average metal and oxide content plus the amount of foreign material (e.g., lacquers, paint, oil, coatings) in the scrap.

After collecting the aluminum scrap, it is separated from contaminants into various streams, using differences between the physical properties and those of the gangue. In some cases, chemical or thermal processes may be used to remove impurities from the material. Separation of aluminum at this stage can be done by various mechanical operations, such as magnetic, gravity, eddy current, or color sensor. Further separation of different aluminum alloys can also be achieved through x-ray methods. The final classified scrap may be agglomerated to make them easier to ship and easier to handle in subsequent smelting processes. In summary, the pretreatment of scrap can be divided into four types of unit process: comminution, separation, thermal processing, and agglomeration. Schlesinger (2006) presents details of each scrap pretreatment process.

Table 2.4. Main scrap types - European aluminum scrap standard (EN 13920) (Boin and Bertram, 2005)

Part	Scrap Description	Aluminum Metal[a] (%)	Oxides[b] (%)	Foreign Material[b] (%)
3	Wire and cable (new scrap)	98.7	1.3	—
	Wire and cable (old scrap)	97.7	1.8	0.5
4	One single wrought alloy	97.2	1	1.8
5	Two or more wrought alloys of the same series	97.2	0.8	2
6	Two or more wrought alloys	94	0.8	5.2
7	Castings	83.4	6.2	10.4
9	Shredded and density separated scrap	84.5	5.4	10.1
10	Used beverage cans	94	0.8	5.2
12	Turnings, one single alloy	95.3	3.7	1
13	Mixed turnings, two or more alloys	84	3.3	12.8
14	Packaging (coated)	71.5	3.8	24.7
15	Packaging (de-coated)	86.1	12.9	1
16	Dross	55.7	44.3	—

[a] Based on empirical data. [b] According to the definitions of the different EN 139208 scrap categories and industry knowledge about scrap composition

The load is charged into the melting furnaces. The melting of scraps is usually performed in rotary, reverberatory or crucibles furnaces. Molten salt fluxes are often used in the melting of scraps highly oxidized or light-gauge scraps. Even though the oxidation is low on light-gauge scraps, this phenomenon is only superficial; thus, the thickness of the raw materials to be melted influences the amount of oxide produced during the process, i.e., the thinner the raw material, the higher the oxide formation. This behavior occurs because the relation surface/volume becomes high when dealing with thin raw material. The oxidation process of aluminum alloys depends on the superficial condition of the sample, on the alloy composition and on the temperature. Typically, the proportion of the fluxes is not more than 2% by weight of the charge, but this fraction might be higher when the raw material is composed mainly of light-gauge scraps or contains organic coatings. The main function of the saline fluxes is to act as a barrier between the liquid aluminum and the oxygen of the atmosphere, diminishing the process of superficial oxidation of aluminum. Other function of the salts layer is to serve as a flux and remove impurities in the molten load (Totten and MacKenzie, 2003b).

Drosses are produced during the aluminum melting processes. Due to the high aluminum reactivity with oxygen, the formation of a superficial layer of oxide occurs. This layer becomes a physical barrier between the melt aluminum and the oxidant atmosphere, hence protecting the bath against oxidation. Turbulence generated by the handling of the liquid metal makes a new exposure of aluminum, which causes an increase in the oxide layer. At the end of the melting process, this oxide layer is removed. During the removal of the oxide layer, some amount of aluminum is dragged along with the oxide. The drosses are separated into three different classes (Totten and MacKenzie, 2003b):

- White Dross: It is formed from the primary metallurgy of aluminum. The main characteristics that distinguish this class of dross from the others are the absence of salt fluxes and the fact that this dross is usually whitish or grayish or presents a light color.
- Black Dross: It is produced in the secondary metallurgy of aluminum due to the use of salt fluxes. The produced dross presents dark colors.
- Saltcake. It is the result of the aluminum recovered from white and black drosses. It is characterized by the high concentration of salt and by its darkish color.

Schlesinger (2006) describes the choices available in dross treatment technology, and the factors determining whether one technology is favored over another. Totten and MacKenzie (2003b) describe the technology used to recover the aluminum content from each dross type.

After melting, the molten metal is transferred to holding furnaces for further refining processes such as de-gassing, reduction of magnesium content (a process known as “de-magging”) and for adding alloying elements. Also, its temperature is maintained or increased and its composition is adjusted for the casting process. Typically, the holding process is performed in reverberatory or crucible furnaces.

From the holding furnaces, molten metal is either tapped to the casting unit to produce ingot or slabs, or into crucibles for liquid aluminum delivery. Figure 2.11 shows the aluminum secondary stages after scrap collecting.

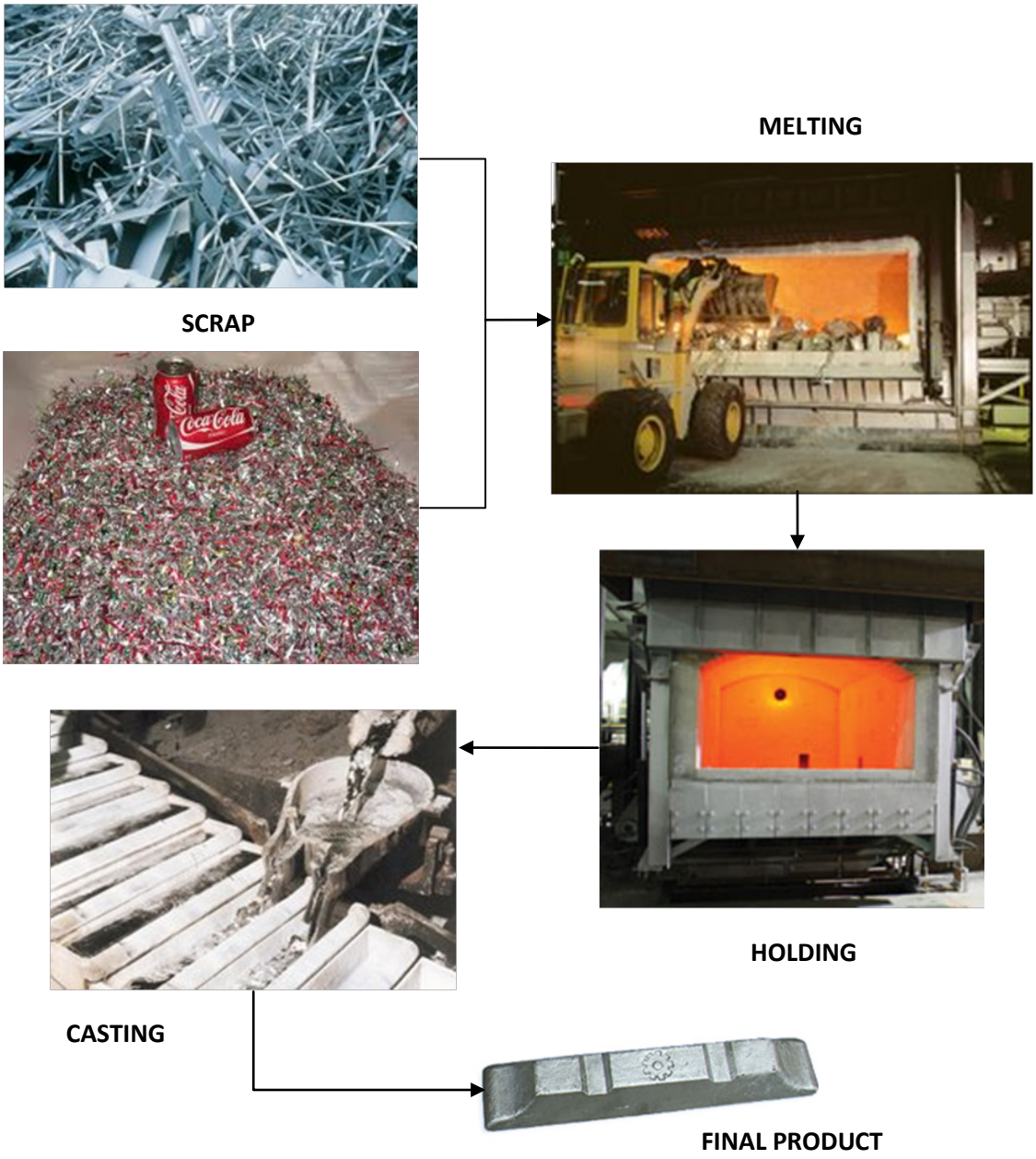

Figure 2.11. Aluminum secondary stages

2.6 Furnaces used in aluminum secondary production

The key equipments for the metallurgical processing of aluminum scrap are furnaces. Remnant contaminations and foreign matter can be removed as soon as the metal reaches the liquid stage. Also, it is possible to adjust the composition and obtain the

desired alloy during the process (Schmitz, 2006). In this section, some details about melting and holding furnaces used in secondary aluminum are presented. This summary is organized based in the layouts of the works of Schlesinger (2006) and Schmitz (2006) and, where the data is partially gathered and more detailed information can be found about the topics involved.

2.6.1 Melting furnaces

2.6.1.1 Sweat furnace

Some aluminum parts are so intricately attached to iron parts that they will not be separated by ordinary shredding. Examples include transmissions, cylinder heads, and manifolds. These items are known as high-irony scrap because of the extremely high levels of iron (50% or more at times). Scrap of this type has too much aluminum to be classified as ferrous scrap but too much iron to be remelted by secondary smelters. To separate these components, it is often used the sweat furnaces. Here, the high-irony scrap fed to the furnace is heated to a temperature just above the melting point of aluminum. At this temperature, the aluminum slowly melts away (hence the term sweating), leaving the higher-melting-point iron behind. The liquid aluminum drains from the bottom of the furnace and is cast in the form of sows or pigs. The product is often known as sweated pig and is sold to secondary smelters, where it is remelted and mixed with other scrap. Figure 2.12 shows large-scale rotary sweat furnace.

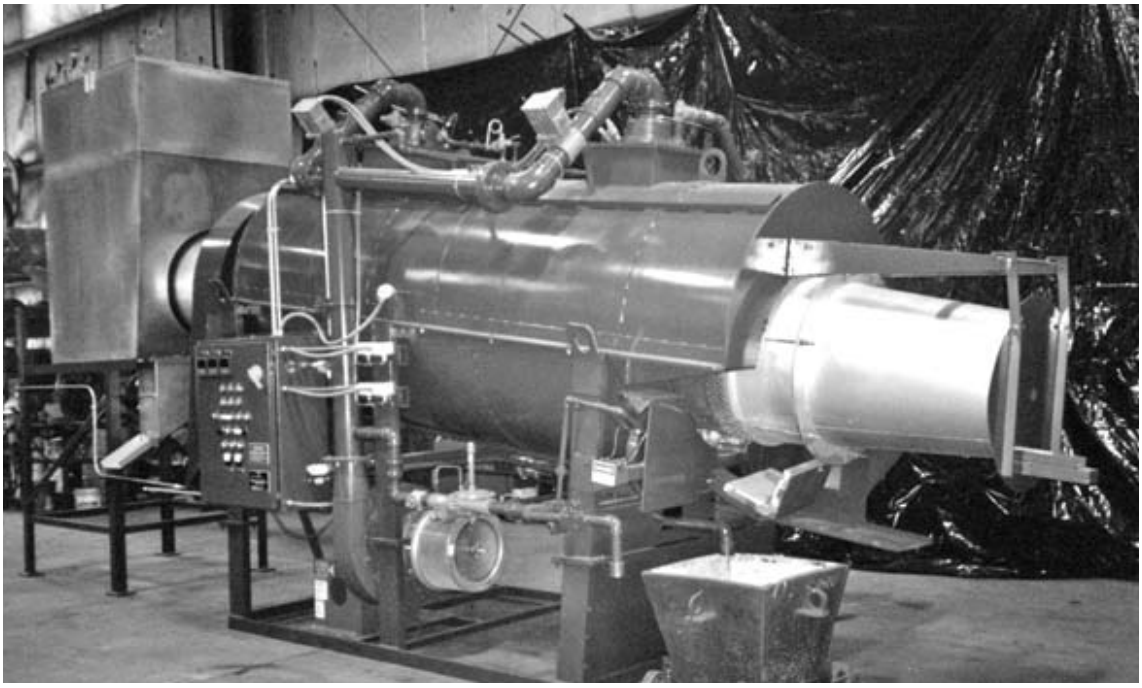

Figure 2.12. Large-scale rotary sweat furnace (Schlesinger, 2006)

2.6.1.2 Wet-hearth

The classic single chamber reverberatory furnace is called "*wet-hearth*". In this, scrap is simply dumped or loaded into the melting chamber, the furnace opening is closed, and process begins. When the molten metal reaches the desired temperature, it is either pumped out or tapped from a hole in the bottom. Burners are mounted at the opposite end of the furnace from the charge well. A pool of molten metal in the furnace bottom after tapping is conserved to make melting easier of the next charge and to reduce damage to the bottom refractories from the shock of the scrap being dumped in. The most severe limitation of this furnace is the problem of charging through a relatively small opening, even though new furnace designs have incorporated wider doors, charging furnaces this way is slow. The most advanced design of wet-hearth furnace includes side burners and a removable top. Other limitations of wet-hearth furnaces are the poor thermal efficiency, poor heat transfer to the charge, low melting rates, high melt loss rates, especially for smaller scrap, difficulty in sealing the furnace and contamination from metallic impurities in the scrap. As a result, wet-hearth furnaces are best suited for melting good-quality scrap, such as sows from sweat furnaces, large

castings, and other bulky uncontaminated scrap. Figure 2.13 shows a generic scheme of reverberatory wet-hearth melting furnace.

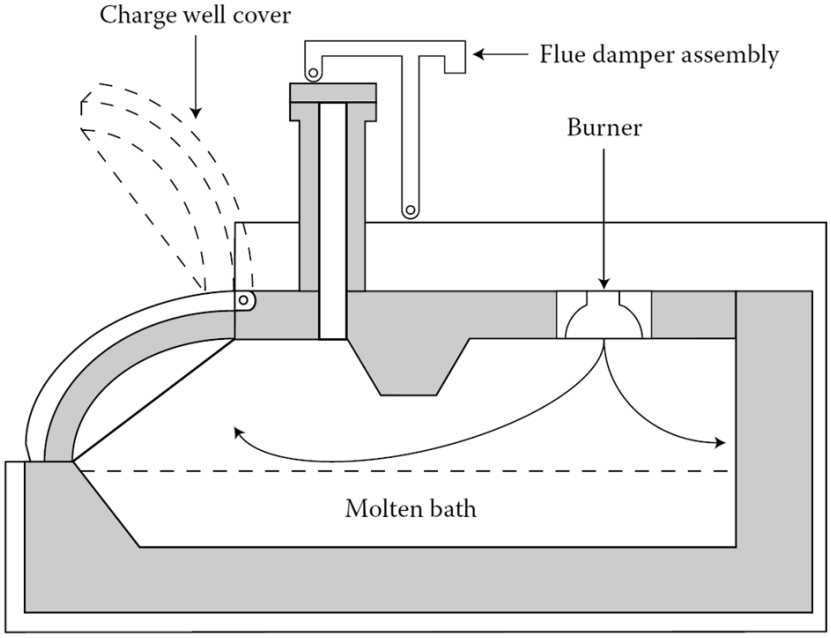

Figure 2.13. Generic reverberatory wet-hearth melting furnace (Schlesinger, 2006)

2.6.1.3 Dry-hearth

Dry-hearth furnace features a sloping hearth, onto which solid scrap is placed for initial heating. As the metal melts, it drains down the hearth into the bath, leaving other metallic materials behind. Figure 2.14 shows a sketch of a typical dry-hearth furnace.

The scrap also dries during the heating process, reducing the possibility of explosions and reducing the potential for melt loss from interaction between the metal and water vapor. Also, convective flames are used in the dry hearth area to maximize heat transfer to the solid scrap; flat luminous flames work better to heat the molten metal. Top-loading dry-hearth furnaces are widely used to maximize capacity. As a result, dry-hearth furnaces are the most popular approach for melting large or bulky scrap.

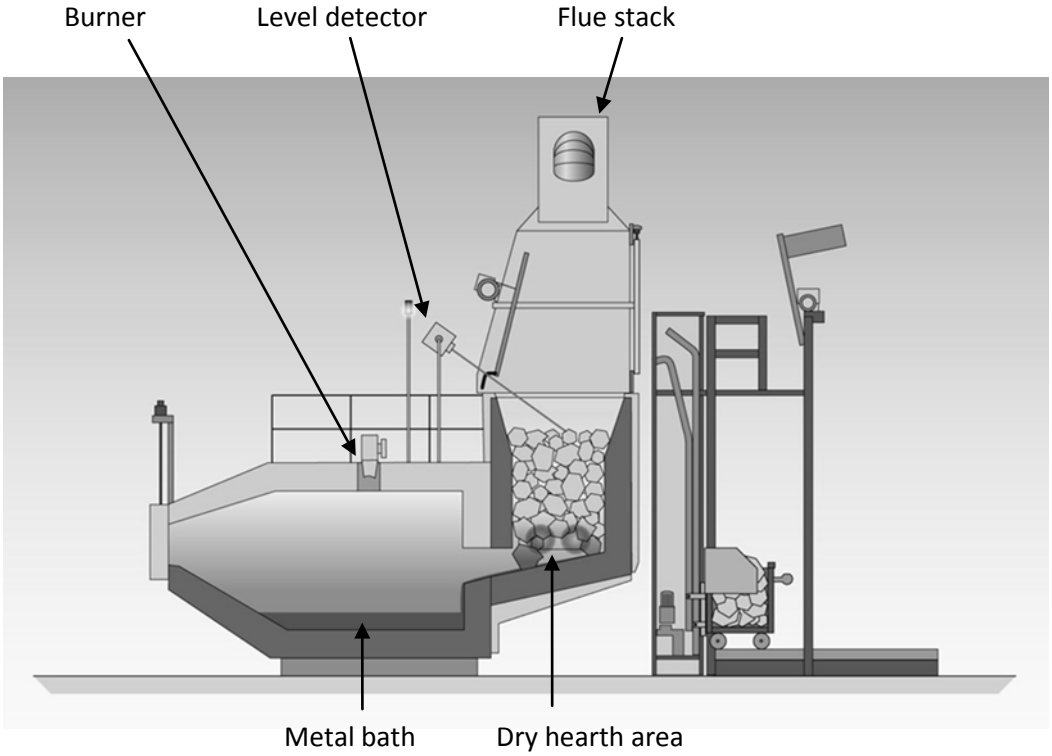

Figure 2.14. Sketch of dry-hearth melting furnace-Adapted from StrikoMelter (2013)

2.6.1.4 Stack melter

An improvement of the dry-hearth furnace is the stack melter shown in Figure 2.15. As the heated scrap descends to the sloping hearth, additional burners melt it, causing it to flow into the molten bath. This in turn allows more scrap to descend to the hearth, creating a semicontinuous melting operation.

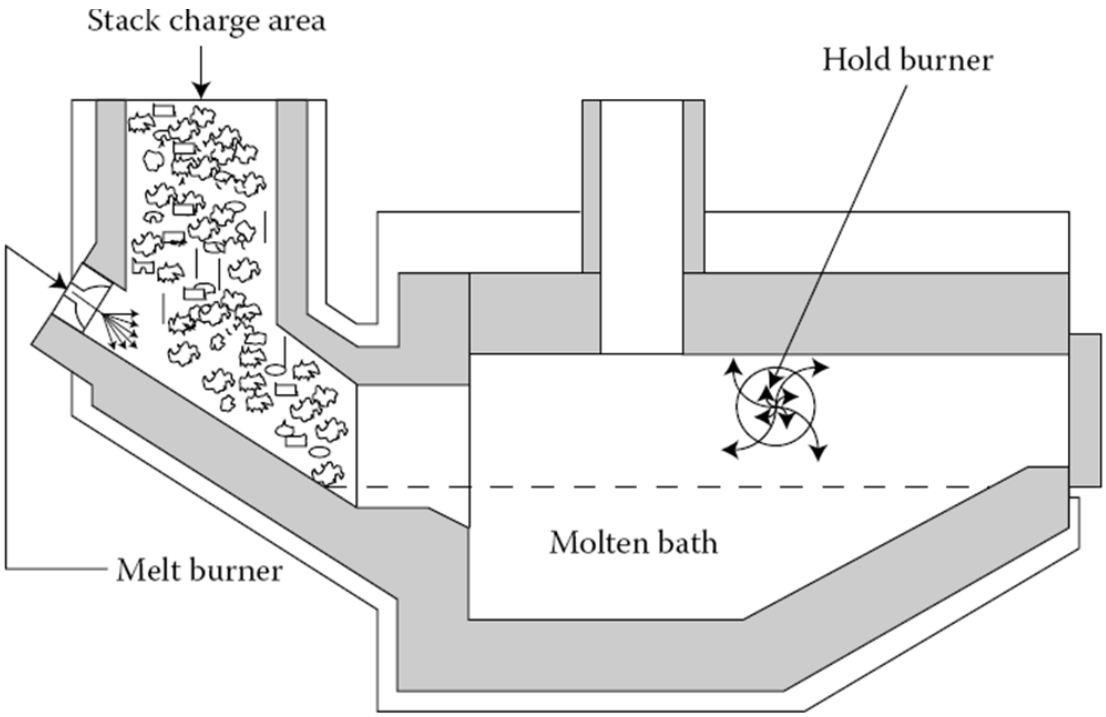

Figure 2.15. Sketch of stack melter (Schlesinger, 2006)

Stack melting has higher efficiency compared with traditional wet- or dry-hearth melting. The high preheating of the scrap by the exhaust gas also reduces melting time on the hearth, improving furnace productivity. Stack melting is not suitable for very large scrap, but a stack can be combined with a dry hearth to accommodate a range of charge materials. These advantages often justify the additional investment required for a stack melter. The main disadvantage is controllability; scrap descends as quickly as it melts, which makes slowing down the melting rate difficult.

2.6.1.5 Tower melter

The pressure of the scrap on the stack limits the depth to which it can be stacked, and this in turn limits the time that it can be preheated. The most advanced design of single chamber furnaces is the tower melter; the tower through which exhaust gas flows consists of several chambers separated by cast iron bars. Scrap is introduced into the top chamber while melting is completed in the furnace hearth below. When metal is tapped from the furnace, the bars on each chamber are sequentially released, and the scrap falls into the next chamber. The design allows a greater amount of scrap to be held in

the column, improving heat recovery and ultimately furnace efficiency. However, tower melters have higher capital costs than other furnaces, and the number of moving parts is a potential maintenance problem.

2.6.1.6 Sidewell furnace

The sidewell furnace avoids the direct interaction between combustion gases and solid scrap, which increased melt loss and dross generation. Instead, only the molten metal in the clean chamber is heated. The superheated molten metal flows underneath a baffle and contacts solid scrap charged to the side well, heating and ultimately melting it. When the charge is melted, the molten metal is then reheated to pouring temperature and tapped, and the process is repeated.

Sidewell furnaces are an effective way to melt light scrap such as UBCs, but fuel efficiencies are poor due no preheating of scrap is provided, a bigger problem has been the slow kinetics of melting limited by the rate at which metal can flow under the baffle to contact the scrap in the well. Even though the sidewell furnace prevents direct exposure of the scrap to combustion flames, the finely divided material oxidizes sufficiently during heating to generate a significant amount of dross. Figure 2.16 shows a sketch of a simple sidewell furnace.

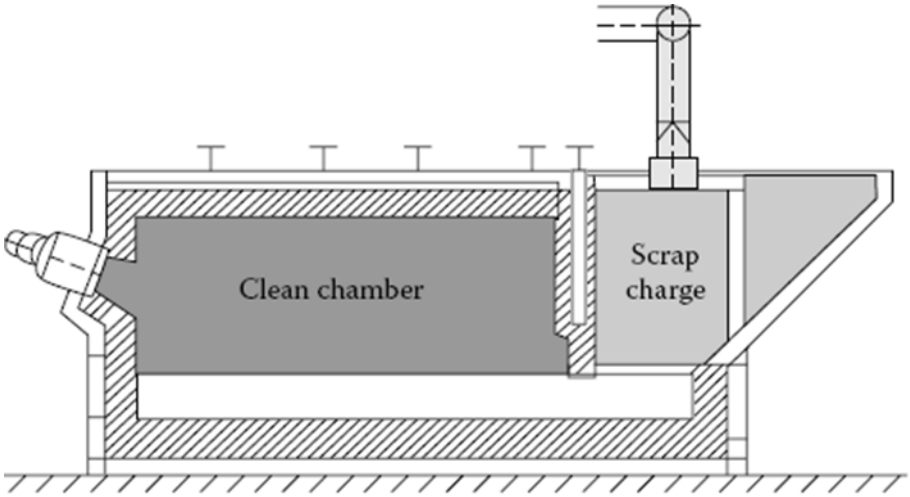

Figure 2.16. Sketch of sidewell furnace (Schlesinger, 2006)

Several methods have been developed to submerge the pieces of scrap in the molten metal in the sidewell while they melted, which would minimize oxidization of the scrap

and eliminate the need for fluxing. An example is that presented in Figure 2.17; here a mechanical pump is used to pump superheated molten metal into a vortex chamber.

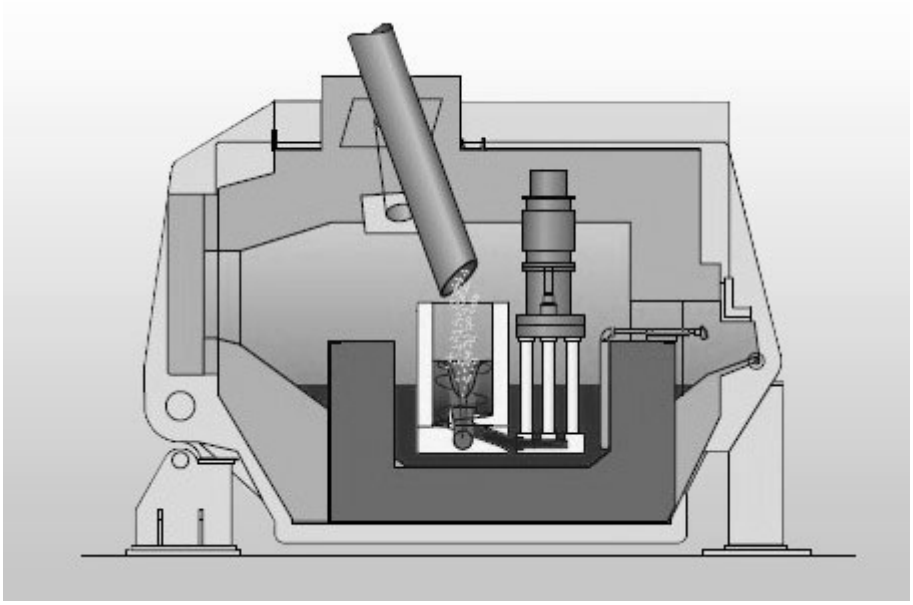

Figure 2.17. Sketch of sidewell furnace with scrap submergence system and mechanical pump (StrikoMelter, 2013)

2.6.1.7 Rotary furnace

For highly oxidized scrap or with low thickness, the use of flux during melting is a requirement. Separating the resulting salt slag from the metal is difficult without sufficient agitation. The most used furnaces for this kind of applications are the rotary furnaces. They are longs sloping tubes, tilted back for charging and firing and tilted forward for slag and molten metal discharge. Typically, these furnaces have the capacity to process 1-10 metric tons of dross or scrap per cycle and burn fuel as the energy source. The salt fluxes that are composed of NaCl and KCl mixtures, should have the following characteristics: melting point below 720ºC; low viscosity; easily detachable from the liquid bath; must not react with the metal; must not add impurities into the metal; must not be hygroscopic; low vapor pressure; low cost; and low treatment cost (Totten and MacKenzie, 2003b, Zhou et al., 2006).

When the contents have reached the desired temperature, the furnace is tilted and the metal and salt slag are poured off. Rotation of the furnace is slow during the early stages

of the melting process, to prevent damage to the refractories from large pieces of scrap or dross; as a molten pool begins to form the speed is increased.

The main advantages of the process using rotary furnaces and salt fluxes are the low-cost energy source (fossil fuel), the low initial investment, and the ease of operation. The main inconvenience of this process is the production of a sub-product that contains salt and needs to be treated before the final disposal. Figure 2.18 shows a sketch of the rotary furnace.

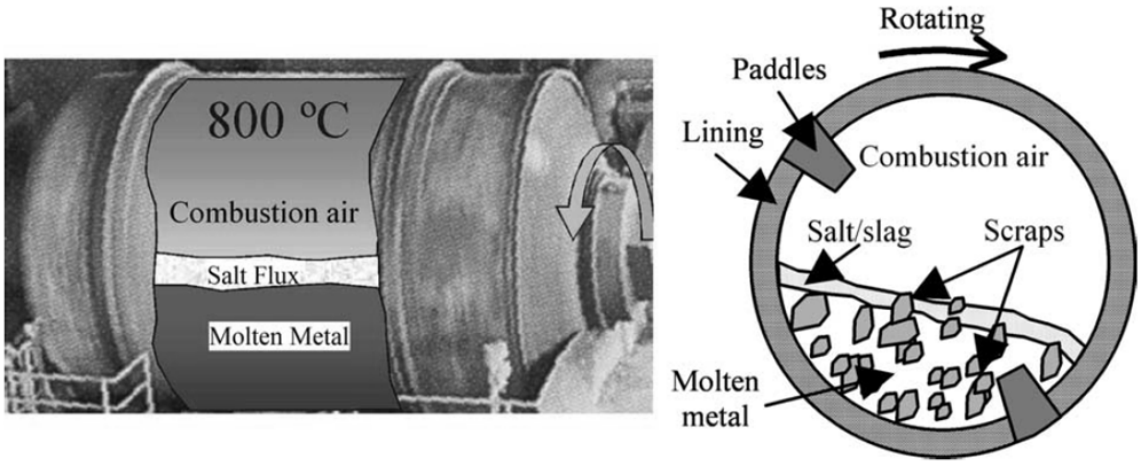

Figure 2.18. Sketch of the rotary furnace (Zhou et al., 2006)

Rotary furnaces are faster and more efficient than ordinary reverberatory furnaces. However, they are also more expensive to install and more difficult to maintain. As a result, they are generally best suited for recovery aluminum from dross and other oxidized old scrap. In practice, smelters use the rotary furnace in their facilities to process any types of scrap.

2.6.1.8 Crucible furnaces

The major application of crucible furnaces is in small capacities. The advantages of crucible furnaces are their simple operation and maintenance and the low capital investment involved. With a furnace concept on the basis of crucible furnaces the foundry can also produce different Alloys in small lots. There are virtually no restrictions as to the type of alloy. The melt can be treated right in the crucible and, if necessary, the alloy can be easily and quickly exchanged.

In the most advanced combustion crucibles, the heating is by means of gas or oil burners that heat the metal in the crucible from outside with spiral guides around the outside; these increase the length of time that combustion gases remain in contact with the crucible. The combustion products do not have contact to the melt. The burner is arranged in the lower part of the furnace shell, the flue gases pass through the flue passageway to a flue duct. Figure 2.19 shows the operation principle of this kind of crucibles.

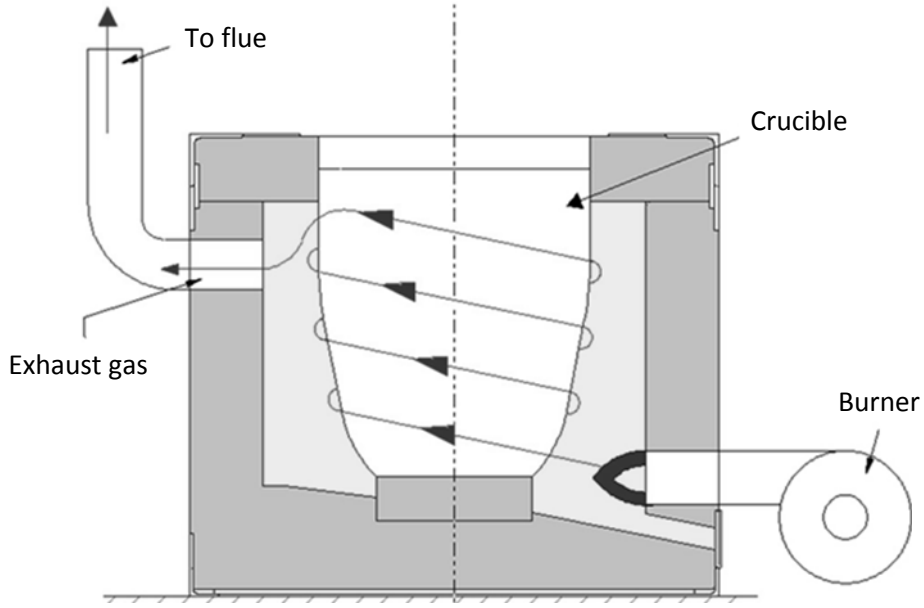

Figure 2.19. Schematic design of a gas-heated crucible-Adapted from Nabertherm (2013)

Instead combustion heating, the crucible furnace can be heated by means of electrical resistance heating elements. This results in very good temperature distribution whitin the liquid metal bath.

For larger production volumes crucible furnaces are no longer an economic option. This is mainly due to the relatively high specific energy consumption and the manual operation of the furnaces. Moreover, only completely dry metal may be added to the charge, as moist material may lead to explosions and hazardous situations for the operators.

2.6.1.9 Coreless induction furnaces

The induction furnace comprises a crucible made of refractory material that contains the metal. A power coil surrounds this crucible; it carries a large alternating electric current which establishes an alternating magnetic field. The field induces electric currents called eddy currents, in the metal bath. Figure 2.20 shows schematically the eddy current effect and construction of a typical coreless induction furnace.

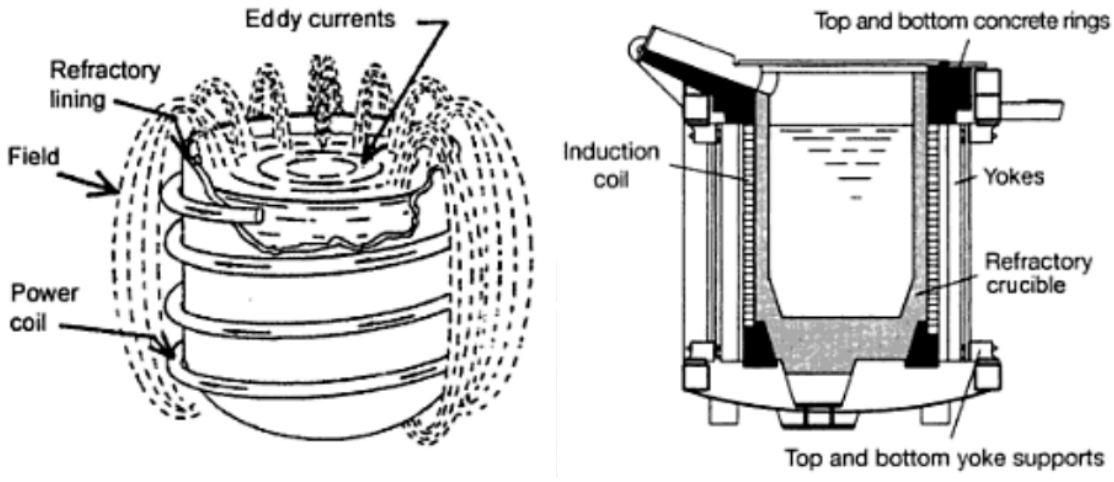

Figure 2.20. Scheme of the eddy current effect (left) and coreless induction furnace (right)-Adapted from Schmitz (2006)

Eddy currents heat and finally melt the bath by Joule effect. The power coil reaches high temperatures and must be cooled; therefore these electrical conductors consist of water-cooled copper tubing. The magnetic field generated by the coil is equally strong on both sides; to prevent the stray flux from heating the outer furnace shell, a series of vertical laminations of transformer iron known collectively as the yoke is located outside the coil. These yokes also eliminate the generation of a high magnetic scatter field and heating up of the furnace structure.

It may be necessary to retain a certain amount of metal in the furnace to continue the operations since it is difficult to start the furnace with small particles, such as turnings or borings, in a cold crucible. As a result, it is general practice to retain a heel in the furnace that may be as much as one-third of its molten metal volume.

Coreless induction furnaces are particularly attractive for melting charges and alloys of known analysis; in essence the operation becomes one the metal melting with rapidly absorbed electric heat without disturbing the metallurgical properties of the initial charge. Also, it is ideally suited to melt scrap with high specific surface area since there is no contact with combustion products. The material must be dry and de-coated. It is of no use to melt ingots or similar size material in an induction furnace.

The coreless induction furnace is very useful for the production of high quality alloys. All means of treatment to clean the melt can be carried out in the furnace. However, throughout, energy and investment costs limit the application in aluminum foundries. Crucible induction furnaces must be reduced in size to compensate the economic cost and technical requirements.

2.6.1.10 Chanel induction furnaces

Figure 2.21 shows a scheme of a channel induction furnace. The most significant is that the channel is placed outside the coil, whereas the metal in a coreless induction furnace is placed inside the coil. To redirect the magnetic field generated by the coil to act entirely on the metal in the channel, an iron core is placed inside the coil. This serves the same function as the iron yoke placed outside the coil in a coreless unit.

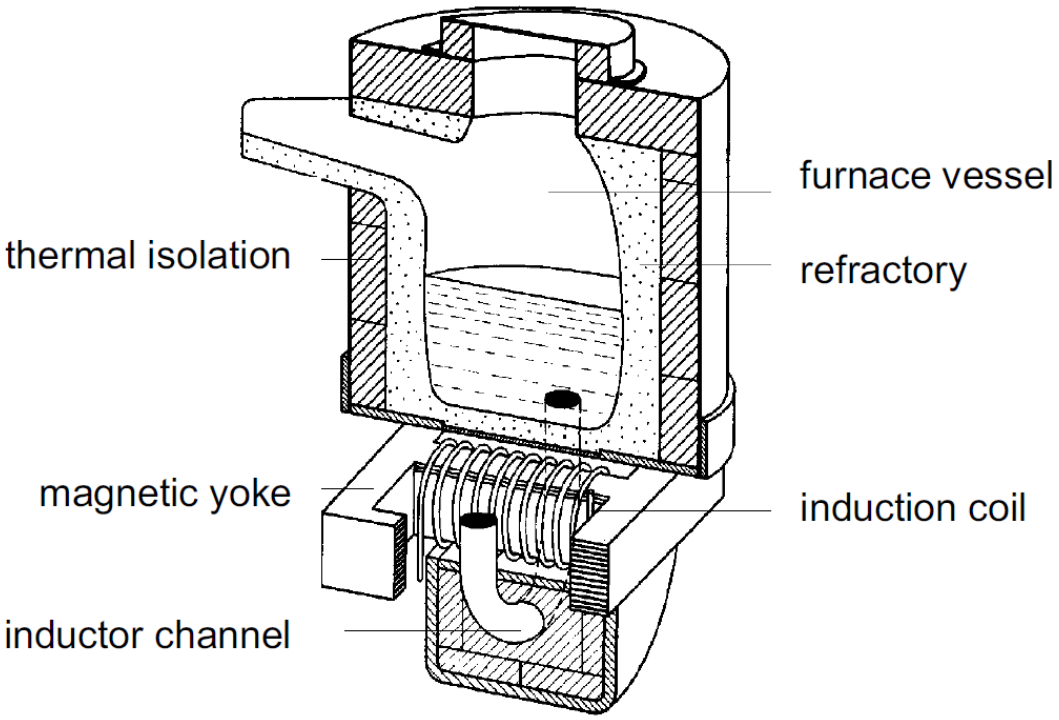

Figure 2.21. Scheme of the channel induction furnace (Langejürgen et al., 2008)

The amount of metal in the channel surrounding the coil is much smaller than the amount of metal being acted on by the field in a coreless unit. As a result, channel furnaces heat metal by an indirect method. Metal flowing through the channel is superheated by the field and moved along by the same forces that cause bath circulation in coreless units. As the superheated metal exits the channel into the main body of the furnace, it transfers heat to the rest of the melt. Scrap or ingot fed to the furnace is melted by this indirect approach, rather than going through the channel.

Chanel induction furnaces can be built in very sizes since more than one inductor can be attached to the furnace bottom.

2.6.1.11 Plasma torch furnaces

There are plasmas of many different types and properties, but in melting applications are only important the thermal plasmas, which in this field are also called plasma torches. Arc plasma torches have three main components: the cathode, the plasma-forming gas injection stage, and the anode. Thermal plasma systems fall into two

categories, namely transferred-arc and non-transferred-arc devices, these are shown in Figure 2.22. In the transferred arc one of the electrodes is the object to be heated. In a non-transferred arc, the arc remains within the plasma torch and is not transferred externally, the anode usually also acts as arc constrictor.

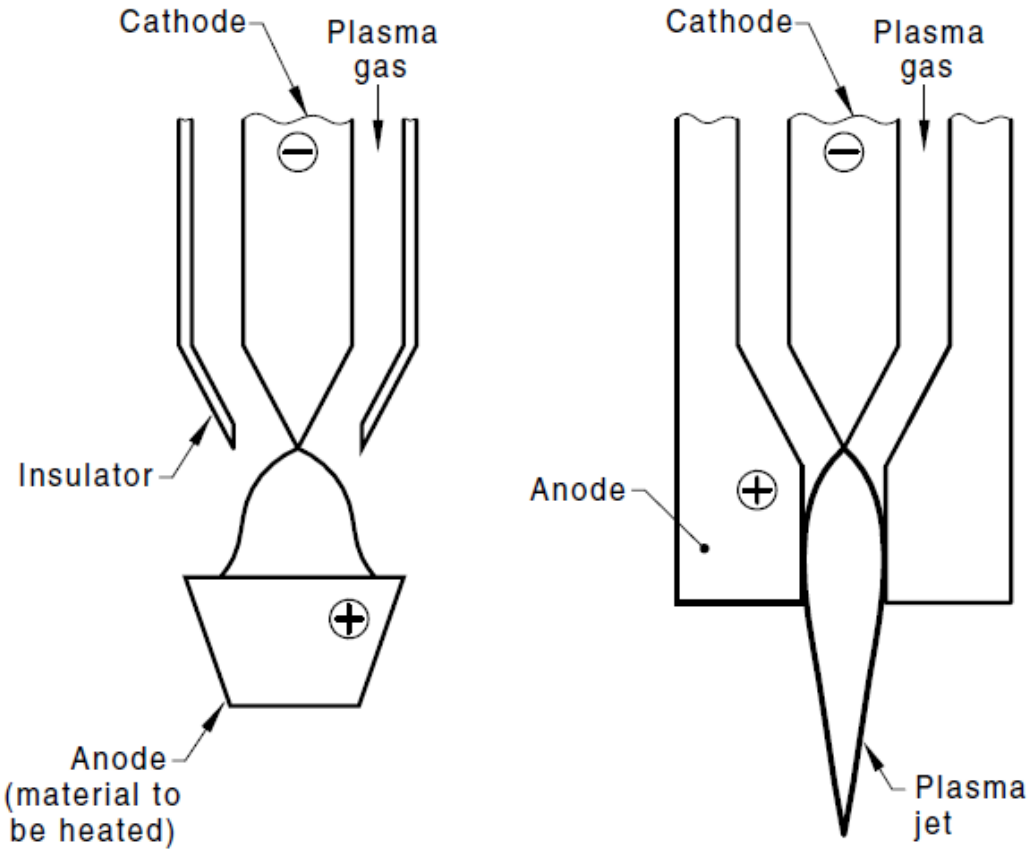

Figure 2.22. Thermal plasmas: transferred-arc (left) and non-transferred-arc (right); adapted from Murphy (2001)

Inside the torch, the working gas flows around the cathode and through a constricting tube or nozzle. The plasma is initiated by a high-voltage difference that creates a conductive path for an electric arc to be formed between the cathode and anode. The electric heating produced by the arc causes the gas to reach very high temperatures (e.g. more than 10000 K), thus to dissociate and ionize. Several features and applications of the most applied atmospheric pressure plasmas are discussed in detail by Tendero et al. (2006).

Non-transferred arc torches are typically used in applications that rely on the formation of a plasma jet with moderate to very high velocity and, its use as a heat source, high-temperature processing medium, or source of specific reactive species, such as plasma spraying and powder synthesis. Transferred arc torches are mostly used in applications that maximize the utilization of heat from the plasma, such as plasma cutting, welding, and metallurgy (Trelles et al., 2009). By this reasons, currently the melting furnaces heated by plasma torches are in transferred arc configurations. Recently, the European Union through the EDEFU project (EDEFU, 2010) of the seventh framework programme, has promoted the development of new prototypes of melting furnaces that can use thermal plasmas as a heating means. However, this technology is still developing and there are not widely used commercial devices.

In plasma torch melting furnaces for aluminum, inert gas as argon or nitrogen must be employed in order to prevent the oxidation of the load. The main advantages of this process in comparison with conventional rotary furnace are that the final dross has no salt content, better heat transfer, low times of melting and less amount of generated gases. On the other hand, the main shortcomings are the use of electric energy, the process needs trained people to operate and maintain the system, and the large cooling requirements that can represent a considerable loss of energy. Figure 2.23 shows a scheme of a transferred arc furnace.

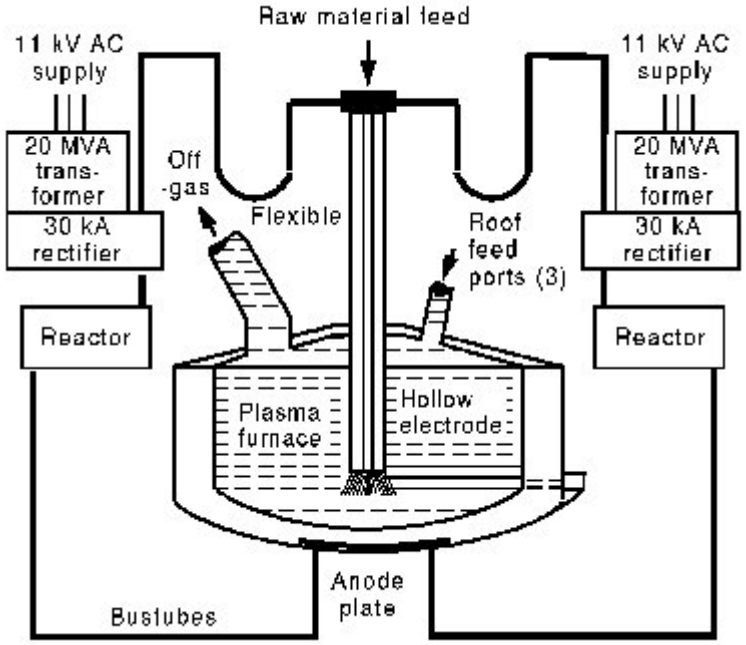

Figure 2.23. Schematic arrangement of transferred arc furnace; Adapted from Jones et al. (2001)

2.6.2 Holding furnaces

In smaller melting facilities, molten metal tapped from a melting furnace is usually transferred to a ladle prior to casting. Larger facilities often employ a holding furnace, where the temperature and composition of the metal can be adjusted. This allows the melting furnace to be used mostly for its intended purpose of increasing productivity. The use of a holding furnace also makes it possible to operate the melting furnace under conditions that most favor heating of solid scrap (reducing condition, convective heat transfer), improving the efficiency and melting rate.

2.6.2.1 Reverberatory furnaces

Many different holding furnaces are available; the most widely used are the reverberatory furnaces with both gas-fired and electric furnaces. Figure 2.24 shows a commonly used reverberatory furnace operating under luminous flame conditions. The main advantage is their low cost, but high oxidation and melt losses presented prevent the intensive use in secondary production.

Figure 2.24. Reverberatory furnace heated by direct combustion flame (StrikoMelter, 2013)

To prevent the direct contact of the combustion gases and the load, the radiant tube furnaces are widely used. Figure 2.25 presents a furnace using this principle. In this furnace the products of combustion are passed through ceramic tubes mounted in the furnace; as the tubes heat up, they radiate energy to the molten metal below. Electrical resistance elements mounted inside the radiant tubes have the same effect.

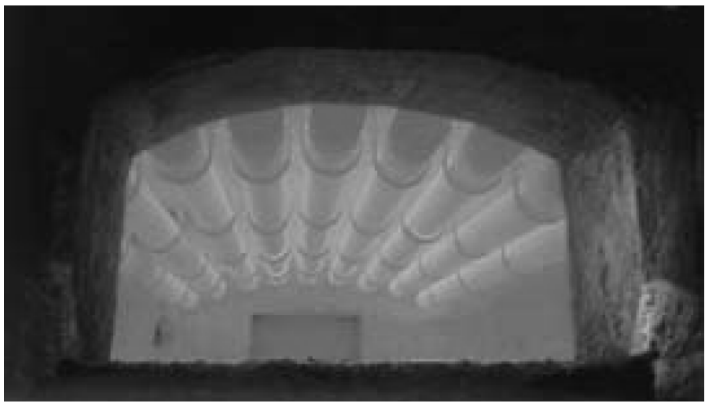

Figure 2.25. Radiant tube in reverberatory furnace (Khanthal, 2011)

2.6.2.2 Crucible furnaces

Crucible furnaces also are used for holding applications especially in small capacities. They are used as holding furnaces in sand or die casting plants; they are ideally suited for metal treatment. For operation, the crucible is filled with liquid metal followed by the

required metal treatment and temperature adjustment. After thorough metal treatment, an excellent metal quality is obtained.

2.6.2.3 Electrical furnaces

Generally, the electrical furnaces are used in applications of smaller size than the crucible furnaces. Electric resistance furnaces feature a wire element looped throughout the sides of the furnace. The elements in most resistance furnaces are made of the nickel–chromium alloy nichrome or aluminum–chromium alloy aluchrom. The element is often installed as an open-coil element supported on high-purity ceramic tubes; elements can also be obtained semiembedded in refractory panels, which are simply swapped out when the element fails. Other option is to install the resistances in the roof. Figure 2.26 shows an electrical furnace heated from lateral walls and another heated from the roof.

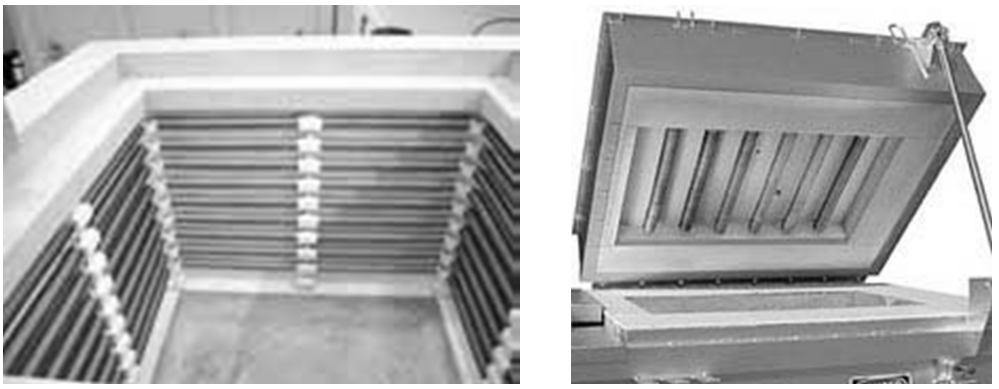

a) b)

Figure 2.26. Electrical holding furnaces: a) heated from lateral walls (Nabertherm, 2013) b) heated from the roof (SPX, 2013)

A special design is the immersed electric furnace; Figure 2.27 shows this kind of application where high efficiency is obtained.

Figure 2.27. Electric immersion holding furnace (SPX, 2013)

2.6.2.4 Induction furnaces

Induction furnaces are used also in the holding stage. Channel furnaces are used more often as holding furnaces, rather than as melting units, and typically for larger operations. In spite of some limitations, from the mechanical and operational point of view the channel induction furnace is the ideal holding furnace. There is no contact with combustion products nor with ambient air. The eddy currents in the inductors cause a through stirring effect which creates a good mixture of all alloying components with the result of a homogeneous melt. Also very good temperature distribution is obtained over the entire bath which is easy to maintain during casting. Their efficiency is typically 70 to 75%, compared with the 50 to 55% efficiencies of coreless furnaces. A second advantage is the reduced agitation in channel furnaces. However, channel furnaces are more expensive per unit melting capacity than coreless units (and much more expensive than fossil-fuel furnaces).

2.7 Motivation

Aluminum is a metal used in a wide variety of applications through all sectors due to their good properties. The secondary aluminum production is a key factor in the global market of this metal. Long product lifetimes and growing markets mean that the future demand will continue to be met from both primary and recycled sources.

The transformation of scrap into recycled aluminum alloys requires approximately only 5% of the energy input needed to produce primary ingot from bauxite. In secondary aluminum production, energy is consumed throughout the refining process, but the key equipments for the metallurgical processing are furnaces. The aluminum secondary industry focuses its efforts in develop a method for recycling the metal that be economically competitive and satisfies the requirements of the market. Several furnace types are developed for the different applications and conditions. Nevertheless, traditional design of melting and holding furnaces has been based on semi-empirical methods due to the complexity of the phenomena involved, which has limited the use of computational techniques based on first principles physics. In addition, the inherent difficulty and shortcomings of experimental measurements do not allow a comprehensive description of the operation. Accordingly, a great deal of information has been missing in these kinds of devices.

Some companies have developed some simplified numerical models of their units. As in the case of Kanthal; which simulate their holding furnace heated by radiant tubes in a simplified 2D domain (Figure 2.28).

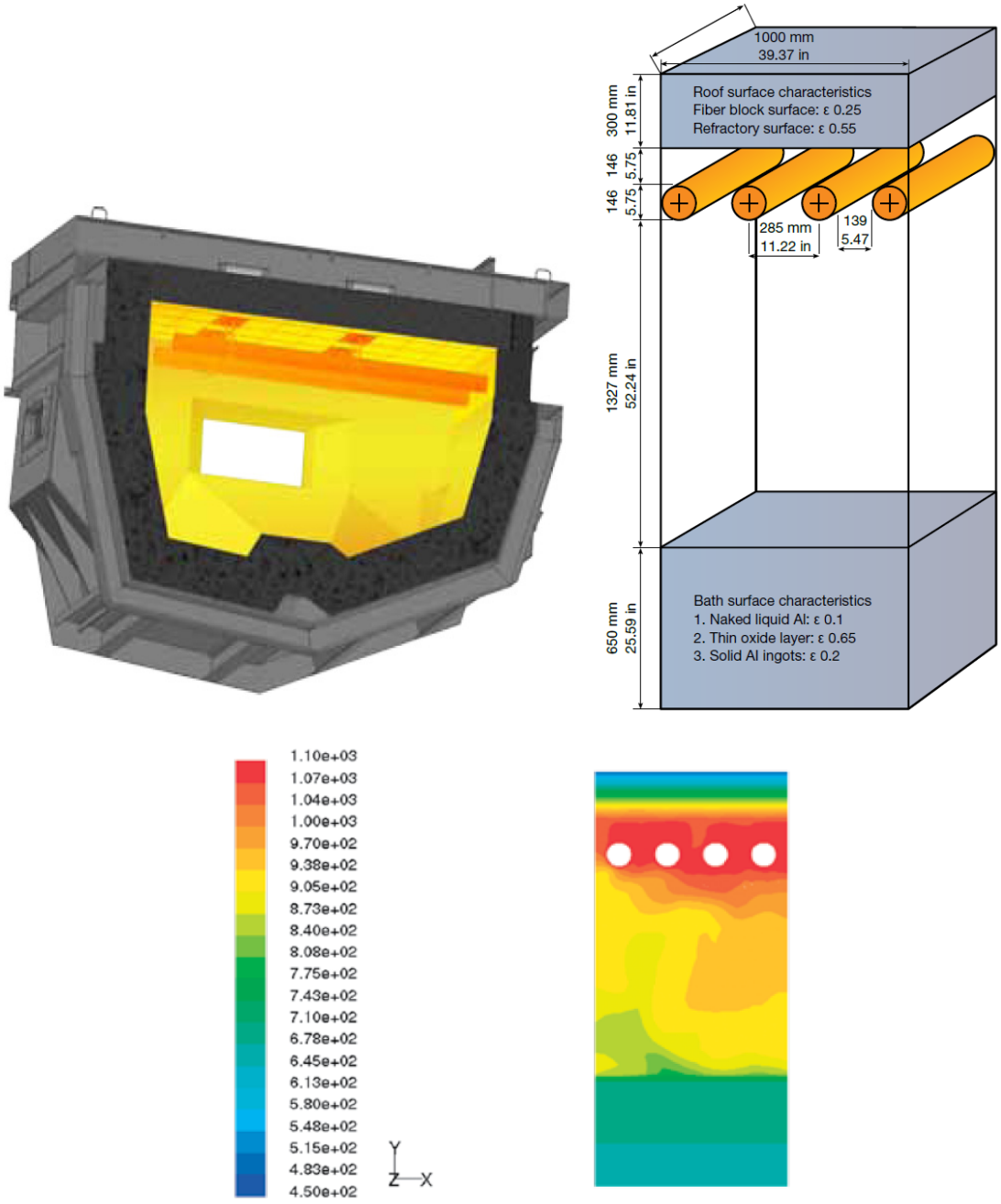

Temperature distribution (in °C) inside the furnace.
Roof surface emissivity = 0.25, aluminum bath emissivity = 0.1.

Figure 2.28. 2D numerical simulation of a industrial holding furnace heated by radiant tubes (Khanthal, 2011)

Nevertheless, the use of numerical techniques is not a common practice in the development process of industrial furnaces. In scientific literature, only few works has been published concerning to numerical simulations in melting and holding furnaces. In

melting applications, most works about numerical simulations did not consider the molten load in the furnace and the interactions between heating space and load; others consider the solid–liquid region of the load as a conducting solid with constant thermal properties (i.e. the convection effects are not considered) and neglect the heat losses from the walls. In holding applications, the works that consider the interaction with the molten load have been developed under steady state assumption, others simulations also neglect the conjugated problem, the radiation losses, the three dimensional geometries or the convection effects. Descriptions of the current state of the simulations for melting and holding furnaces will be presented in detail in chapters 4 and 5, respectively; but according to the literature reviews of scientific papers and industrial devices, it is possible to point out that comprehensive simulations with realistic models are still undeveloped for these kinds of devices.

3. Models used in numerical simulations of industrial furnaces

The operation of furnaces relies on the relationship between fluid flow and heat transfer. The laws governing these processes can be represented by a set of partial differential equations. Analytical solution for each particular problem is not available but it is possible to obtain numerical solutions that resemble the exact solutions with a good level of accuracy. Furthermore, numerical simulations often become the most economical and fastest approaches to provide a broad understanding of the practical processes.

What a numerical calculation does is essentially to simultaneously solve the conservation equations of mass, momentum and energy in gases, liquids and solid phases. This is done numerically by (a) adopting an adequate discretization of the geometrical domain and (b) transforming the original partial differential equations into approximate, algebraic counterparts. For present modeling purposes, multi-phase modeling is required for including the interaction between the different domains in the furnaces, i.e. load (liquid-mushy-solid), refractories walls (solid) and the air in cavities (gas). This kind of numerical analysis can be accomplished by either finite volume method (FVM), finite element method (FVM) or boundary element method (BEM). The success of FEM and BEM lies in their ability to handle complex geometries, but their drawback is the high time consuming in terms of computing and programming. Because of their good performance solving thermal-fluid problems and their simplicity in formulation and programming, most commercial codes of computational fluid dynamics (CFD) implement their algorithms with the FVM. Values of thermal variables are

obtained at a large but finite number of discrete points, providing an adequate approximation to the corresponding fields and fluxes.

Several commercial codes have been developed that solve numerically the constitutive equations using the finite difference approximation. In this thesis, the commercial CFD code, FLUENT software version 13.0.0 (ANSYS, 2012) has been used to simulate numerically the melting and holding furnaces.

In the numerical simulations of the furnaces presented in this thesis, the main phenomena considered are the mass, momentum and energy conservation; flows induced by natural convection due to variation of density as function of temperature; conjugated problems and interactions between gas-liquid-solid zones; radiation heat transfer in cavities and phase change.

The flow is governed by the Navier-Stokes equations, which describe the principle of mass and momentum conservation; an additional equation for energy conservation is solved in problems involving heat transfer. These basic equations are commonly presented in works of numerical modeling of flows (Pope, 2000, Ferziger and Perić, 2002).

Variation of density with temperature increases the non-linearity of the equations. It may be possible to ignore the density variations in all terms other than body force in the vertical momentum equation. This method is called the Boussinesq approximation and it allows the equations to be solved by methods that are essentially identical to those used for incompressible flow, but this approach is valid if the density variations are small (Ferziger and Perić, 2002), which is not the present case; therefore, the Boussinesq approximation is not taken for this work. The sequential solution method for a density variable with temperature is accomplished in the same way as the energy equation; i.e. the fluid properties are calculated after each iteration and treated as known during the next iteration. The volume expansion of liquids in gases is typically solved with the method of "Volume of Fluid" (VOF), but this technique is difficult to implement in conjugated problems, so that most commercial CFD codes avoid it. Since the interaction between the refractory walls and the load is a major consideration for the melting and

holding furnaces analyzed, the volumetric expansion effect is neglected for the simulations. In this sense, the air-aluminum interface in the furnaces is fixed and the calculation focuses on material fusion, temperatures and losses. Since this assumption avoids the numerical computation in each time step of the geometric interactions in the gas cavity, which is very costly in computational terms, it is possible in return to take into account the heat losses from the top of the load by radiation with a good compromise of computational resources.

In many practical conditions, turbulence has to be modeled to some degree. In these cases, additional transport equations must also be solved. As we will explain in Chapters 4 and 5, we are not concerned in this thesis about turbulent flows. Numerical models are covered widely by Pope (2000) and Ferziger and Perić (2002).

Conjugated problems are referred to when heat conduction in a solid needs to be considered simultaneously with convection in an adjacent fluid. A problem with similar complexity is presented for the interactions between gas-liquid-solid zones. These problems need to be solved by iterating the equations describing the two types of heat transfer.

The core of such simulations of industrial furnaces for melting or holding must include a model for the phase change of the load material. In the following sections, an overview of the numerical methods used in phase change problems and the state of the art of the related simulations are presented. The governing equations considering phase change problems and the methods used for the numerical computations are presented in detail for the most important phenomena involved. Main attention is given to the special models used: i.e. phase change model and losses by thermal radiation.

3.1 Liquid-solid phase change in pure substances and mixtures

In general, the liquid-solid phase could be a function of a number of variables, such as temperature, concentration, cooling rate, etc. In many practical systems, however, the

condition of local thermodynamic equilibrium is satisfied; therefore properties of the material only depend on temperature and pressure for a given composition, and the heat transfer rate is slow enough not to affect the thermal equilibrium. In addition, the properties of solids and liquids are almost independent of pressure. Accordingly, it is reasonable to assume that the liquid fraction is a function of temperature alone (Voller and Swaminathan, 1991).

A chemically pure substance (an element or compound) has a sharp, clearly defined melting point. In phase changes of these substances, the two phases (liquid and solid) are separated by a distinct interface. On the other hand, mixtures change phase over a temperature range, i.e., they start the phase change at a given temperature and do not complete the process until they reach a lower (solidification) or higher (melting) point. The start temperature and range depend on the composition of the mixture. In phase changes of mixtures, the liquid and solid phases are often separated by a mixed-phase region (both liquid and solid coexist), consisting of an intricate mixture of liquid and solid grains of different composition. This zone is commonly termed the mushy zone.

When the mixture is made mostly of metals, this is called an alloy. Many mixtures and alloys have eutectic points for given compositions, at which the mushy zone disappears and the phase change process is performed at a given temperature, in a form similar to a pure substance.

In metallurgical science, the information about how the solid alloy forms, what its chemical composition is and what its microscopic structure will be, are presented in a single (sometime simple) diagram called phase diagram or phase equilibrium diagram.

3.1.1 Phase diagrams for alloys

Many alloys have complicated phase diagrams with several solid phases, which depend of the micro-crystal lattice, promoting the existence of various eutectic points and more solid-solid transitions. A typical illustration of this case is the equilibrium diagram of steels; in their simplest form, steels are alloys of Iron (Fe) and carbon (C). The Fe-C phase diagram is a fairly complex one, but the industrial interest is only for the steel part, so

the metallurgists only consider up to around 7% Carbon. This special diagram is called Iron-Iron Carbide (Fe - Fe_3C) phase diagram and although it is only a part of the original diagram, the Fe - Fe_3C diagram contains all the features indicated above. As many authors, Porter and Easterling (1992) describe and explain this and other phase diagrams in alloys.

Figure 3.1 shows a typical phase diagram for a binary eutectic alloy; this simplified but representative diagram is used to summarize the main information provided in equilibrium diagrams, and their connection with the numerical modeling concerning to this thesis (next section).

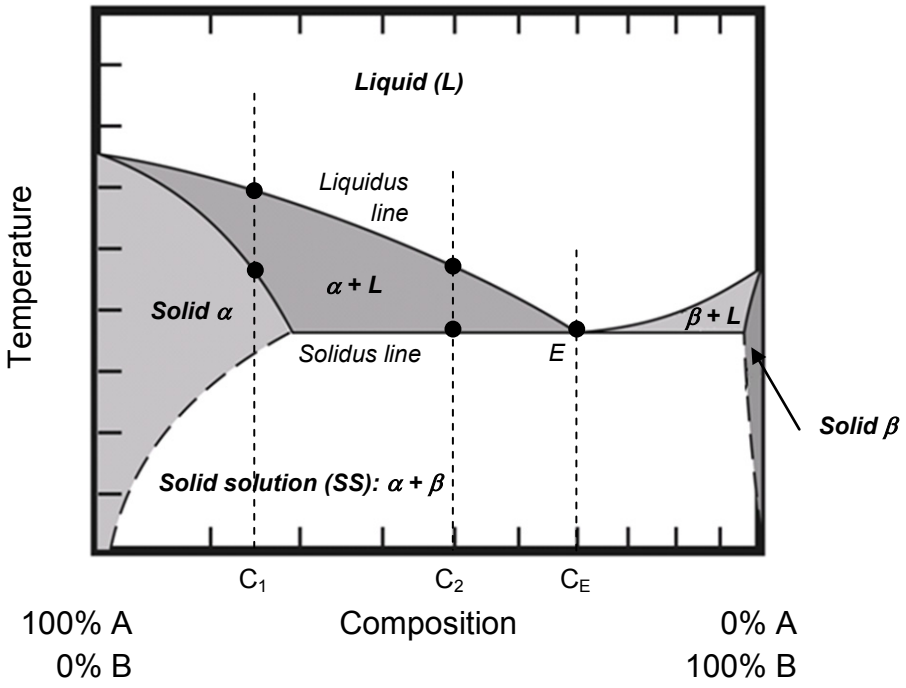

Figure 3.1. Typical phase diagram in a binary alloy

In the phase diagram, the horizontal axis gives the composition of the alloy in percentage of the pure substances A and B. Given a mixture of concentration C_i (weight percent of component B) with uniform temperature *T*, the coordinates C_i and *T* define a point on the phase diagram. The region in which this point is located determines the phase present in the system at equilibrium. In the phase diagram presented in Figure 3.1, *L* denotes the liquid, *SS* the solid solution, $\alpha + L$ a mixture of liquid and a solid in which solid molecules of B are incorporated into the crystal lattice of A, and $\beta + L$ a mixture of liquid and solid in which solid molecules of A are incorporated in the crystal

lattice of B. In this figure, two different types of mushy region zones (α + *L* and β + *L*), three different types of solid regions (*solid* α, *solid* β and *SS*) and only one liquid phase (*L*) are possible during the phase change process depending on the initial concentration. The liquidus line separates the region of pure liquid phase from the mushy zone. The solidus line separates the region of a solid phase from the mush or from another solid phase. At the eutectic point (*E*), there is a unique melting-freezing temperature and there is no mushy zone.

As pure substance A is on the extreme left hand side of the diagram, its melting point can be read off where either the solidus or the liquidus line meets the axis. Similarly the melting point of pure substance B can be read off the right hand side. In addition to the two pure substances, three cases can be defined that involve the phase change for any defined concentration (C_i): C_1, C_2 and C_E, these cases are presented in Figure 3.1 as dashed vertical lines and details of the phase change in each are explained as follows:

The phase change in an alloy with composition C_1 includes the transition between liquid (*L*), mushy region (α + *L*), solid region (*solid* α) and depending of the specific composition, the solid can remain in this phase (*solid* α) or undergo a transition to another solid region (*SS*). The solid-solid phase changes are omitted from the current explanation since it concerns to the casting process, which exceeds the scope of this work. Figure 3.2 shows a close up of the region of liquid-solid phase change of the alloy with composition C_1 (see Figure 3.1).

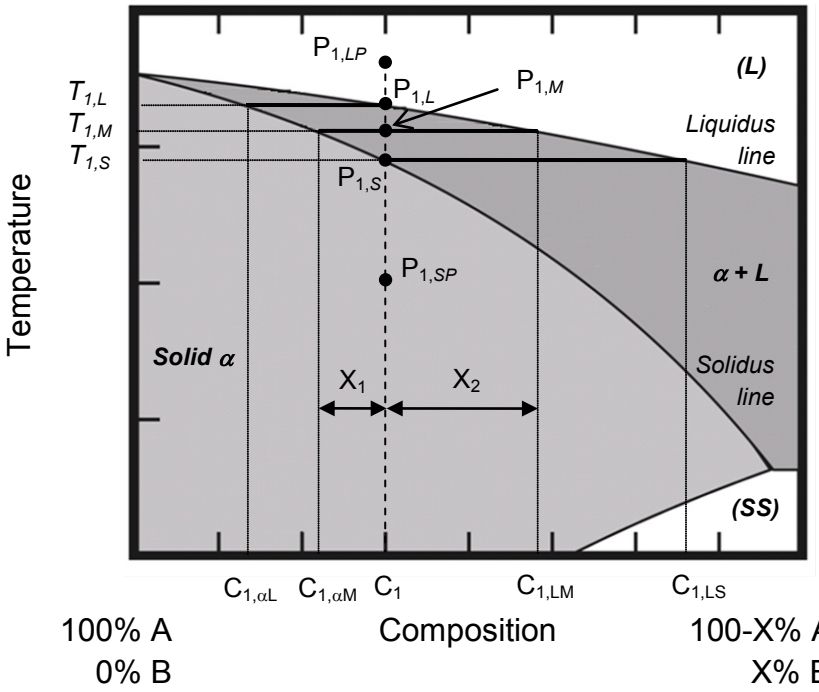

Figure 3.2. Close up of the region of liquid-solid phase change of the alloy with composition C_1 (see Figure 3.1)

In Figure 3.2 the point $P_{1,LP}$ is located above the liquidus line and so the entire mixture is liquid. The liquid cools until it reaches the liquidus line at temperature $T_{1,L}$ (point $P_{1,L}$), grains of *solid* α start to form with a composition of $C_{1,\alpha L}$ % B, 100-$C_{1,\alpha L}$ % A. When the temperature reaches the value of $T_{1,M}$ at point $P_{1,M}$, the grains in the mushy region (α + *L*) being coated with *solid* α with a composition of $C_{1,\alpha M}$ % B, 100-$C_{1,\alpha M}$ % A and the liquid has a composition of $C_{1,LM}$ % B, 100-$C_{1,LM}$ % A. At $T_{1,S}$ (point $P_{1,S}$) the last of the liquid has a composition of $C_{1,LS}$ % B, 100-$C_{1,LS}$ % A and the final grains have an average composition of C_1 % B. The whole phase change process takes place over a temperature range of $T_{1,L}$ - $T_{1,S}$.

The liquid fraction of the mushy regions are computed through the inverse lever rule, which is applied to any phase change as the average of two homogeneous phases. Therefore the liquid fraction (LF) of a point $P_{1,M}$ located in the mushy region (α + *L*) is (Porter and Easterling, 1992): $LF = X_1/(X_1+X_2) = (C_1 - C_{1,\alpha M})/(C_{1,LM} - C_{1,\alpha M})$; and the solid fraction (SF) of the same point is: $SF = X_2/(X_1+X_2) = (C_{1,LM} - C_1)/(C_{1,LM} - C_{1,\alpha M})$.

The phase change for an alloy with composition C_2 is similar to that of the alloy with composition C_1, but in this case the solidus line coincides with the eutectic temperature and made different the process in this part. The phase change includes the transition between liquid (*L*), mushy region (α + *L*) and solid region (*SS*). Figure 3.3 shows the region of liquid-solid phase change of the alloy with composition C_2 (see Figure 3.1).

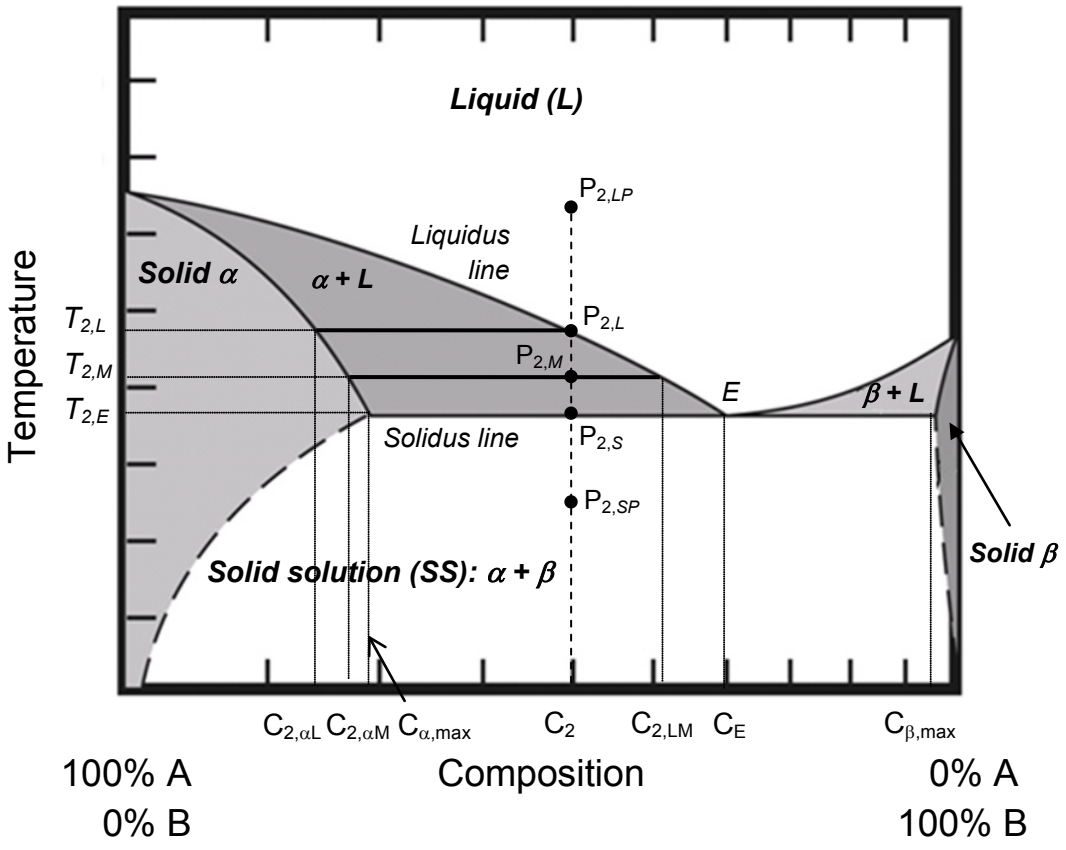

Figure 3.3. Region of liquid-solid phase change of the alloy with composition C_2 (see Figure 3.1)

The phase change shown in Figure 3.3 for an alloy of composition C_2 follows a similar process than that shown in Figure 3.2 for the corresponding points $P_{2,LP}$, $P_{2,L}$, and $P_{2,M}$ (liquid to mushy zones). At the eutectic temperature $T_{2,E}$ (point $P_{2,S}$), the last of the liquid has a composition of C_E % B, 100-C_E % A (point *E*). It might be expected that the grains be composed of C_2 % B, but this is not the case since the maximum B content of *solid* α is $C_{\alpha,max}$ %. Instead, *solid* β starts to form in the liquid with a composition of $C_{\beta,max}$ % B, 100-$C_{\beta,max}$ %. The liquid-solid phase change process takes place over a temperature

range of $T_{2,L}$ - $T_{2,E}$. The results of the cooling process so far are grains of *solid* α ($C_{\alpha,max}$ % B, 100- $C_{\alpha,max}$ % A) with patches of layered $\alpha + \beta$. But even though the alloy is solid the process still hasn't finished. As the material cools to room temperature the *solid* α can hold on to less and less substance B, and the same process happens with the *solid* β. This is shown by the curved, dashed lines beneath the solidus line.

The phase change presented for the left side of the eutectic point *E* (i.e. the *solid* α and mushy zone $\alpha + L$) is also valid for the right side of *E* (i.e. the *solid* β and mushy zone $\beta + L$).

Finally, a particular concentration of the alloy is the eutectic composition (C_E), since the liquid cools down to the point marked *E* at a temperature T_E and stays there. At some points in the liquid grains of *solid* α start to grow and at others, grains of *solid* β are created. The entire process happens at the fixed temperature T_E. Once the alloy is fully solid the temperature can begin to drop again.

3.1.2 Phase diagrams of alloys -towards modeling

Figure 3.4 shows the evolution of the liquid fraction with temperature for the binary eutectic alloy. On the one hand, isothermal curves represent the solid-liquid phase change of the two pure metals and the alloy of eutectic composition, where the latent heat is evolved at a unique temperature; T_{melt} and T_E are the melting and the eutectic temperatures of the material, respectively. On the other hand, the solid-liquid phase change process for alloys is performed in a temperature range, between the solidus temperature (T_S) and liquidus temperature (T_L), given by the solidus and liquidus lines, respectively. In this case, the liquid fraction is computed from the inverse lever rule presented in the previous section. This results in several relations between the liquid fraction and temperature. Voller and Swaminathan (1991), Swaminathan and Voller (1992) and Swaminathan and Voller (1993) have developed models to implement cases of potential relations and combinations of eutectic and linear relations, but in practical terms and with the purpose to reduce the computational cost, the relation between the liquid fraction and temperature for mixture substances is simplified typically as a linear

function (Hu and Argyropoulos, 1996). Currently, only this relation is included in commercial codes (ANSYS, 2012, CD-ADAPCO, 2004).

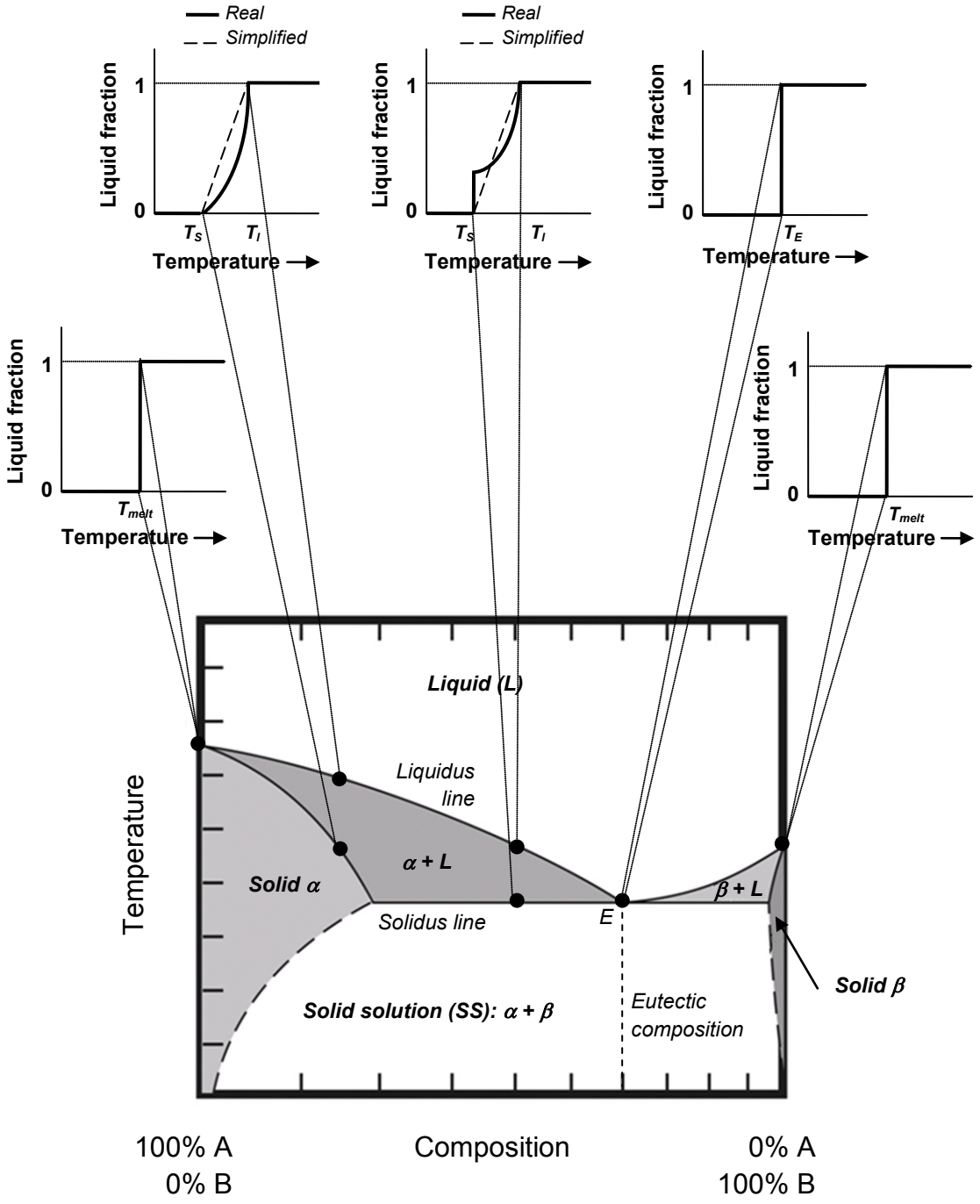

Figure 3.4. Liquid fraction evolution with temperature for a binary eutectic alloy

3.2 Numerical models for phase change problems

In the general case the phase change of the load material depends on time and space and originates a phase-separating boundary moving within the medium during the process. Transport properties vary considerably between phases, resulting in totally different rates of energy, mass and momentum transfer from one phase to the other. The position of this moving boundary cannot be identified in advance, but has to be determined as an essential constituent of the solution. The term “moving boundary problems” is associated with time-dependent boundary problems, where the position of the moving boundary must be determined as a function of time and space. Moving boundary problems are also referred to as Stefan problems (Hu and Argyropoulos, 1996). Phase change methods are divided into three main categories: analytical, variable grid and fixed grid methods. The last two approaches make use of numerical simulations.

3.2.1 Analytical methods

The simplified analytical methods offer an exact solution and are mathematically elegant. However due to their limitations, analytical solutions are mainly used in 1D cases of an infinite or semi-infinite region, with simple boundary conditions and constant thermal properties. These evidently entail important simplifications, related to geometry and physical properties of the distinct phases, that prevent their use in almost all practical problems of solidification and melting, but the analytical solutions developed serve as a cornerstone of this discipline and are still used today as standard references to validate the numerical models. In order to appreciate the complexity of the fundamental physics and understand the method adopted in this work, the theory of liquid-solid phase change for unidirectional problems, in a pure substance without liquid movement is presented (Alexiades and Solomon, 1993, Hu and Argyropoulos, 1996, Poulikakos, 1994).

Focusing on the melting or freezing front, Figure 3.5 shows such a front separating a solid from a liquid region, the horizontal dashed lines represent an infinitely thin control volume surrounding this front.

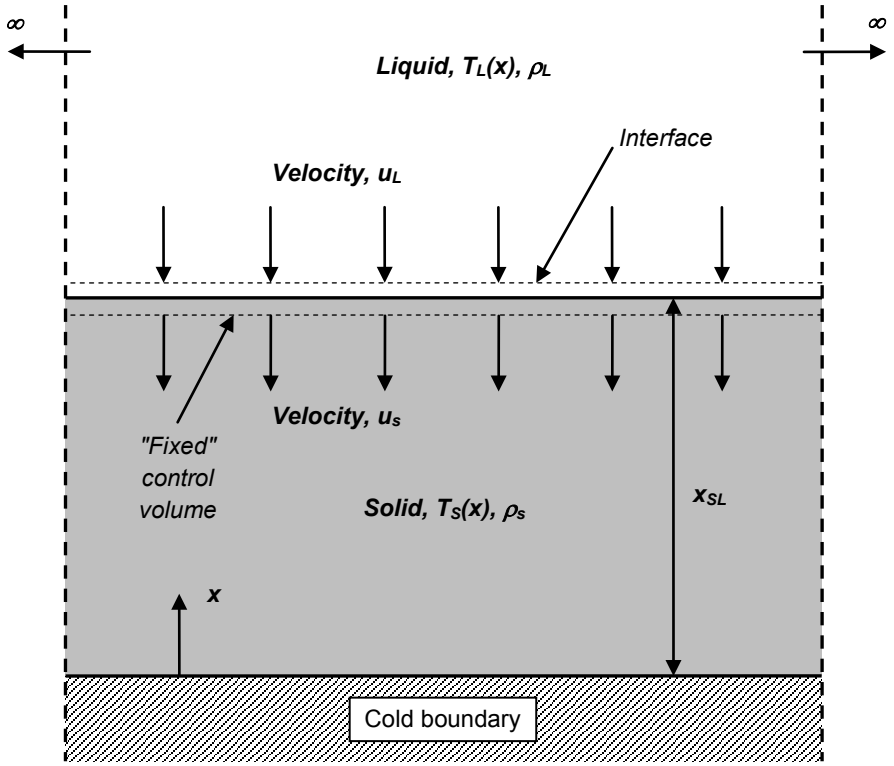

Figure 3.5. Solidification from a plane cold surface-Adapted from Poulikakos (1994)

It is assumed that freezing takes place in the liquid because of the presence of cold boundary. The study of a melting process is analogous. As the freezing progresses, the interface moves upward (in the positive direction) n the stationary medium. It is easier to model the heat transfer in the foregoing freezing process if, instead, it is assumed that the interface and the control volume surrounding it are stationary and that the medium moves downward through the interface. To this end, liquid of density ρ_L and velocity u_L enters the upper side of the control volume and solid of density ρ_S and velocity u_S exists the lower side of the control volume (in this case assuming $\rho_S > \rho_L$). Mass conservation:

$$\rho_L u_L A_V = \rho_S u_S A_V \tag{3.1}$$

where A_V is the large area of each side of the control volume.

An energy balance on the control volume yields:

$$Q_{in,cond} + Q_{in\,conv} - Q_{out,cond} - Q_{out\,conv} = 0 \tag{3.2}$$

where $Q_{in,cond}$ is the heat transferred into the control volume by conduction, $Q_{in,conv}$ is the energy transferred into the control volume by convection (since the medium is moving through the control volume), and $Q_{in,cond}$ and $Q_{in,conv}$ are the analogous quantities exiting the control volume. Fourier's law accounting for the fact that heat diffuses in the negative *x*-direction states that:

$$Q_{in,cond} = k_L A_V \left(\frac{\partial T_L}{\partial x}\right)_{x=x_{SL}} \tag{3.3}$$

$$Q_{out,cond} = k_S A_V \left(\frac{\partial T_S}{\partial x}\right)_{x=x_{SL}} \tag{3.4}$$

In addition, the energy convected In and out of the control volume is:

$$Q_{in,conv} = \rho_L u_L A_V h_L \tag{3.5}$$

$$Q_{out,conv} = \rho_S u_S A_V h_S \tag{3.6}$$

where h_L and h_S are the specific enthalpies at the liquid and solid sides of the control volume. Combining equations (3.2) to (3.6) yields:

$$k_L \left(\frac{\partial T_L}{\partial x}\right)_{x=x_{SL}} - k_S \left(\frac{\partial T_S}{\partial x}\right)_{x=x_{SL}} + \rho_L u_L h_L - \rho_S u_S h_S = 0 \tag{3.7}$$

Reconizing that the latent heat of fusion (h_{SL}) is given by $h_{SL} = h_L - h_S$ and making use of the equation (3.1), equation (3.7) yields:

$$k_L \left(\frac{\partial T_L}{\partial x}\right)_{x=x_{SL}} - k_S \left(\frac{\partial T_S}{\partial x}\right)_{x=x_{SL}} + \rho_S u_S h_{SL} = 0 \tag{3.8}$$

or

$$k_L \left(\frac{\partial T_L}{\partial x}\right)_{x=x_{SL}} - k_S \left(\frac{\partial T_S}{\partial x}\right)_{x=x_{SL}} + \rho_S h_{SL} \frac{dx_{SL}}{dt} = 0 \tag{3.9}$$

Equation (3.9) is called the Stefan condition (Hu and Argyropoulos, 1996). It is a direct result of an energy balance at the solidification front and provides a needed matching condition for the solution of the temperature field in the system. It is worth noting that this formulation holds for the case of radial conduction in cylindrical spherical coordinates if the Cartesian coordinate, *x*, is simply replaced by the radial coordinate, *r*, of a cylindrical or spherical system of coordinates. Examples of the solution of equation (3.9), in one-dimensional transient phase change problems for Cartesian, cylindrical and spherical coordinates are presented by Hu and Argyropoulos (1996) and Poulikakos (1994).

3.2.2 Variable-grid methods

Most widespread variable-grid methods use dynamical grids, where some nodes move with the phase change boundary and others are dynamically reconstructed at every time step. Therefore, the use of non-structured grid is mandatory. Transport equations are solved for each phase separately. This is the most direct approximation to the underlying physics, having the inherent shortcoming of a large computational expense related to grid calculations, which adds up to (and usually is larger than) the approximation and resolution of transport equations themselves. The fixed grid methods can be subdivided into the following subgroups:

3.2.2.1 Unstructured deforming grids

In this method the initial grid (non-transformed) is deformed in a new unstructured one. The number of spatial intervals is kept constant but their shape is adjusted in such a manner that the moving boundary lies on a particular grid point. The position of the moving boundary is updated at each step by the Stefan condition on the moving boundary (Hu and Argyropoulos, 1996).

Calculations at every time-step are performed as follows: first, a new phase change interface locations is evaluated from the Stefan conditions (quasi-stationary approach); secondly, a new grid is generated; and thirdly, the values of variables are interpolated on the new grid. An example of results from an implementation of this method in a typical problem of phase change is shown in Figure 3.6.

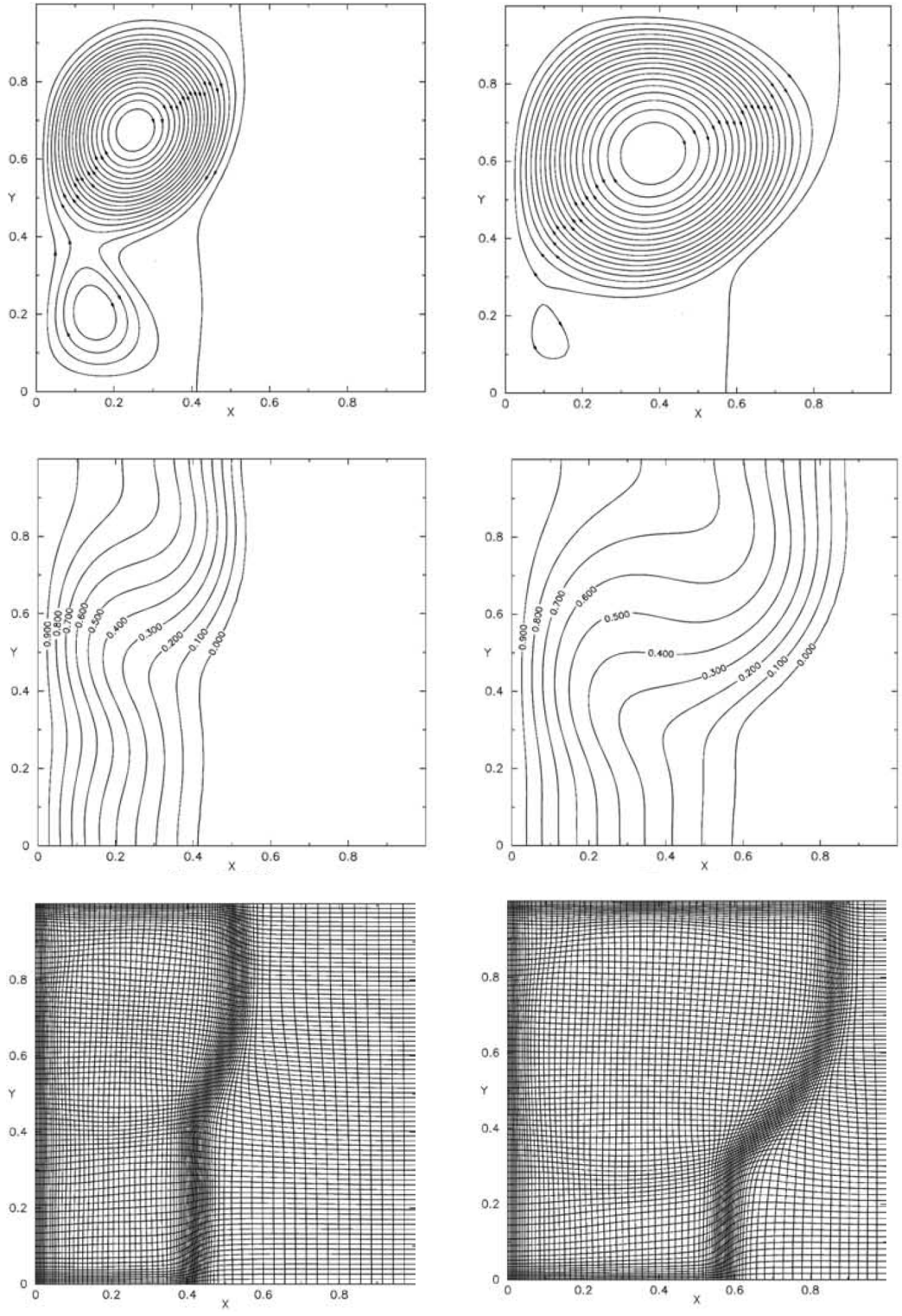

t_1 t_2

Figure 3.6. Application of the unstructured deforming grid method-Adapted from Mencinger (2004): streamlines (up); dimensionless temperature (center); deforming grid (down)

Voller (1997) and Mencinger (2004) present details of the mathematical treatment for this method.

3.2.2.2 Domain transforming techniques

This subgroup refers to the methods which are based on a transformation of the considered irregular physical domain into a rectangular one introducing new independent variables. The essential feature of this method is the fixing, in space and time, of the liquid-solid interface via a suitable choice of new space coordinates.

The movement of the solid-liquid interface and of the mesh points in the original region appears only as changes in the *x* and *y*, at the corresponding fixed points at each time step. The nature of the relationship between the fixed and physical grids is illustrated in Figure 3.7.

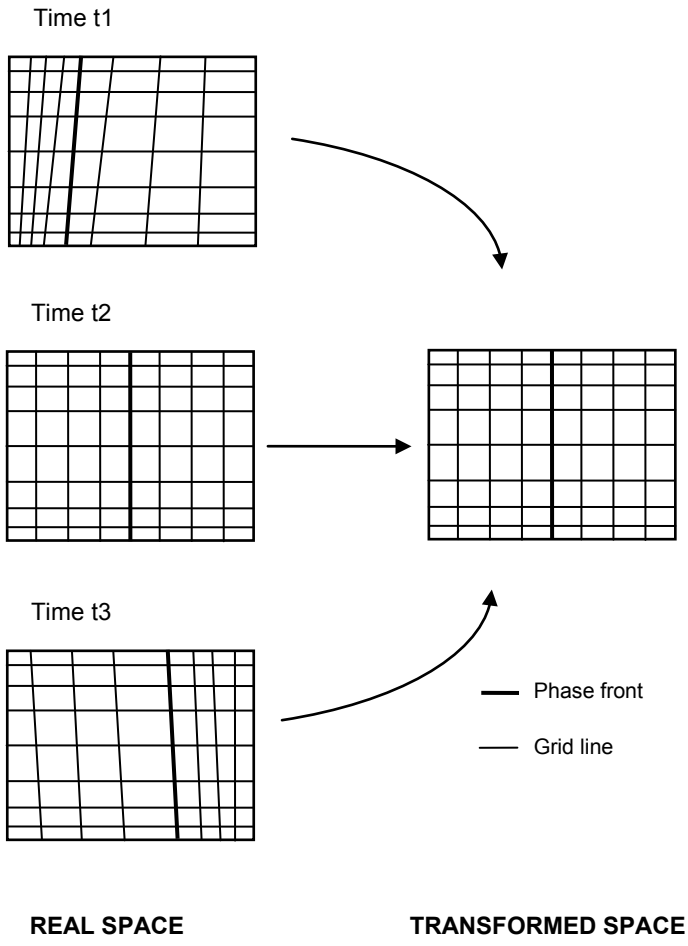

Figure 3.7. Relationship between the physical and transformed grids-Adapted from Lacroix and Voller (1990)

The major advantage of this method is that the governing flow and energy equations are solved on a fixed rectangular and uniformly spaced computational grid, with no loss of accuracy in discretization near curved boundaries. The simplicity in the numerical grid, however, comes at the expense of more complex governing equations. The method uses the coordinate transformations to map the irregular physical domain to rectangular computational space. It calculates the new interface position and the corresponding coordinate transformation after achieving stationary state. However, this quasi-stationary assumption is limited to cases with relatively slow interface movement. Also, a stationary state may not exist even with fixed interface position (Mencinger, 2004).

The key step in using this approach is the grid generation, that is, the relationship between the fixed and physical grids at any point in time. Although the same differential equations can be obtained in previous and current subgroup, the discretizations of these are different (Samarskii et al., 1993). The mathematical model for this method is explained in detail by Samarskii et al. (1993) and Lacroix and Voller (1990).

3.2.2.3 Local adaptation methods

Finally, the last subgroup encompasses the local adaptation methods. Here, the phase change interface is determined explicitly and governing equations are accurately approximated near the interface points of a fixed grid. The essence of this approach is that smooth phase change interface is approximated by a polygonal line through the grid points (Samarskii et al., 1993).

In this method the grid adapts to the solid–liquid interface, which is calculated from the heat flux balance and the grid quality is controlled with a local grid refinement method. This method becomes troublesome when the topology of the interface changes (merging or breaking), and the implementation in 3D problems is rather complicated. Also, the interface-tracking is not suitable for the cases where a phase change region appears (phase change in alloys) instead of a sharp interface characteristic of phase change of a pure metal (Mencinger, 2004).

3.2.2.4 Final comment about dynamical grid methods

In phase change problems, since the phase front moves, the grid needs to be regenerated at every time step. There are a number of options for generating the grid, but this is a procedure that could prove to be expensive in computational terms. Particular emphasis must be placed on the fact that, in the general case, construction of the grid is a very important and complicated problem by itself. In fact, grid generation can require more computational resources than the solution of the transport equations themselves.

3.2.3 Fixed-grid methods

In fixed-grid methods, a single equation is solved for the whole domain, made up of solid, mushy (for alloys) and liquid regions, instead of separated equations for each phase. The boundary is tracked implicitly over the entire region of a fixed domain. The most widely fixed grid methods used are the apparent capacity method, the source based method and the enthalpy method. Voller et al. (1990) review merits and demerits of these schemes, but a summary of each is presented in the next sections.

3.2.3.1 Apparent heat capacity methods

In this method, the latent heat is accounted for by increasing the heat capacity of the material in the phase change temperature range. The major advantage of the method is that the final energy equation is similar in form to the standard heat conduction equation; therefore it can be easily discretized and numerically solved with well-developed algorithms. Hu and Argyropoulos (1996) and Voller and co-workers (Voller, 1997, Swaminathan and Voller, 1992, Swaminathan and Voller, 1993, Voller et al., 1990) present the procedure to calculate and discretize the apparent heat capacity method.

The method has been extended to finite element formulation in a generally applicable approach to one and two dimensional problems, with both moving boundaries and temperature-dependent physical properties. Although the apparent heat capacity method is conceptually simple, the method does not perform well as compared with other methods (Hu and Argyropoulos, 1996, Voller et al., 1990). The reason for such a

drawback is that if, for a melting case, the temperature of a control volume rises from below the solidus to above the liquidus temperature in one time step, the absorption of the latent heat for that control volume is not accounted for. As a result, very small time steps have to be used in order to overcome this shortcoming.

3.2.3.2 Source-based method

This method allows any additional heat from either, a heat source (latent heat during solidification) or a heat sink (latent heat during melting), to be introduced into the general form of the energy equation as an extra term, that is, a source term. Voller and Swaminathan (1991) present the formulation of a general source-based method.

The source-based method has become more popular over the years. The reason for this is that the form of the final energy equation is compatible with basic numerical solution approaches; in particular those based on finite difference control volumes. The overall accuracy of this method is fairly good, especially for non-isothermal phase change problems (phase change in mixtures) (Hu and Argyropoulos, 1996, Voller et al., 1990).

A complete description of the discretization of this method is given by Hu and Argyropoulos (1996) and Voller and co-workers (Swaminathan and Voller, 1993, Voller, 1997, Voller and Swaminathan, 1991, Voller et al., 1990).

3.2.3.3 Enthalpy method

In this method, the evolution of latent heat and temperature are accounted for by phase enthalpy. This is accomplished by a source term introduced in the energy equation that accounts the variation in latent heat and sensible heat for the phase change process. Another source term is introduced in the momentum equation in order compute the velocity in the liquid and mushy zones but imposing at the same time, a zero velocity in the solid zone. It is assumed that the enthalpy is only a function of the temperature.

The enthalpy formulation may cause convergence difficulties in the numerical discretization when variable properties are used. Furthermore, oscillation of the solution may appear for cases with large ratio of latent heat to sensible heat. However, the enthalpy method gives accurate solutions with a reduced computational cost, especially

for phase change problems of alloys in which a phase change temperature range exists (Hu and Argyropoulos, 1996).

The enthalpy method is in fact the most widely used in phase change problems and has been tested in several applications. Also, this method is actually implemented in commercials codes, such as FLUENT (ANSYS, 2012) or STAR-CCM+ (CD-ADAPCO, 2004).

First formulations were developed by Voller et al. (1987), Voller and Prakash (1987) and Voller et al. (1988); these contributions constitute the most comprehensive and recommendable account of the subject. The evolution of the methodology and the procedure for the numerical discretization has been covered by Voller and coworkers (Lacroix and Voller, 1990, Swaminathan and Voller, 1992, Swaminathan and Voller, 1993, Swaminathan and Voller, 1997, Voller, 1997, Voller et al., 1987, Voller and Prakash, 1987, Voller and Swaminathan, 1991, Voller et al., 1990).

In this work, the enthalpy method is used; for a full appreciation, their equations are summarized in the following section.

3.3 Governing equations of the enthalpy method

The governing equations used in the numerical simulations are presented in this section. All terms are based in the enthalpy formulation, which is used to solve the phase change problem in the aluminum load. The adaptation of the governing equations in gas and solid domains are also presented.

For the convective motion of the molten load and gas into the furnaces, the Navier Stokes equations corresponding to a fluid of variable density can be written as:

$$\frac{\partial}{\partial t}\rho + \nabla \cdot (\rho \vec{u}) = 0 \tag{3.10}$$

$$\frac{\partial}{\partial t}\rho \vec{\boldsymbol{u}} + \nabla \cdot (\rho \vec{\boldsymbol{u}}\vec{\boldsymbol{u}}) = -\nabla P + \nabla \cdot (\bar{\bar{\tau}}) + \rho \vec{\boldsymbol{g}} + S_u \tag{3.11}$$

In Eq. (3.11), the source term (S_u) modifies the momentum balance depending on the phase. In the gas zone, this term is set to zero. In the phase change domain (aluminum load in this case), the source term varies from a large value imposing complete rest of a solid material, down to a limiting value of zero when the material becomes completely liquid. The "mushy" zone in between can have a physical existence for alloys or be made conveniently thin for pure metals. This behavior can be accounted for by defining:

$$S_u = -A^* \vec{\boldsymbol{u}} \tag{3.12}$$

Where *A** increases from zero to a large value as the liquid fraction (γ) decreases from its liquid value of 1 to its solid value of 0. A well-known format, derived from the Darcy law, which has been proposed as a general model for flow in metallurgical mushy regions (Lacroix and Voller, 1990, Swaminathan and Voller, 1993, Voller et al., 1988, Voller, 1997, Voller et al., 1987, Voller and Prakash, 1987), is the Carman-Kozeny equation:

$$A^* = \frac{C^*(1-\gamma)^2}{\gamma^3 + q} \tag{3.13}$$

Where *C** is the mushy zone constant, that depends on its morphology; values between $1x10^4$ and $1x10^7$ are recommended for most computations. γ is the local liquid fraction. Voller and Prakash (1987) introduce the constant *q* as a small number (0.001) to prevent division by zero.

In the gas domains, the liquid fraction value is 1; therefore the values for *A** and S_u in these cases become zero.

The energy equation is rewritten in terms of the enthalpy *h* as (Voller et al., 1988, Voller et al., 1987):

$$\frac{\partial(\rho h)}{\partial t} + \nabla \cdot (\rho \vec{\boldsymbol{u}} h) = \nabla \cdot \left(\frac{k}{c} \nabla h\right) + S_h \tag{3.14}$$

In this case, the relation thermal conductivity/specific heat *k/c* is approximated as a constant. The source term S_h is zero for the gas inside furnace and solid domains. In solid

domain, the enthalpy method is implemented via the energy conservation equation, written as Eq. (3.14) with a zero velocity, i.e., as a purely conductive problem.

In aluminum load domain, evolution of the latent heat is accounted for by defining the source term S_h as:

$$S_h = \frac{\partial(\rho \Delta H)}{\partial t} + \nabla \cdot (\rho \vec{\boldsymbol{u}} \Delta H) \tag{3.15}$$

where:

$$H = h + \Delta H = \int c dT + \Delta H \tag{3.16}$$

and $\Delta H = \gamma\, h_{SL}$, with h_{SL} denoting the latent heat of fusion and the liquid fraction being defined as:

$$\gamma = \begin{cases} 0, & T < T_S \quad solid\ phase \\ \dfrac{T - T_S}{T_L - T_S}, & T_S < T < T_L \quad solid/liquid\ phase \\ 1, & T > T_L \quad liquid\ phase \end{cases} \tag{3.17}$$

where T_S and T_L are the solidus and liquidus temperatures, respectively.

Eq. (3.17) is the solution of the linear approach for the phase change in binary alloys presented in section 3.1.2. As was discussed before, this approach is accurate for most alloys; for other complex materials, this is taken as the best approach included in commercial codes.

In the cases of pure substances and alloys with eutectic compositions (isothermal phase change occurring at temperature T_{melt} and T_E, respectively), when phase change occurs in the neighbourhood of the phase change temperature, the abrupt changes may lead to numerical difficulties. To solve this, a small artificial temperature region is introduced in order to approximate the discontinuity at the linear piecewise continuous curve (Voller et al., 1990). The limits in Eq. (3.17) become: $T_S = T_{melt} - \varepsilon_T$ and $T_L = T_{melt} + \varepsilon_T$. Where ε_T is a small temperature value (0.05 ºC approx).

In general, the phase change problems involve materials that have variable thermophysical properties. Some care needs to be taken in this kind of problems, in particular, where the thermal properties are discontinuous across the phase change. Properties can be calculated in terms of nodal averaged values or mixture properties (Swaminathan and Voller, 1992, Swaminathan and Voller, 1997, Voller, 1997, Voller and Swaminathan, 1991, Voller et al., 1990):

$$w = (1 - \gamma)w_S + \gamma w_L \tag{3.18}$$

where w is any thermal property of the mixture as the specific heat or mixture conductivity.

3.4 Surface-to-Surface radiation model (S2S): Numerical simulation by computing view factors

Aluminum in solid and liquid phases is practically opaque to thermal radiation in the spectral range corresponding to T < 800 ºC, but air filling up the furnaces is transparent. Therefore, an accurate model of heat losses must incorporate the transfer of energy by thermal radiation between the internal surfaces of the furnaces, including the load exposed to gas in cavities. This effect is a consideration even more important for the processing of other metals, as the melting of steel, whose temperature exceeds the 1200 ºC instead the 800 ºC reached in aluminum production. However, such a mechanism is expected to contribute in an amount comparable to heat convection in the gas. This is an added complexity to the already complex model of heating and phase change in melting and holding furnaces.

The surfaces of the furnaces analyzed are opaque (not transparent). When radiation falls on a real opaque surface, some will be absorbed, and the remainder will be reflected. The fraction of the incident radiation that is absorbed or reflected depends on the material and surface condition, the wavelength of the incident radiation, and the angle of incidence. There is also a small dependence on the surface temperature. However, for engineering calculation, it is adequate to assume that appropriate average values can be

used. If the absorptance (absorptivity) of a surface *k* (α_k) is defined as the fraction of all incident radiation absorbed, and the reflectance (reflectivity) of a surface *k* (ρ_k) is defined as the fraction of all incident radiation reflected, then for an opaque surface:

$$\alpha_k + \rho_k = 1 \tag{3.19}$$

The radiant energy emitted by a surface *k* at all wavelengths is its total emissive power (E_K). It has a fourth-power temperature dependence given by the Stefan-Boltzmann law, for a black surface:

$$E_{k,b} = \sigma T_k^4 \tag{3.20}$$

where σ is the Stefan-Boltzmann's constant (5.672 x 10^{-8} ($W/m^2.K^4$)).

For a real surface:

$$E_k = \varepsilon_k E_{k,b} \tag{3.21}$$

where ε_k is the emissivity of the real surface *k*, which is a surface radiative property defined as the ratio of the radiation emitted by the surface to the radiation emitted by a blackbody at the same temperature.

Reasonable assumptions can be made for most engineering applications (as in the present case) in order to simplified greatly the calculation of the radiation. Firstly, ε_k and α_k vary rather weakly with temperature. Secondly, diffusive reflection occurs, i.e. regardless of the direction of the incident radiation, the intensity of the reflected radiation is independent of the reflection angle. Finally, the surface is gray, i.e. emissivity and absorptivity are independent of the wavelength. Under these conditions:

$$\alpha_k = \varepsilon_k \tag{3.22}$$

A surface for which emissivity and absorptivity are independent of the reflection angle and wavelength is termed a diffusive, gray surface. It is possible to model the real opaque surfaces of the furnaces in this form, the radiation properties are characterized by a single average radiative property of the surface.

Thermal radiation is calculated by the so-called "surface-to-surface" (S2S) radiation model of FLUENT (ANSYS, 2012). This is a built-in implementation of the net radiation method (Mills, 1992) coupled to the diffusive term of surface energy balances. It relies on the numerical calculation of geometric view factors between pairs of surface elements, only dependent on discretization, and assumes diffuse-gray radiation, which is reasonable for the problem.

Equations involved in the S2S model are presented in the theory guide of FLUENT (ANSYS, 2012). The basic theory is presented as follows:

The net heat radiation of a surface *k* is computed from:

$$q_{rad,k} = A_k \sum_{j=1}^{N} F_{kj}\left(J_k - J_j\right) \tag{3.23}$$

and

$$q_{rad,k} = \frac{\varepsilon_k A_k}{1-\varepsilon_k}\left(\sigma T_k^4 - J_k\right) \tag{3.24}$$

where ε_k is the emissivity of surface *k*, σ the Stefan-Boltzmann's constant, A_k is the area of surface *k*, F_{kj} is the view factor between surface *k* and surface *j* and *J* is the surface radiosity.

In equations (3.23) and (3.24), the values of $q_{rad,k}$, T_k and J_k are unknown. The net heat radiation is incorporated to the energy conservation in the surface, and it is taken into account for the balance with terms of conduction or convection for solid or fluid adjacent domains, respectively. These latest terms are solved numerically by the CFD code. Equations (3.23), (3.24) and energy conservation are solved simultaneously in an iterative procedure in order to obtain $q_{rad,k}$, T_k and J_k. The method is also holds for transient state, since the mass of the surface is by definition very small, the radiation heat transfer is too fast and there is not accumulation.

The view factor F_{kj} between two finite surfaces *k* and *j* is given by:

$$F_{kj} = \frac{1}{A_k}\int_{A_k}\int_{A_j}\frac{cos\theta_k cos\theta_j}{\pi r^2}\delta_{kj}dA_k dA_j \tag{3.25}$$

where δ_{kj} is determined by the visibility of dA_j to dA_k. $\delta_{kj} = 1$ if dA_j is visible to dA_k and $\delta_{kj} = 0$ otherwise.

Rays are traced through the centers of every face to determine which surfaces are visible through that face. At each radiating face, rays are fired at discrete values of the polar and azimuthal angles. To cover the radiating hemisphere, polar angle is varied from to *0* to $\pi/2$ and azimuthal angle from *0* to 2π. Each ray is then traced to determine the control volumes it intercepts as well as its length within each control volume. This information is then stored in the radiation file, which must be read in before the fluid flow calculations begin.

The reciprocity relationship is also used:

$$A_j F_{jk} = A_k F_{kj} \quad \text{for } j = 1,2,3,\dots,N \tag{3.26}$$

The first step in the implementation of the S2S radiation model is to compute the view factors for the specific problem and grid. This process consumes high computational resources, but it is performed only once by each simulated domain.

4. Numerical simulation of an aluminum melting furnace

In this chapter, simulations of a new aluminum melting furnace heated by a plasma torch are presented; these simulations reproduce an experimental test carried out in a real prototype. The aim is to calculate melting time, heat losses and temperature distributions in the aluminum load and refractory parts. Models used are 2D axisymmetric and take into account heat conduction in solid parts, convection in air and molten aluminum, interactions between gas-liquid-solid zones and radiation heat transfer. Several calculation strategies are tested concerning their computational economy and their accuracy in computing different key parameters. Results show that interactions gas-liquid-solid have an important effect. Firstly, a proper account of heat transfer and losses requires solving the conjugated problem comprising refractory walls and heated load. Secondly, thermal interaction with air cavities seems to determine the convective movement of the molten load and therefore inner-load temperature patterns and their time evolution.

4.1 State of the art in related numerical simulations

4.1.1 Melting furnaces

In addition to phase change, several other complex physical phenomena occur in industrial furnaces that are difficult to model and couple within an unified simulation. Conjugate heat diffusion through solid and fluid volumes, movement of the molten load

and radiation heat transfer are some of them. Accordingly, works dealing with realistic, comprehensive simulations are rather scarce in the literature, so that a review is forcibly brief and encompasses very different applications and approximations. As direct antecedents of the work presented here, the following can be quoted:

4.1.1.1 Empirical studies of melting furnaces

Furnace manufacturers test their devices in industrial conditions. But experimental data are often not available for public domain. In this sense, only a general perspective is known about the operation of furnaces in secondary aluminum production. The U.S. Department of Energy has sponsored an investigation to improve the energy efficiency in reverberatory furnaces for aluminum melting. As a result, an experimental reverberatory furnace has been constructed (Das, 2008, Das, 2007, King et al., 2005b); some general parameters have been obtained (King et al., 2005a, Belt et al., 2006, King et al., 2005b, Li et al., 2003, Golchert et al., 2005), e.g. the influence of power input, burner loading and combustion space volume on melting efficiency; scaling laws (Penmetsa et al., 2005) and simplified models based in thermodynamic procedures to estimate the performance (Li et al., 2006, Li et al., 2005). Concerning rotary furnaces, Zhang et al. (2008) present an experimental study on steel scrap melting in a continuous process furnace. They also developed a simplified thermal model to evaluate commercial viability of industrial-scale units.

All these empirical works were developed for specific furnace types; in addition, the studies were based on combustion heating, which makes difficult the use of the results in the development of new technologies.

4.1.1.2 Aluminum melting furnaces

Wang et al. (2013) present a numerical simulation to estimate the melting process of a regenerative aluminum melting furnace; the model consists in a combination of a self-developed melting model and a CFD commercial code. Different burner factors such as the location, orientation and inlet conditions are investigated in order to estimate their effects on the melting process. Inside the furnace, the CFD solution of the combustion is coupled with the melting sub-model. The solid–liquid region (load) is treated as a

conducting solid with constant thermal properties. In this simulation, the heat losses by the walls are neglected. Wang et al. (2012) present a study of the optimization of parameters for a regenerative aluminum melting furnace using the Taguchi approach. The effects of the burner location and operational conditions are analyzed through numerical CFD experiments in an orthogonal array. These simulations are the base for the work of Wang et al. (2013) presented above. Therefore, the same simplifications are taken. In this case, the main objectives are to reduce energy consumption and pollutant emission, instead of improve the melting performance.

A similar approach is presented by Zhou et al. (2006), who simulate the melting of aluminum scrap in a rotary furnace under a salt layer. In this work, the combustion is also simulated with a commercial CFD code and the solution is coupled to a melting model, the treatment for the load is also as a conductive solid with constant thermal properties, averaged in this case with the total mass of scrap and salt flux. The main target of this study is to predict the melting rate and energy distribution and their relation with types and properties of the scrap. In this approach the conjugated problem is taken into account and the oxidation of the load is estimated with a self-developed sub-model. The rotation of the furnace is not included in the model. The main drawback is that the overall simulation must be adjusted to empirical data, that are difficult to obtain a priori. Wu and Lacroix (1995) applied a two-dimensional time-dependent heat transfer model for the melting of scrap metal in a circular furnace without considering radiation heat transfer. The phase change problem is treated with the enthalpy method in an assumed porosity domain. The model is limited to the prediction of the temperature distribution in the axial direction in a non conjugated domain.

4.1.1.3 Electric arc furnaces

The electric arc furnaces (EAF) are typically used in secondary production of steel, but they share several features with the melting furnace analyzed in this thesis. The design of these devices, as in other furnaces types, is based in semi-empirical models as those presented by Logar and Škrjanc (2012a), that develop an industrial EAF simulator, based on semi-empirical correlations for the electrical and hydraulic model (Logar et al., 2011), heat and mass transfer (Logar et al., 2012a), thermo-chemistry (Logar et al., 2012b) and

radiative heat transfer (Logar and Škrjanc, 2012b). This kind of models can be used to estimate the general parameters of the furnace designed, but don't offer details of the thermal behavior for a specific device.

Arzpeyma et al. (2013) simulate an eccentric bottom tapping EAF to investigate the influence of electromagnetic stirring on melting of a single piece of scrap. Only the load domain is considered in this study; other components like the electrical electrodes, furnace walls or air in cavity are considered indirectly through different boundary conditions. The piece of scrap is a little cube located on the bottom of the furnace and the remaining charge is considered in liquid state. The phase change process is modeled by the enthalpy method. The heat transfer and fluid flow in the melt for both conditions with and without electromagnetic stirring are studied. The results show that electromagnetic stirring leads to a considerable reduced melting time; this conclusion is justified by the increase of the convection inside the molten load, which is predicted for the same problem by ABB Metallurgy (Widlund et al., 2011) in an EAF without melting. González et al. (2010b) develop a Lagrangian model of melting particles to describe the melting kinetics of metallic particles in an industrial EAF. This model must be coupled to a CFD solution that predicts the fluid flow previously (González et al., 2010a). In these works, the Boussinesq approximation is invoked to model the convection effects, and again, only the load domain is considered.

4.1.1.4 Induction furnaces

Simulations of induction furnaces have increased in the last years with the development of multi-physics codes. Even though this kind of simulations requires a coupling between the flow model and Maxwell equations, the induction furnaces present some advantages in computational terms compared with other used technologies: e.g. low temperatures in the whole furnace, the movement of the molten load is mainly driven by the Lorentz force and the geometries can be simplified to 2D axisymmetrical. Nevertheless, so far only a few works include an integration of the magnetohydrodynamic problem with the phase change energy balance and fluid flow. Bermudez and co-workers (Bermúdez et al., 2007b, Bermúdez et al., 2010, Bermúdez et al., 2009, Bermúdez et al., 2007a, Bermúdez et al., 2011) have developed one of the most comprehensive. The enthalpy method is

used to consider the phase change of the load. The solutions have been implemented in 2D axisymmetrical domains with the finite element method (FEM) (Bermúdez et al., 2007b, Bermúdez et al., 2010) and with a combination between boundary element method (BEM) and FEM method (Bermúdez et al., 2009, Bermúdez et al., 2007a, Bermúdez et al., 2011). The latest methodology avoids the numerical solution of the air around the coils.

4.1.1.5 Electro slag remelting process

Other melting process whose modeling involves the coupling of the Maxwell and flow equations is the electro-slag remelting (ESR) process. This is used in aluminum secondary production to produce large ingots of higher quality than the original material, by controlled solidification and chemical refinement. Usually, an ESR furnace consists of one electrode submerged in a poorly conducting mix, relatively conductive slag, and a highly conductive crucible. The passage of current through the electrode supplies electrical energy to the slag for metallurgical processes. At steady state the heat transfer mechanisms are a combination of thermal conduction together with forced and free convection. The body forces causing the motion are a combination of electromagnetic (dominant in this case) and thermal buoyancy (Ahn et al., 2009, Prasad and Rao, 2000).

One of the main complications in the simulation of these processes, is that material properties are a strong function of temperature, which greatly influences the electrical, magnetic, temperature, and velocity fields. Furthermore, a major aim of the process is to separate the contaminants from the metal of high quality by density difference. Therefore, in many cases an additional multiphase model must be coupled. Simulations in this subject are performed with simplified geometries in 2D axisymmetric, without considering any external element to the load, like walls, electrodes or air in the cavity of the furnace (Kelkar et al., 2005, Patel and Kelkar, 2009, Rückert and Pfeifer, 2009, Rückert and Pfeifer, 2007, Weber et al., 2009, Chang and Li, 2008, Kharicha et al., 2005). Currently, three dimensional models are even more simplified cases; for instance, Xihai et al. (2011) and Li et al. (2012) implement 3D models of ESR processes for the heating of the load, but without considering the melting or the movement of the fused phase. Recently Kharicha et al. (2011) simulated the 3D movement of a molten load in an ESR

process and found three-dimensional flow effects for large geometries. Unfortunately the current computational resources force the use of 2D approaches in melting analysis.

4.1.1.6 Glass melting furnaces

In the glass production, works of numerical simulations can be found for melting furnaces. This is a most complicated problem in terms of radiation calculation; because it is necessary take into account the volumetric radiation in a participating media, since in general, the surfaces are not opaque and the reflection is not diffusive. Choudhary et al. (2010) present a review of the principles and practices involved in mathematical modeling of batch melting, electric heating of glass melt, convection due to bubbling, combustion, turbulence, radiation, and viscoelasticity for the industrial-scale glass melting furnaces. Abbassi and Khoshmanesh (2008) undertake a three dimensional steady state study of a gas-fired, regenerative, side-port glass melting furnace. The melting process of the solid load (batch blanket), the natural convection of the resulting molten glass and the turbulence and chemical reactions of the combustion space are all simulated. The glass load and the combustion space are simulated separately. Despite the load reaches temperatures above 1073 K, this comprehensive approach doesn't consider the radiation in the molten bath and the conjugated problem, neglecting the heat losses through the walls of the furnace. Recently, Díaz et al. (2013) performed CFD calculations in steady state condition to define the effect of the burner configuration in a day tank glass furnace (tank glass melting furnace of periodic operation, is used when the daily demand may not be enough to use a continuous furnace). To represent the entire system, the combustion chamber and glass tank are modeled separately, but coupled through boundary conditions. Natural convection is represented by the Boussinesq approximation and radiation is simulated in both the combustion chamber and the glass tank whit a radiation model, but the density of the molten load inside the tank is considered constant and the melting process is not estimated. The authors also developed a simplified mathematical transient model to estimate the thermal behavior in the furnace considering radiation, combustion, convection, heat loss through walls and glass melting.

4.1.1.7 Other numerical simulations in furnaces

Most literature about numerical simulation of aluminum melting furnaces does not consider the molten aluminum in the furnace and the interaction between combustion space and aluminum bath. Below some simulations related with processes of melting furnaces are presented.

Nieckele et al. (2011) and Nieckele et al. (2004) present numerical simulations of the combustion process inside industrial aluminum melting reverberatory furnaces. They analyze the flame patterns, species concentration distribution, temperatures and velocity fields with combinations of oxygen and air, natural gas and liquid oil, and different injection options. Hongjie et al. (2012) also performed simulations of the combustion process in a prototype of reverberatory furnace for copper recovery. A series of simulations was used to optimize the combustion performance varying the burner construction and installation location. Golchert et al. (2005) used a non commercial CFD code in order to simulate the combustion, heat transfer (including thermal radiation), gaseous product flow (mainly CO_2 and H_2O), and production/transport of pollutant species/greenhouse gases in an aluminum reverberatory furnace. Using this code, the surface heat fluxes are calculated and these data can be used in a melt code. The output from the code is compared and validated against in the furnace measurements carried out by King et al. (2005a).

Cadavid et al. (2010) present a three dimensional numerical simulation of a gas-fired self-regenerative crucible furnace; different combustion models are used to assess their effects on the numerical results. Aerodynamics, temperature fields, species profiles and emissions are compared with experimental data. Mei et al. (2008) simulate the combustion space of an oil fired float glass furnace including the turbulence, radiation and the oil drop motion.

Davies et al. (2013) analyze the energy flows within a rotary aluminum recycling furnace, using the global properties of its main components, i.e. the gas, metal and refractory walls. With this simplified model, different operations such as loading, heating and stirring are estimated. The furnace is broken up into its components and each is treated

differently within the model. A one-dimensional numerical model is used for each section neglecting any losses through the sides. Radiative exchange within the furnace, melting of the charge, and forced convection in the melt due to the rotation of the furnace are also considered. Khoei et al. (2003) carried out numerical simulations of a rotary furnace to estimate the evolution and distribution of temperatures in the furnace walls under different flame positions. In order to apply the heat generated at the flame position and heat transferred between the melted material and the internal surface of the furnace, the segments of the walls (elements in the FEM model) are modeled by different flux pulses applied successively to each segment to simulate the changes in thermal loading during rotation. Guo and Irons (2008) modeled the steel scrap movement into a device to understand the phenomenon and thus avoid operational problems in melting furnaces.

Finally, several simulations have been done for the heating of solid pieces inside furnaces. Since these cases are more simplified than heating of liquid material or melting processes, the models used can be represented with 3D approaches, including interaction of the solid pieces with combustion products (DellaRocca et al., 2012, Han et al., 2009) or with turbulent flow in a conjugated problem (Hachem et al., 2013).

4.1.2 Phase change problems

Bermúdez and Otero (2004) simulate a phase change problem of aluminum for a casting process with in a 3D domain. Solidification is considered with the enthalpy formulation taking into account the convection effects. Because of symmetry, only a quarter of the region occupied by the metal is simulated. The problem is considered as not conjugated, the cooling by the contact of the slab with either the bottom block or air or water, are represented by means of boundary conditions.

Melting in metals with low fusion points in rectangular cavities have been simulated by different authors. 2D simulations in not conjugated problems, including convection and heating from the side with a fixed temperature boundary condition, are solved for gallium (Belhamadia et al., 2012) and tin (Hannoun et al., 2005). Recently, Ben-David et al. (2013) solve this same problem for melting of gallium using 2D and 3D approaches;

their results revealed a better agreement between 3D computational and experimental data.

A related class of problems that have been widely studied refer to phase change materials (PCM) at near-ambient temperatures. Simulations typically use the enthalpy formulation and logically handle buoyancy via the Boussinesq's approximation, but often consider simplistic 2D geometries, including square cavities, cylinders, pipes or spheres. Also experimental visualization techniques are used to validate the detailed numerical results, taking advantage of the transparency of the liquid phase in many cases. A few authors use distinct properties for liquid and solid phases. Others solve the conjugate problem or use the method of "Volume of Fluid" (VOF) in order to consider the volume expansion. A summary of the typical works developed in this field is presented in Table 4.1. A comprehensive review of the simulations undertaken in PCM applications are given by Dutil et al. (2011) and Al-abidi et al. (2013) present an excellent complementary review.

Table 4.1. Summary of the typical works developed in PCM simulations

Reference	PCM	Geometry	Convection	Conjugated problem	VOF	Experimental measurements
Dhaidan et al. (2013a)	n-octadecane + CuO	Cylindrical concentric/ eccentric horizontal annulus	Boussinesq			E1-E2
Dhaidan et al. (2013b)	n-octadecane + CuO	Square	Boussinesq			E2
Dhaidan et al. (2013c)	n-octadecane + CuO	Horizontal cylindrical	Boussinesq			E1-E2
Longeon et al. (2013)	RT35*	Annulus vertical cylinder	Boussinesq			E1-E2
Mahdaoui et al. (2013)	Gallium	Rectangular with hole	Boussinesq			
El Qarnia et al. (2013) and Faraji and El Qarnia (2010)	n-eicosane	Rectangular with discrete protruding	Boussinesq	Infinite viscosity in solid regions		
Sharifi et al. (2013)	Octadecane	Cylindrical	Boussinesq			E2-3D array
Arasu and Mujumdar (2012)	Paraffin wax + AL_2O_3	Square	*ρ (T,Comp.)*			
Darzi et al. (2012)	n-eicosane	Cylindrical concentric/ eccentric horizontal annulus	Power law			
Wang et al. (2010b)**	Multiple	Rectangular	Boussinesq			
Tan et al. (2009)	n-octadecane	Spherical	Boussinesq			E1 and E2
Vidalain et al. (2009)	Gallium	Rectangular	Self model simplification			
Assis et al. (2007)	RT27*	Spherical	Boussinesq	yes	yes	E1
Jones et al. (2006)	n-eicosane	Cylindrical	Boussinesq	yes	yes	E1 and E2
Scanlon and Stickland (2004)	Lauric acid/ Water	Rectangular with hole/ Rectangular	Different liquid and solid prop.			E1 and E2
Khodadadi and Zhang (2001)	Multiple	Spherical	Boussinesq			E1

*Commercial PCM; **Self melting model; VOF: Volume of Fluid method; E1: Visualization techniques in transparent liquid phase; E2: Temperatures measurement with thermocouples; *ρ (T,Comp.)*: Density function of temperature and composition; Different liquid and solid prop.: Different liquid and solid properties and both function of temperature

4.1.3 Plasma torch

In the analyzed melting furnace, the heating is performed by a transferred thermal plasma torch. This new heating system in the aluminum melting furnace adds a strong complication to the numerical simulations. The most ambitious aim of a thermal plasma model is to provide a consistent description of the plasma from only macroscopic

parameters such as the geometry, the current intensity, the nature of the gas, material properties, the mass flow rate and some boundary conditions. Actually, the present development of thermal plasma modeling does not allow a comprehensive description, because the lack of precise knowledge of some phenomena (electrode phenomena, radiation, turbulence, wall ablation) imposes simplifications on the models and thus on experimental adjustment or validation (Gleizes et al., 2005).

The modeling of DC arc plasma torches is extremely challenging due to several features in the plasma flow: e.g. it is highly nonlinear, presents strong property gradients, it is characterized by a wide range of time and length scales, and often includes chemical and thermodynamic non-equilibrium effects. High collision frequencies lead to a state close to local thermodynamic equilibrium (LTE) in which the kinetic energy of the constitutive species can be characterized by a single temperature. The LTE approximation is often violated near the plasma boundaries, either as the plasma interacts with solid walls, the working material, or with the cold working gas or atmosphere.

The range of temperatures that have to be considered in studies of thermal plasmas is typically from room temperature to the central regions of the plasma (T > 1000 K). Within this range, many different species are generated. For example, in a nitrogen plasma, N_2, N_2^+, N, N^+, N^{2+}, N^{3+} and electrons will be present in significant concentrations. In plasmas in gas mixtures, there are typically more species that also have to be considered. For example, in an argon–nitrogen plasma, eleven species, Ar, Ar^+, Ar^{2+}, Ar^{3+}, N_2, N_2^+, N, N^+, N^{2+}, N^{3+} and the electron, would usually be present in significant concentrations (Murphy, 2001). The determination of thermodynamic and transport properties requires first the calculation of plasma composition that must be obtained from a chemical model. Thermodynamic properties depend highly on the local temperature and composition, and are calculated from the particle number densities of the various species forming the plasma and previous knowledge of the internal partition functions (Trelles et al., 2009, Gleizes et al., 2005).

The most frequently used thermal plasma models rely on the LTE approximation, and model the plasma flow as the flow of a property-varying electromagnetic reactive fluid

in chemical equilibrium. As the plasma flow behavior can be assimilated to a fluid, the equations used to describe the hydrodynamic movements are the Navier–Stokes equations. The mass, momentum and energy equations are the same as for a classic hydrodynamic problem except for some additional terms in the momentum and energy equations. These terms come from the coupling of the Maxwell's equations, a term that represents the radiation heat loss in the arc core to the surroundings and the diffusion fluxes (Trelles et al., 2009, Gleizes et al., 2005, Murphy, 2001). The latest terms include the diffusion rates between the large numbers of species generated, even for a unique parent gas, and the thermal diffusion due to the high temperature gradients. The theory of calculation of these diffusion coefficients are detailed by Murphy (2001).

Chau and Hsu (2011), Chau et al. (2011), Colombo et al. (2008), Iwao et al. (2008), Chau et al. (2007) and Hur et al. (2001) simulate thermal plasma torches with 2D axisymmetrical models. They consider the radiation through the net emission coefficient approach (NEC) and neglect the diffusion fluxes. The NEC approximation is the most common approximation used in thermal plasma modeling to describe the radiation transfer. This technique is a direct but rough calculation based in the calculation of an effective net emission coefficient (net means the difference between emission and absorption), which for a given plasma forming gas can be expressed as function of temperature and an effective absorption radius. The latter represents the radius of a isothermal sphere in which the emitted radiation can be re-absorbed; outside of this sphere, the emitted radiation leaves without further interaction with the plasma. The net emission approach is particularly appealing for thermal plasma flow simulation because the effective emission coefficient can be treated as any other thermodynamic or transport property of the plasma (Trelles et al., 2009). Currently, net emission coefficients are available for the different pure gases, e.g. N_2 (Ernst et al., 1973, Gleizes et al., 1991), SF_6 (Gleizes et al., 1991), air (Naghizadeh-Kashani et al., 2002) and Ar (Iwao et al., 2008); and mixtures, e.g. SF_6-N_2 (Gleizes et al., 1991), Ar-Cu, N_2-Cu, SF_6-Cu and Ar-Fe (Gleizes et al., 1993). The radiation losses in thermal plasma are generally a minor loss of the total input electrical energy. Furthermore, the form in which radiation directly interacts with the plasma flow suggests that detailed description of radiation transfer

may not be needed; therefore direct approximations of the total radiation transfer as the NEC approach is justified. (Tanaka and Lowke, 2007, Trelles et al., 2009, Gleizes et al., 2005).

Other authors also use the losses by radiation with the NEC approximation but include the calculation the diffusion fluxes, cases in 2D domains have been presented by Tanaka and Lowke (2007) and Lago et al. (2004), and simulations in 3D domains have been presented by Gonzalez et al. (2002) and Gonzalez et al. (2005).

The exact treatment for the diffusion term is obtained with the solution of each species in the plasma. This procedure is exceedingly expensive, especially for the modeling of industrial thermal plasma flows. Thus, alternative approaches have been are sought. These approaches seek to define mass diffusion fluxes as function of the other macroscopic characteristics of the flow, such as temperature, pressure, and concentration gradients. A practical approach to obtain this term is the combined diffusion method developed by Murphy (1993); this approach is based on the definition of combined diffusion coefficients together with the grouping of species according to their parent gases. This model allows the description of a thermal plasma in chemical and thermodynamic non-equilibrium by the transport of groups of species related by their parent gases, i.e. the treatment of the diffusion is made in terms of gases instead of species. As an example, an Ar-He plasma in chemical nonequilibrium can be modeled by conservation equations of the group of species related to Ar (that is, Ar, Ar^{+}, Ar^{++}) and the group related to He (He, He^{+}). This approach is valid if the parent gases (e.g., Ar and He above) do not react with each other. Several authors have been used the diffusion method in numerical simulations of thermal plasma torches (Wang et al., 2006, Wang et al., 2007).

The highest temperatures found in thermal plasma torches are in the order of 15000 K. The temperature profile of the plasma and its maximum value depend on the separation of the electrodes, current intensity, nozzle geometry, etc. In the works presented in the literature about numerical simulations of plasma torches, only few studies validate their

temperature predictions with measurements (Hur et al., 2001) due to the complexity of the procedure.

In fact, the measurement of temperature in a thermal plasma arc is not possible with the conventional techniques, but it is possible to get an idea about the temperatures using unconventional methods related to the techniques of radiation pyrometry. One of the most spread tool is the optical emission spectroscopy (OES) (Murphy, 2001, Grinys et al., 2007, Nafarizal et al., 2009, Wang et al., 2010a, Sarani et al., 2010, Hur et al., 2001). This method is based on the spectral analysis of optical radiation emitted by excited atoms or molecules then they return to the lower energy state level. OES has been used for years to determine the plasma parameters, such as its composition, temperature and electron density. This is an advanced technique which allows the study of the physics inside the plasma without perturbing it.

In OES, energy acquired by an atom can be reemitted as radiation which is collected and analyzed by a spectrometer. From quantum theory, it is known that electrons occupy discrete energy levels. Atoms, which are characterized by the energetic configurations of these electrons, emit light whenever electrons fall from a higher excited energy level to a lower level. Typically, OES system consists in a monochromator, optical fiber, photomultiplier, and data acquisition. Figure 4.1 shows a scheme of a common spectrometer used for the diagnostic of a plasma torch.

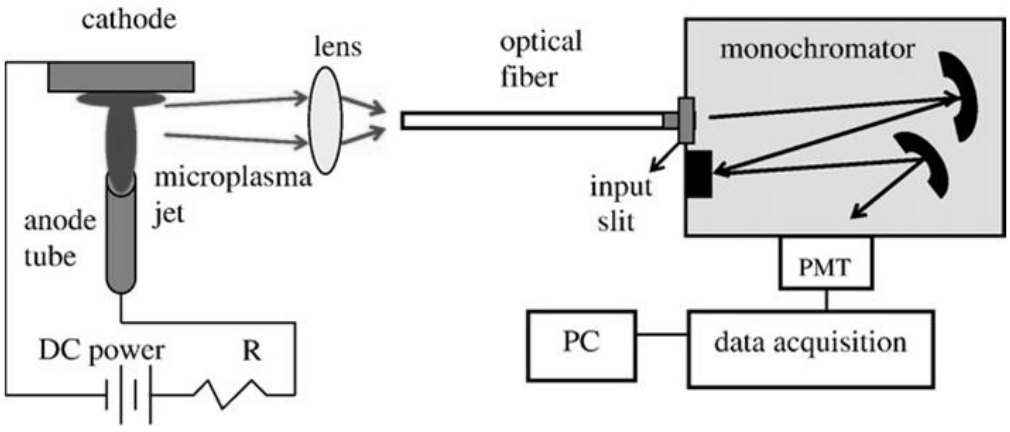

Figure 4.1. Scheme of a common spectrometer (Sismanoglu et al., 2009)

Implementation and interpretation of OES is complicated and expensive, but careful analysis can yield quantitative information.

Finally, in problems where the plasma torch is a part of a process (e.g. in this case is part of a melting process); the interaction of the torch with the processing material must be taken into account. Nevertheless, most of the works presented in numerical simulation of thermal plasmas, the resolution of the energy equation is carried out only in the plasma. The anode is assumed to be a simple surface at the domain boundary where a temperature profile or a heat flux condition is imposed as a boundary condition. Tanaka and Lowke (2007) and Wang et al. (2006) simulate plasma torches with phase change in the anode using the enthalpy method; while Tanaka and Lowke (2007) limit their experimental procedure to the measurement of the load temperature after switching off the arc with an IR pyrometer, Wang et al. (2006) omit any experimental validation. Lago et al. (2004) and Gonzalez et al. (2005) compare the estimated temperatures in the plasma torch and the heat flux to the anode with available measurements in literature; they simulate the thermal interaction between the plasma torch and the anode without considering the melting of the load, although the temperature predicted exceeds the melting point of the material.

4.2 Experimental configuration

4.2.1 Principle of operation and test protocol

Under the general objective of developing an innovative type of secondary aluminum melting furnace, experiments were undertaken with a reduced-size prototype (ca. 50 kg max. load). Experimental facilities and tests were provided and accomplished by Corporación Tecnalia (Tecnalia/Inasmet facilities at Irun-San Sebastián) in the frame of the EDEFU project (EDEFU, 2010). The heating means is a transferred plasma torch that superficially heats the aluminum load, which acts as a conducting body. The load is confined within a crucible made of refractory material. Figure 4.2(a) is a photograph of the practical experimental rig, externally showing the main elements: graphite

electrodes, plasma gas (nitrogen) injection, cooling system of the electrodes and electrical and measurement equipment. For clarity, Figure 4.2(b) shows a sectional view of the furnace.

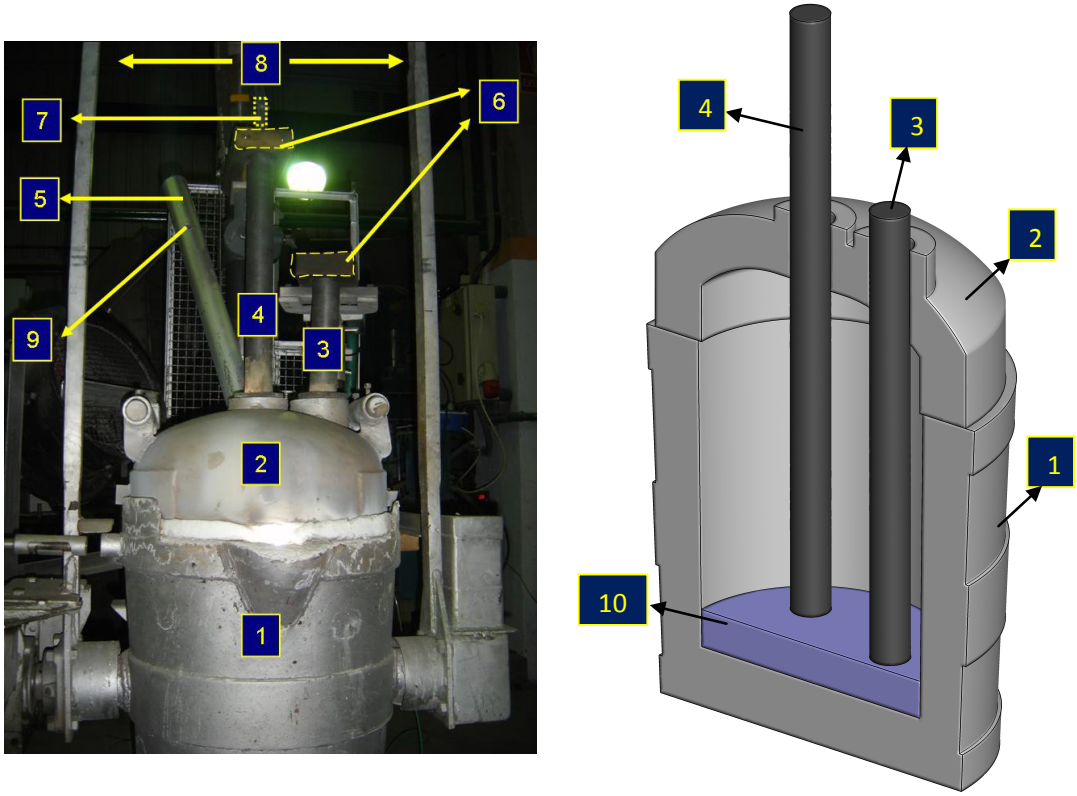

a) b)

Figure 4.2. (a) Pilot melting furnace; (b) Sectional view (1. Crucible/ ladle; 2. Top of furnace; 3. Anode; 4. Cathode; 5. Exhaust gas pipe; 6. Cooling system of electrodes; 7. Inlet nitrogen pipe; 8. Transport hook; 9. Temperature measurement sensor; 10. Load)

The anode and cathode are graphite electrodes. The anode is a solid cylinder with a diameter of 5 cm and the cathode is a hollow cylinder with outer and inner diameter of 5 and 1 cm respectively. Refrigeration is provided by a system of water circulation and is used for cooling of the supports of the electrodes. Any other part of the global prototype is not cooled with this system. The input electricity is transmitted to the electrodes through a special wire that also is used as the water duct for the refrigeration. The plasma gas used is nitrogen (N_2) that is provided from a storage tank. Figure 4.3 shows the electric/hydraulic connections for the electrode refrigeration and the connection for the N_2 supply in the cathode.

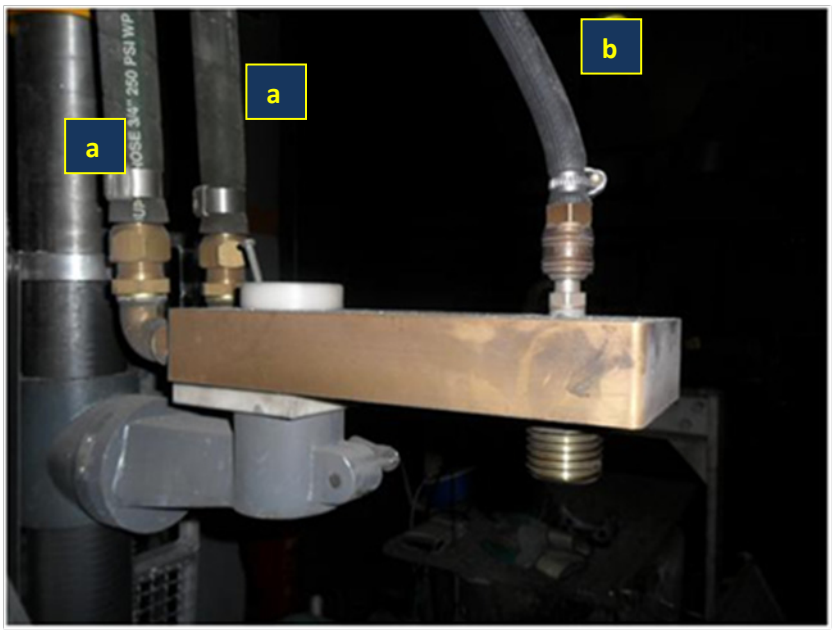

Figure 4.3. (a) Electric/hydraulic connections for the electricity supply and electrode refrigeration; (b) connection for the N2 supply

The first stage of the experimental test is preheating the crucible by a propane gas burner for two hours approximately, until it reaches the operation temperature. This is done to avoid damage due to cracking from thermal expansion; the lid is not heated. For the tests, the preheated crucible temperature was set at 658 ºC. Figure 4.4 shows the preheating process in the facility.

Figure 4.4. Preheating process for the ladle with a gas burner

The load of aluminum is weighted before the test and then it is placed inside the furnace. At the initial instant, both electrodes have to be in contact through the metallic load, so that the starting point is a short-circuit. The plasma gas is injected and the cathode is separated; at this moment the plasma torch starts and begins to heat the aluminum surface. In order to maintain a constant power input, the separation distance between the cathode and the load is frequently adjusted. After the theoretical time for melting, temperature is measured in the aluminum; once fusion of the material has been verified, it is poured into a mould. Figure 4.5 shows the appearance of the furnace during the melting process.

Several tests were carried out for different configurations, type and amounts of load and power input. A single representative case is selected for the simulations.

Figure 4.5. Appearance of the furnace in the melting process

4.2.2 Measurement equipment

An infrared IR thermograph camera is used to produce a map of outer surface temperature of different components of the furnace. The maximum temperature that

can be measured with this camera is 2000 ºC. Thermal images of the crucible are taken periodically by the camera. Since the emissivity of real objects depends, besides temperature and wavelength, on factors such as material composition, surface condition and viewing angle, the contact thermometer method was used to obtain the emissivity of the furnace wall. Temperature readings with a thermocouple provided an absolute datum to calculate the emissivity correction of the camera. Emissivity was fixed at 0.7. For the method used (narrow-band IR pyrometer), the way in which the error of the assumed emissivity is transmitted to the absolute temperature can be estimated according to (Doebelin, 1990):

$$\frac{T_{actual}}{T_{measure}} = \left(\frac{\varepsilon_{estimated}}{\varepsilon_{actual}}\right)^{1/3} \tag{4.1}$$

Since the relation of the emissivities is equal to the cubic relation of temperatures, the error on the measurement of temperatures is very low for large values of emissivities, typical of rough-finished surfaces (as in this case).

Figure 4.6 shows the IR thermograph camera and a thermal image obtained for the process.

(a)

(b)

(c)

Figure 4.6. Measurement of external temperatures of the furnace: (a) IR thermograph camera system; (b) furnace in melting process; (c) typical thermographic image

An assembly made up of a thermocouple in a steel tube that the operator shoves in the molten metal is used to measure its temperature. Figure 4.7 shows the measurement of the load temperature after the melting process.

Figure 4.7. Measurement of molten temperature

Exhaust gas temperature, which is indicative of that of the inner atmosphere, is measured through a thermocouple probe installed in the pipe. Contact thermocouple probes are used to record temperature into the wall of the crucible; the measurement point (P_m) is located at a height of 245 mm from the bottom of the crucible and at the center of the wall thickness. The electrical system includes measurement of instantaneous power and accumulated energy input.

Most of the measurements related to thermal magnitudes are taken under industrial conditions. Measurement of temperatures in solid parts and fused metal has an estimated accuracy of ± 2 ºC, whereas electric power supply is measured to within ± 0.1 kW. Load weights and times can be considered exact in practical terms. However, heat losses to ambient and initial preheat of the crucible are determined only indicatively, which is to be taken into account when comparing with numerical results. Different measurement instruments used in the test are shown in Figure 4.8.

(a)

(b)

(c)

Figure 4.8. Measurement instruments: (a) digital scale; (b) water and N2 flowmeter; (c) control box and analogue instruments for power supply

4.3 Model description

4.3.1 General assumptions and boundary conditions

Numerical simulations is undertaken with the commercial CFD code FLUENT. Pressure-velocity coupling is implemented by the SIMPLE algorithm, with the standard scheme for pressure interpolation. A first-order upwind scheme is adopted for spatial discretization. The criterion of numerical convergence by time step is to achieve a decrease of $1x10^{-3}$ in the absolute residuals of the continuity and momentum equations, and a decrease $1x10^{-6}$ in the absolute residual of the energy equation. Details of the numerical techniques are given in the user's manual (ANSYS, 2012).

In order to reduce the computational cost, the real geometry is simplified to a 2-D axisymmetric model; details such as the anode and sections of gas outlet and temperature probes are thus ignored. The load consisting in 10 kg of metal is assumed to fill the ladle uniformly from the bottom up to a specific height. The whole domain is closed: gas inlet and outlets and air infiltrations are neglected.

Heating from the plasma torch is represented by a small, circular heating area of equal diameter as the electrode, 50 mm, located at the centerline on the top surface of the load. Obviously, better models of the plasma torch can be incorporated under the same general scheme. However, as was presented before, due to the complexity of the phenomenon, there are no simple, reliable models of heat transfer from thermal plasmas. Moreover, the existing models must be calibrated with experimental measures not available for industrial applications. Given the absence of experimental observations regarding e.g., electrode and arc geometry or plasma temperature, the accuracy of any thermal model for the plasma torch is not warranted at this stage. By these reasons, an averaged power transferred to the load is used as the heat input of the simulations. Hur et al. (2001) measure the power transferred to the load in a similar application and Ünlü and Drouet (2002) present typical values for the transferred efficiency for these kind of furnaces. The authors coincide in that the fraction of energy transferred to the load ranges from 45 to 60 % depending on arc length. In this case, a value of 55% is adopted,

and a typical experimental measurement of 30 kW input electricity, input power to the load (W_{input}) is 16.3 kW. This is uniformly distributed on the assumed heating area and imposed as a boundary condition, the concentration of the energy is justified since the greatest part of the energy is given at the centre of the anode, where the total heat flux is 500 times larger than at the plasma edges (Lago et al., 2004). This simplification is often used in electric arc applications (Arzpeyma et al., 2013, González et al., 2010b, González et al., 2010a, Widlund et al., 2011). The assumption is intended as a rough approach to represent the heating means and focus the calculation on material fusion, temperatures and losses.

Gas and molten aluminum move due to thermally induced density differences. Corresponding Rayleigh numbers can be estimated as $2x10^8$ and 10^6, respectively. Although the first is relatively close to the critical value of 10^9 usually given for external flows in air (Mills, 1992), whereas turbulence transition for liquid metals heated from the top is not clear, laminar flow is considered for both sub-domains, which additionally simplifies the problem.

Heat losses from the external surface of the crucible to the surroundings are approximated as follows. The bottom is considered perfectly insulated. In the remaining external walls, heat transfer by natural convection and radiation takes place. A constant, average heat transfer coefficient $h_{av} = h_{conv} + h_{rad}$ [W/(m^{2}K)] is estimated according to elementary heat transfer calculations (Incropera and DeWitt, 1990). It should be noted that, since the major part of temperature decrease occurs in the refractory parts, not a precise value but only an indicative figure is needed here. For the convective coefficient h_{conv}, an empirical correlation for the ideal geometry of a vertical cylinder is applied. Radiation is estimated through the formula giving the losses to a large (thus, black) radiative environment. Both coefficients depend on surface and ambient temperatures, assumed uniform and known. Values of 250 ºC and 18 ºC, respectively, are used, the former confirmed as representative of the typical average of numerical results for the surface temperature distribution. Total emissivity used is 0.7, estimated from the measurement of the superficial emissivity presented above. Calculation results in $h_{conv} \approx 7.2$ W/(m^{2}K), $h_{rad} \approx 11.7$ W/(m^{2}K), and thus $h_{av} \approx 18$ W/(m^{2}K).

4.3.2 Geometry and materials

Main dimensions of the melting furnace are shown in Figure 4.9(a), and the geometry adopted for numerical computations is shown in Figure 4.9(b), detailing the different computational sub-domains. Material used for the refractory parts (crucible and top lid) is high alumina, whereas load is made up of alloy AlSi9Cu3. Thermophysical properties are given in Table 4.2 and Table 4.3, respectively. Only density of molten aluminum is considered variable with temperature; the remaining magnitudes are (reasonably) assumed constant. Gas inside the ladle is represented by standard dry air at atmospheric pressure, and calculated as an ideal gas.

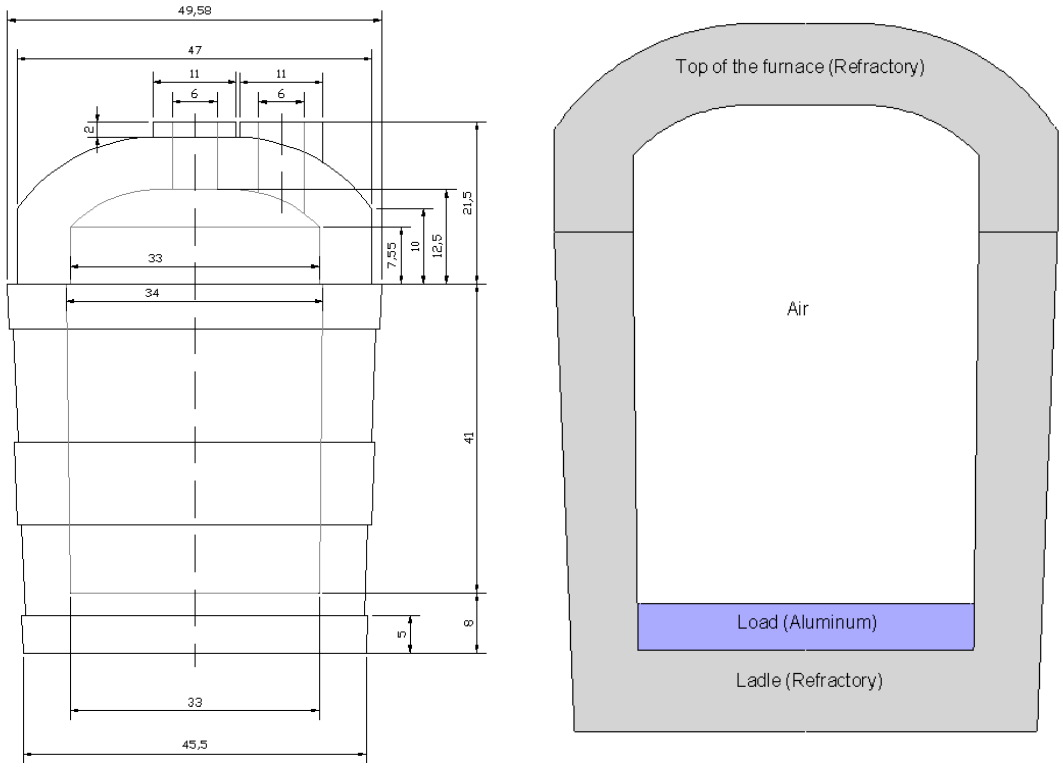

a) b)

Figure 4.9. a) Main dimensions of melting furnace; b) Geometry for the numerical simulations

Table 4.2: Thermophysical properties of refractory (Carbosanluis, 2007)

Density (kg/m^3)	2150
Specific heat (kJ/kg.K)	0.850
Thermal conductivity (W/m.K)	1.5

Table 4.3: Thermophysical properties of aluminum load

Density (kg/m^3)[a]	2700	$T < 873$ K
	-3.873T+5992	873 K < T < 933.15 K
	-0.3116T+2668	T > 933.15 K
Specific heat (kJ/kg.K)[b]	0.900	
Thermal conductivity (W/m.K)[b]	237	
Viscosity (kg/m.s)[a]	0.001	
Latent heat of fusion (kJ/kg)[b]	397	
Solidus Temperature (K)[c]	873	
Liquidus Temperature (K)[c]	933.15	

[a] Assael et al. (2006); [b] Brandt (1984); [c] Zeiger and Nielsen (2004)

4.3.3 Simulation of gas cavity

The physical model consists in the numerical solution of the appropriate differential conservation equations for all domains involved. On the one hand, mass continuity and momentum conservation (Navier-Stokes equations) are solved for liquid aluminum and air filling up the ladle, which takes into account buoyancy; solid parts are considered incompressible. Non-slip, or velocity continuity, is imposed on all interfaces. The air-aluminum interface in the furnaces is fixed and the volumetric expansion effect is neglected. On the other hand, energy conservation is solved in refractory, load and air, which is equivalent to a problem of heat conduction in solids and heat convection in air and liquid aluminum. The method used enforces temperature continuity and conservation of heat flux through interfaces. Energy conservation in the load is formulated in terms of total enthalpy, to serve to the enthalpy method, which is used to model the phase change of the metal.

An accurate model of heat losses must incorporate the transfer of energy by thermal radiation between the surface of the load and inner surfaces of the ladle. Such a mechanism is expected to contribute in an amount comparable to heat convection in the gas. This is an added complexity to the already complex model of heating and phase

change. However, since heat losses by radiation are actually only a small fraction of the input energy, it is reasonable to consider simplified models of the gas cavity. The idea is to develop a simplified simulation by considering successively simpler and thus more economical and less reliable models. Aside from estimating the accuracy of the different simulation results, the progressive reduction in computational workload is also monitored. Five different cases are calculated, as described below from the more complex to the simplest one; the latter even disregard movement of one or two of the fluids. The objective is to assess the applicability of the different schemes to the comprehensive simulation of realistic, complex industrial systems, which often requires a judicious use of limited computational resources.

4.3.3.1 Case 1: Thermal radiation and air convection fully modeled

This is the more precise and expensive model of the gas cavity, which is taken as a reference for the remaining cases. Thermal radiation is calculated by the S2S radiation model presented in Chapter 3.

4.3.3.2 Case 2: Radiation no modeled

Radiation is simply not taken into account, in order to determine the effect of this rough approximation both on the fictitious reduction of heat losses and on the economy of the calculation.

4.3.3.3 Case 3: Purely diffusive transfer in the gas, with an augmented, effective thermal conductivity

An approximate way of handling convective and radiative heat losses from the top surface of the load is to adopt a constant, overall heat transfer coefficient [W/(m^{2}K)], h_{eff} = h_{conv} + h_{rad}, that can be estimated for typical temperature differences and idealized conditions. This is of course completely similar to the consideration of losses from the outer surface of the ladle, and can be justified given the reduced magnitude of the term. Heat fluxes [W/m^2] from/to cavity surfaces are then calculated as $q = h_{eff}\Delta T$, where ΔT is the difference between the local surface temperature and the temperature of the inner atmosphere of the cavity T_{cav}. However, the value of T_{cav}, intermediate between

maximum (load) and minimum (lid) surface temperatures, is unknown a priori, resulting from the balance of energy input, heat of fusion of the material and external losses. An energy balance to the cavity would allow to calculate T_{cav} coupled to the numerically calculated temperature distributions in load and refractory sub-domains. Unfortunately, FLUENT doesn't implement directly such a scheme, thus rendering it iterative. A too-high/low guessed value of T_{cav} would lead to an artificial heat source/sink in the cavity that would be corrected by lowering/raising the guess.

Given the complexity of the numerical solution, this would be obviously very costly, but a better alternative can be implemented. Instead of assuming a uniform T_{cav}, the inner temperature of the cavity is allowed to vary spatially according to a purely diffusive process. Treating losses in the gas cavity as pure heat conduction then allows to improve on the assumption of a constant T_{cav}, and at once is much cheaper than calculating gas convection plus radiation.

Now, since heat conduction in a flat layer of thickness t_c is given by a Nusselt number $Nu = ht_c/k = 1$, the fact that real heat transfer by convection and radiation is more intense can be represented by an augmented thermal conductivity given by $k_{\text{eff}} = h_{eff}t_c$. Considering the cavity as a cylinder with the inner diameter of the ladle and height t_c = 0.5 m, and uniform surface temperatures of 660, 100 and 500 [ºC] in load, lid and lateral wall, respectively, coefficients are estimated according to basic heat transfer calculations (Incropera and DeWitt, 1990). Results are $h_{conv} \approx 3.4$ W/(m^{2}K), $h_{rad} \approx 29.5$ W/(m^{2}K), $h_{eff} = h_{conv} + h_{rad} \approx 33$ W/(m^{2}K), so that conductivity is taken as $k_{eff} = 16.5$ W/(m.K).

Finally, although gas is considered still in this approach, the interface surface with the load is allowed to move by imposing there a free-slip boundary condition. In this way, movement of molten aluminum is predicted.

4.3.3.4 Case 4: Cavity not modeled

Invoking again the small value of heat losses, perfectly insulated surfaces ($h_{eff} = 0$) can be specified for the cavity, so that the load only losses heat by conduction to the refractory where it touches it. This is obviously a rough approximation, which will over-

/underestimate energy efficiency, temperatures, fusion times, etc. However, it amounts to a large computational economy, since it is equivalent to treat the cavity as a vacuum, i.e., to avoid modeling it. As in case 3, movement of the fused load is allowed by imposing a free-slip top surface.

4.3.3.5 Case 5: Cavity not modeled and load heated by pure conduction

In addition to the assumptions of the previous case, density of solid and liquid aluminum is taken as a constant, ρ_{load} = 2400 [kg/m^3], an average of the values shown in Table 4.3. This suppresses natural circulation in the material, which amounts to the simplistic model of considering inner heat transfer driven exclusively by diffusion. This is obviously another reference case: the computational expense is the minimum that can be imagined, amounting only to solving the heat conduction equation everywhere, with the addition of the phase change model in the load.

4.3.4 Numerical time step

Simulations are carried out for a transient process. In phase change problems, convergence of the numerical iteration can be very difficult to reach; therefore, selection of a suitable time step is of paramount importance. In this approach, iterative convergence is assured at each time step. Different values were tested, which resulted in that the required maximum value should be lower the complex the problem solved. Values finally adopted for cases 1-5 are, respectively: 0.0005, 0.00075, 0.01, 0.1, 1 s.

4.3.5 Meshing scheme

Due to the diverse complex phenomena involved, the implementation of the numerical simulations is very expensive in computational terms. Therefore, currently it is not feasible to carry out a grid convergence study, and only a single mesh of 18 116 cells is used in the present work. The number of cells allotted to the different sub-domains is as follows: ladle (5 749 cells), lid (2 522 cells), load (825 cells) and air (9 020 cells). These last cells are not used in cases 4 and 5. Figure 4.10 shows the grid used for the simulations.

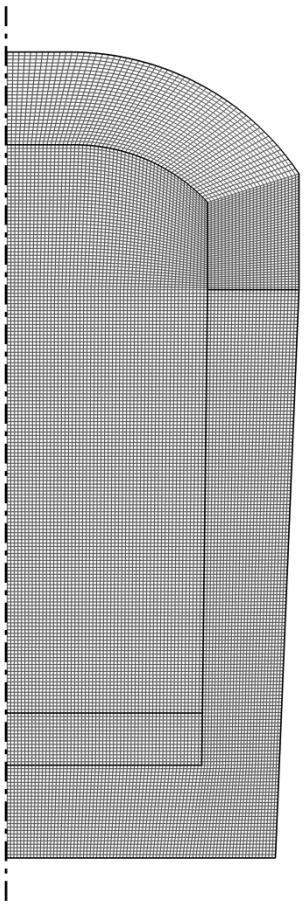

Figure 4.10. 2-D axisymmetric grid for the numerical simulation

4.4 Preheating of the refractory ladle

As described before, the process doesn't start from cold conditions but firstly the ladle is preheated by a gas burner impinging on its inner surface. This imposes an initial internal energy content and a temperature distribution in the refractory material, and both should be taken into account. Therefore, firstly the preheating process is simulated, and its final state is taken as the initial one for the ensuing simulation of the fusion of the aluminum load.

The rather complex and uncontrolled actual process is approximated as a constant and uniform heat flux entering the inner surfaces of the ladle, with the remaining area subjected to heat losses to the environment. Load, top lid of the furnace and air are not

simulated at this stage. Assuming that the temperature of the refractory material is increased 500 ºC in average for all the volume during a time interval of two hours, a heat flux of 15 000 W/m^2 can be estimated. The preheating process starts from ambient temperature and lasts for 7 200 s. A large numerical time step of 5 s is used, adequate for simple heat conduction problems.

Results and comparison with experimental measurements can be discussed as follows. Figure 4.11 shows the calculated final temperature distribution in the ladle material, as well as the position of the temperature measurement point P_m. Final temperature along the thickness of the crucible wall at the same height is shown in Figure 4.12.

Temperatures numerically predicted are 1050, 775 and 625 K for the inner wall, measurement point and outer wall, respectively. These estimations agree reasonably with experimental observations, in which inner wall temperature ranges from 950 to 1180 K, temperature of the measurement point P_m is 750 K, and outer wall temperature ranges from 509 to 600 K.

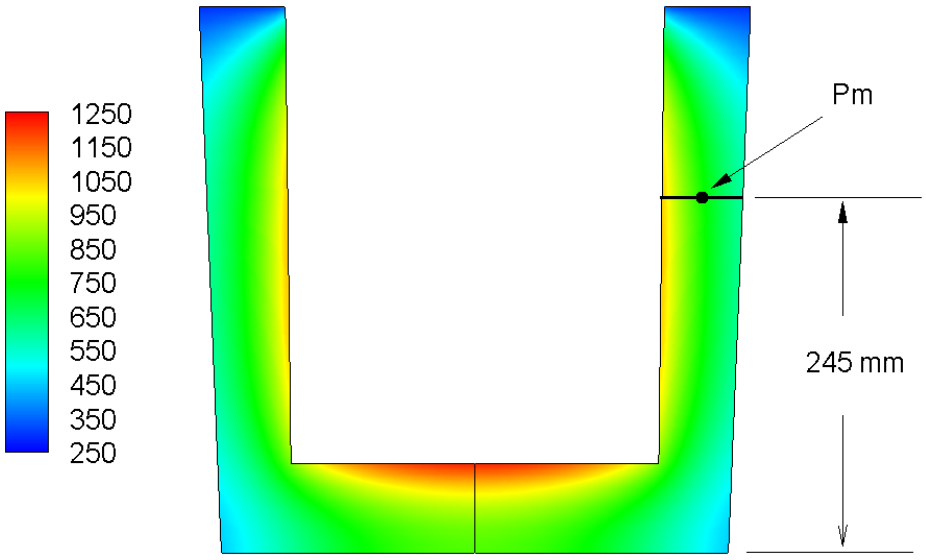

Figure 4.11. Temperature distribution [K] in the crucible at the end of the preheating stage

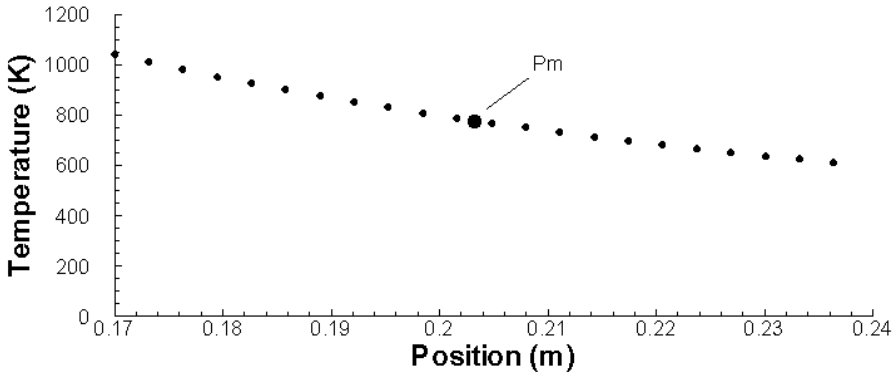

Figure 4.12. Temperature along the thickness of the refractory wall at the end of the preheating process

The temperature distribution shown in Figure 4.11 is taken as the initial one in the refractory material for the transient simulation of aluminum melting. Top lid, air and load are added at ambient temperature to complete this initial state.

4.5 Results and discussion

4.5.1 Melting time

An approximate melting time (t_m) can be calculated by assuming heat is communicated to the load at a constant rate. Total heat needed for melting is:

$$Q = mC\Delta T + mL \tag{4.2}$$

Where $\Delta T = T_m - T_0$ is the increment from ambient to fusion temperatures. Thus,

$$t_m = \frac{Q}{W_{input}} = 560\ s \tag{4.3}$$

Melting time predicted by the simulation is measured by a monitor of the melting fraction, defined as total amount of molten aluminum divided by the initial solid load. For cases 1-5, predicted melting times are 625, 603, 622, 614, 584 s, respectively. Experimental value is 671 s, although this includes some overheating of the fused

aluminum. In conclusion, numerically predicted times agree reasonably, both with approximate guesses and with measurement.

Figure 4.13 shows total liquid fraction in the load throughout the simulation time for the five cases studied. Behavior of the melting rate is roughly the same for the two models including radiation (cases 1 and 3), that correspondingly predict similar melting times. Compared with them, simulation without radiation (case 2) and without the whole gas cavity (case 4) exhibit a similar melting rate for, say, the initial five sixths of the process, but clearly accelerate during the last sixth. This is an indication that radiative losses logically predominate at latter stages, under increased load temperatures; the effect is more pronounced for case 4 than for case 2, which is also coherent. Finally, case 5 overpredicts load temperature and leads to a shorter melting time. Difference with case 4, and the lack of it between cases 2 and 4, clearly show that influence of heat convection inside the load surpasses that of losses through the gas cavity.

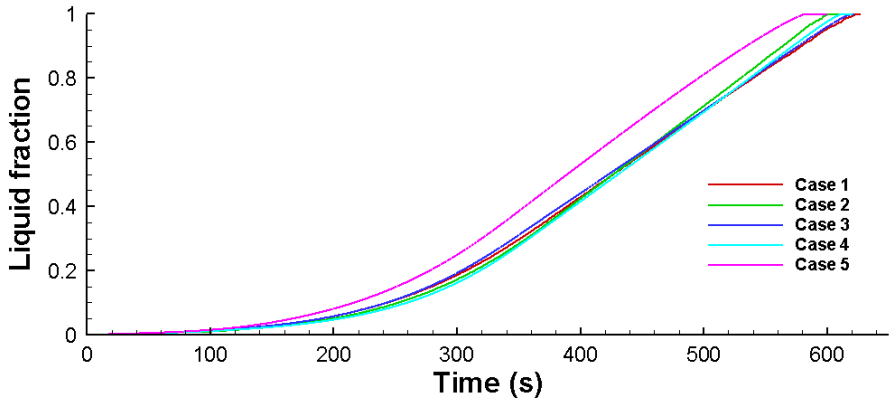

Figure 4.13. Liquid fraction in the load throughout simulation time for five study cases

4.5.2 Distribution of liquid fraction

Figure 4.14 and Figure 4.15 show liquid fraction distribution for cases 1-5 at times 150 and 480 s, respectively. The gas cavity sub-domain is not colored in these drawings.

The shapes clearly suggest that melting is initially controlled by heat conduction, and at a certain time, effects of natural convection inside the load become important. In the last figure, differences between cases 1 and 2 on the one hand, and cases 3 and 4 on the

other pinpoint the effect air movement has on movement of the molten load. Input heat seems to extend superficially more, but to a lower depth, when surface is assumed free, not subjected to the shear stress needed to drag air along. Similarity between cases 3 and 4 indicates that this is unaffected by heat losses from the surface of the load. Finally, a pure heat conduction situation, for a very conductive material, is clearly observed for case 5.

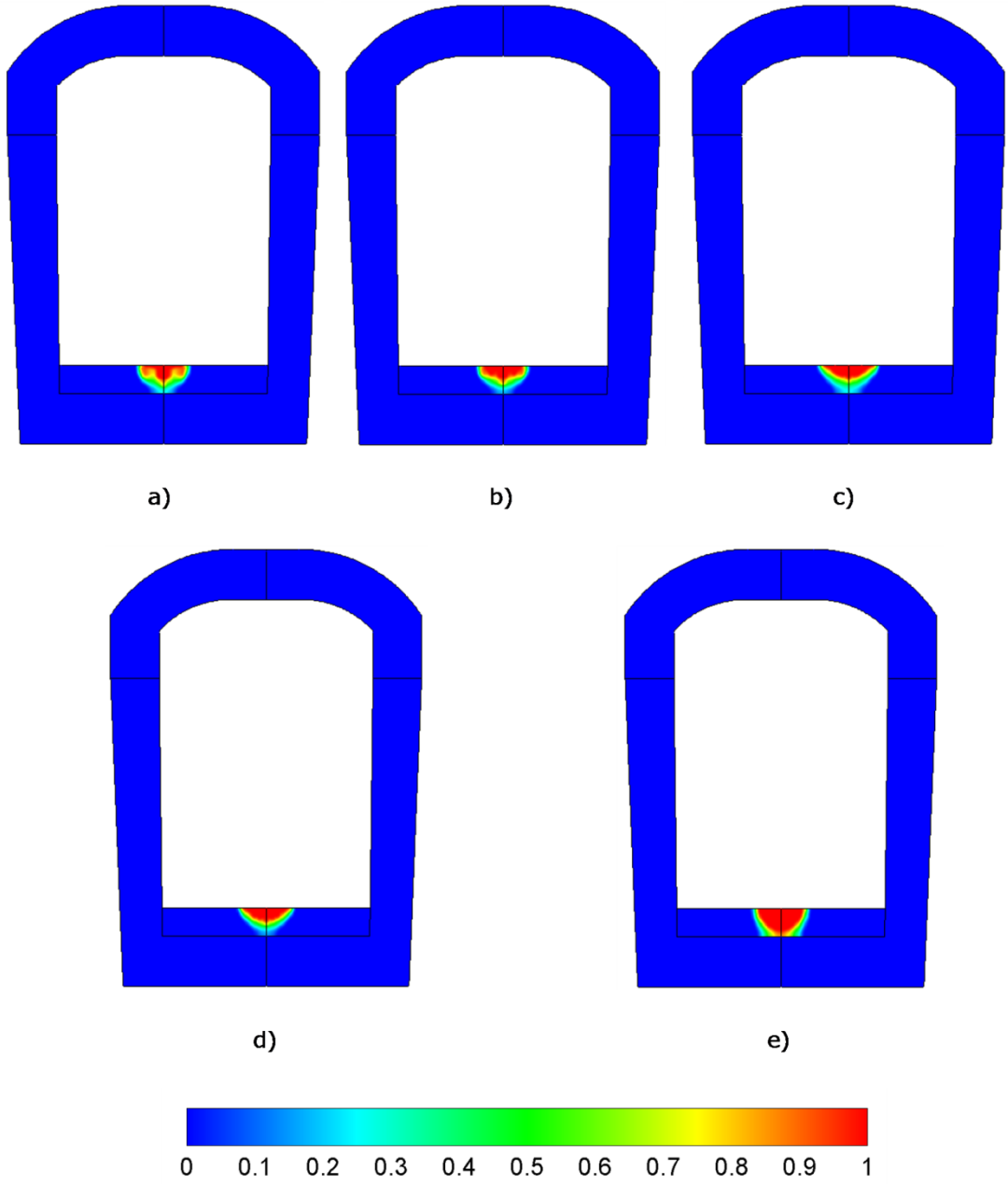

Figure 4.14. Liquid fraction at *t* =150 s: a) Case 1; b) Case 2; c) Case 3; d) Case 4; e) Case 5

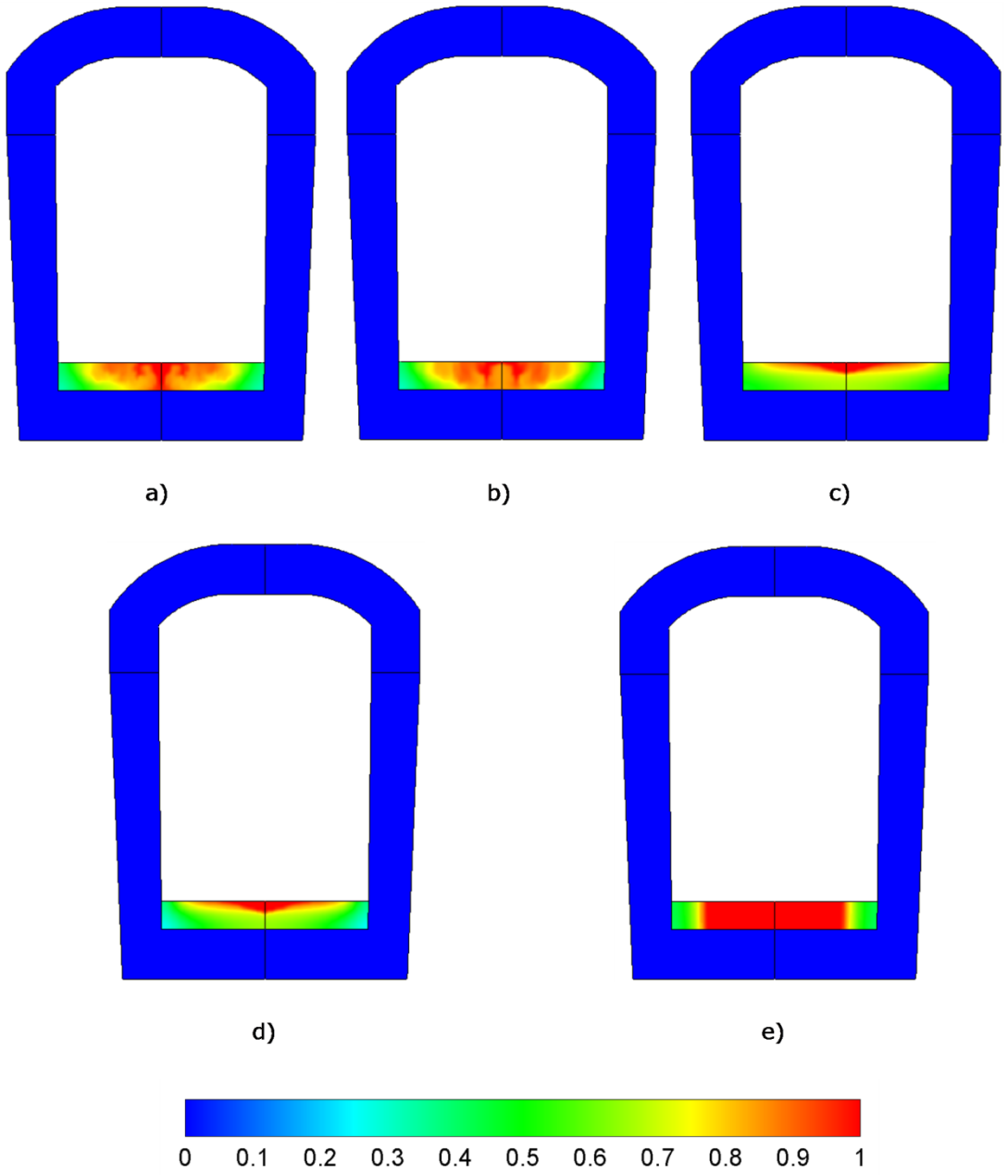

Figure 4.15. Liquid fraction at t = 480 s: a) Case 1; b) Case 2; c) Case 3; d) Case 4; e) Case 5

4.5.3 Temperatures

Figure 4.16 and Figure 4.17 show color maps of calculated domain temperature for cases 1-5 at times 150 and 480 s, respectively.

For comparison purposes, Figure 4.18 shows thermal images of the outer surface taken during the experiment at times 150 and 480 [s], as well as the values estimated at

specific points on the ladle, lid and electrodes. Figure 4.19 shows the evolution of temperature of gas inside the cavity and wall of the crucible.

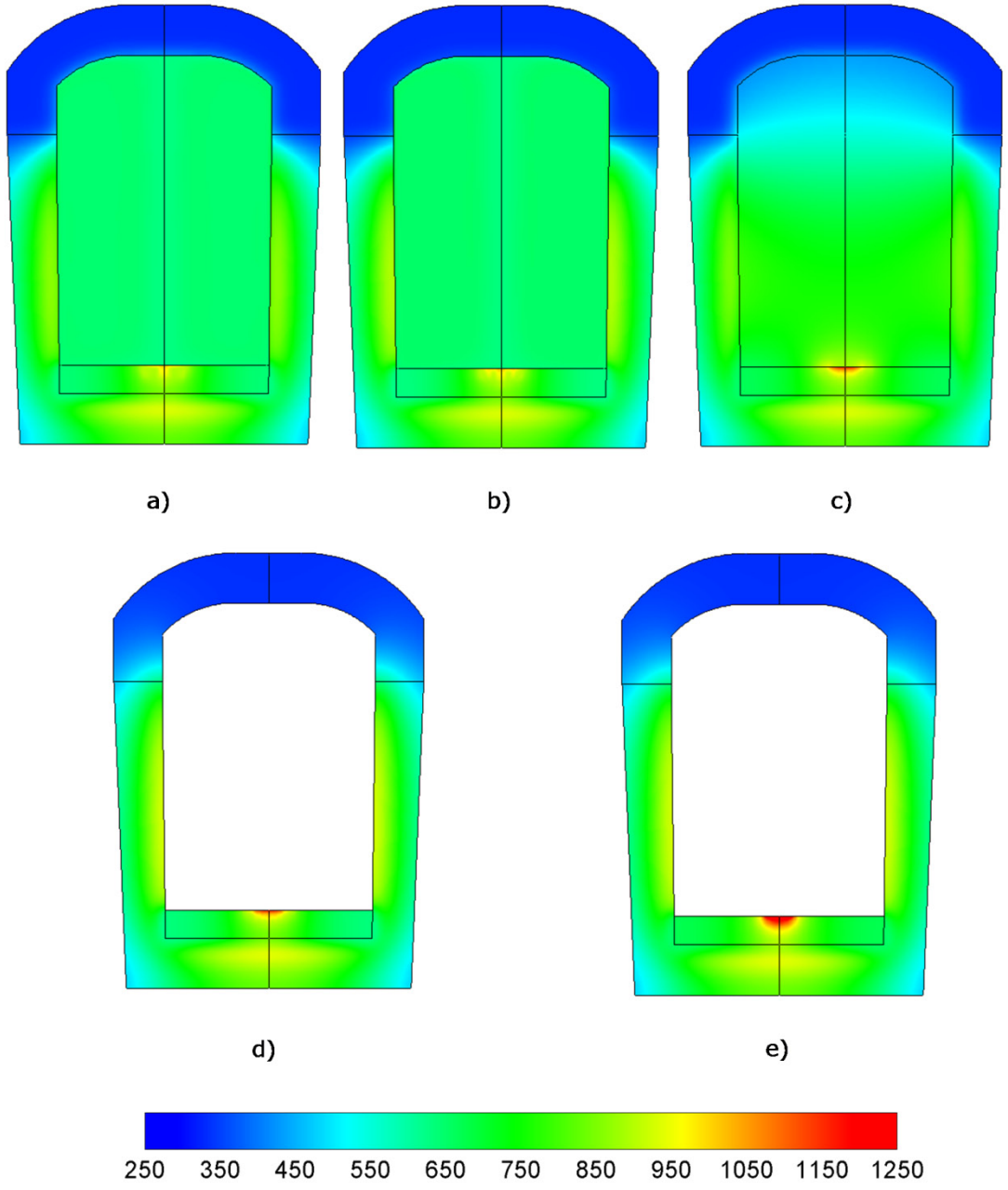

Figure 4.16.Temperature [K] at *t* = 150 s: a) Case 1; b) Case 2; c) Case 3; d) Case 4; e) Case 5

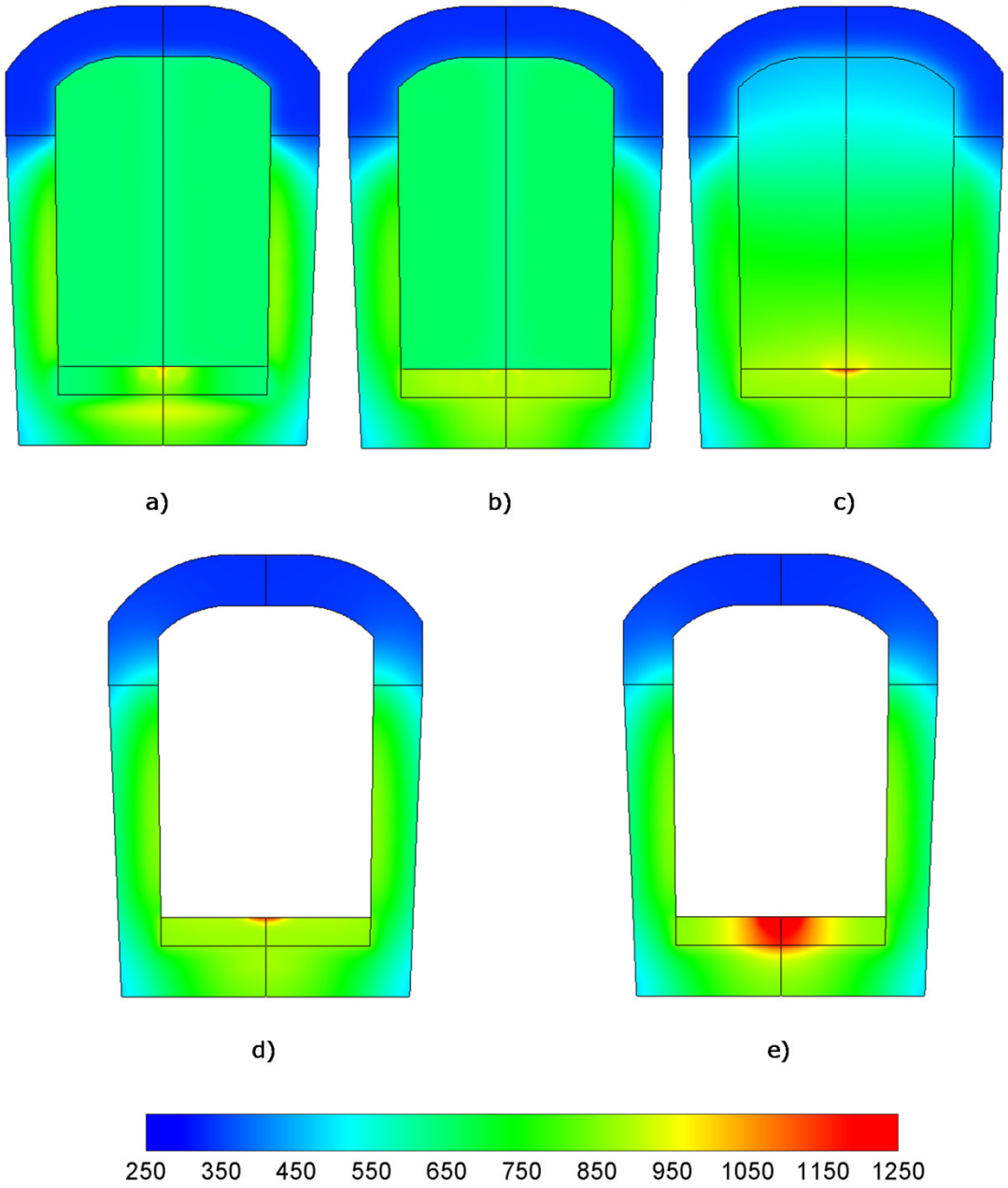

Figure 4.17. Temperature [K] at t = 480 s: a) Case 1; b) Case 2; c) Case 3; d) Case 4; e) Case 5

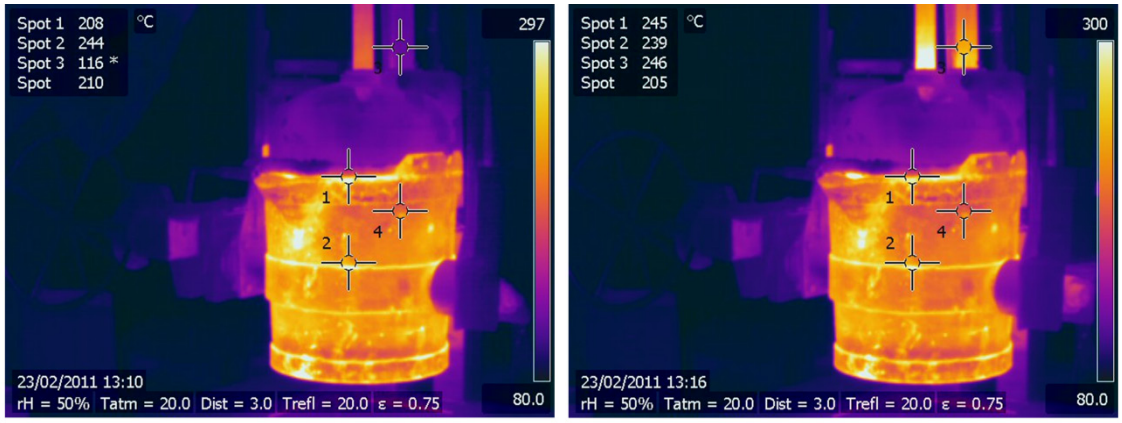

Figure 4.18. Thermal images of the outer crucible surface: a) t = 150 [s]; b) t = 480 [s]

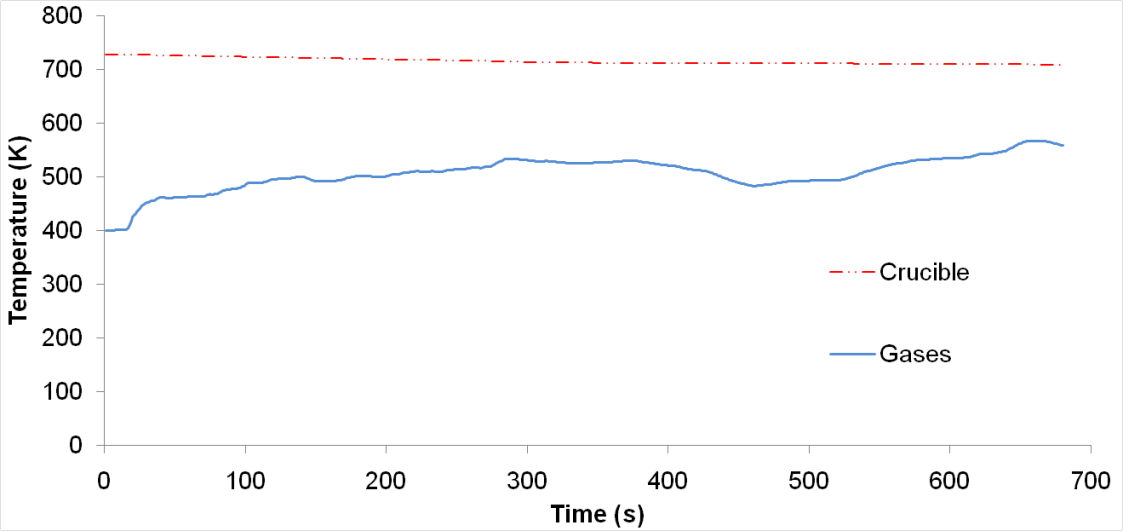

Figure 4.19. Evolution of measured temperatures of crucible wall and gases

Outer surface temperatures predicted by the simulation, Figure 4.16 and Figure 4.17, range from 500 to 600 [K] for t = 150 [s] and 450 to 550 K for t = 480 [s]. These values agree reasonably with the thermal images presented in Figure 4.18, that show 483 to 517 [K] for t = 150 [s] and 478 to 512 [K] for t = 480 [s]. Temperature predicted in the measurement point P_m ranges from 750 to 850 [K] for t = 150 [s], and 700 to 800 [K] for t = 480 [s], which agrees with experimental values shown in Figure 4.19. It is interesting to note that the temperature of the crucible continuously decreases, which means that it supplies a part of the energy to the process, that it is subsequently distributed for load heating and losses to the environment. Gas cavity temperature predicted by the full

model (case 1) ranges from 500 to 700 K, which is of the same order than the experimental value in Figure 4.19.

Experimental measurements of the inner wall temperature are shown in Figure 4.20, as estimated by thermal images taken at the end of the test, when the top lid of the ladle is removed. Values range from 700 to 950 [K], which is also in agreement with numerical estimations.

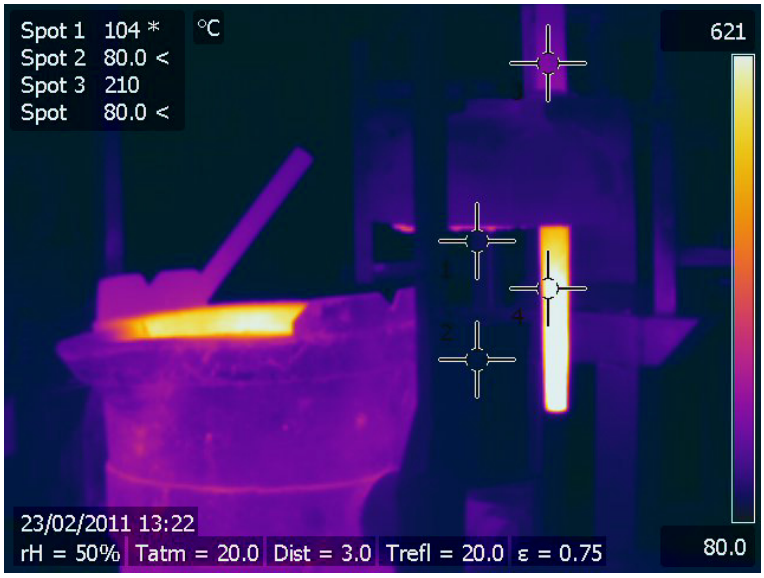

Figure 4.20. Thermal image at the end of the test

Final load temperature predicted in case 1 ranges from 933 to 950 [K], with hot spots of 1200 K. This value corresponds to the time at which all the metal load is in liquid phase, t = 627 [s]. Load temperature at the end of the experimental test, for t = 671 [s] is 1030 K, which further shows that calculation and experiment agree reasonably.

4.5.4 Molten load movement

Figure 4.21 shows velocity vectors in the liquid aluminum for cases 1-4 at the end of the melting process. It is observed that four concentric recirculation zones are predicted in cases 1 and 2, whereas only one is formed in cases 3 and 4. This is coherent with the differences observed in Figure 4.15, and points out the fact that a full model of air movement and coupling at the interface are needed to adequately predict natural circulation of the molten metal. It is important to note that industrial-scale hot melting

experiments are very expensive and complicated. Moreover, as known, until now there are no workable technical means for velocity measurements in high-temperature liquid metals (Ben-David et al., 2013). Therefore, a validation of the estimated flow is not possible with the current measurement techniques. Nevertheless, the flow patterns predicted in cases 1 and 2 agree with the roll cells expected for circular containers in convective problems. (Gebhart, 1988).

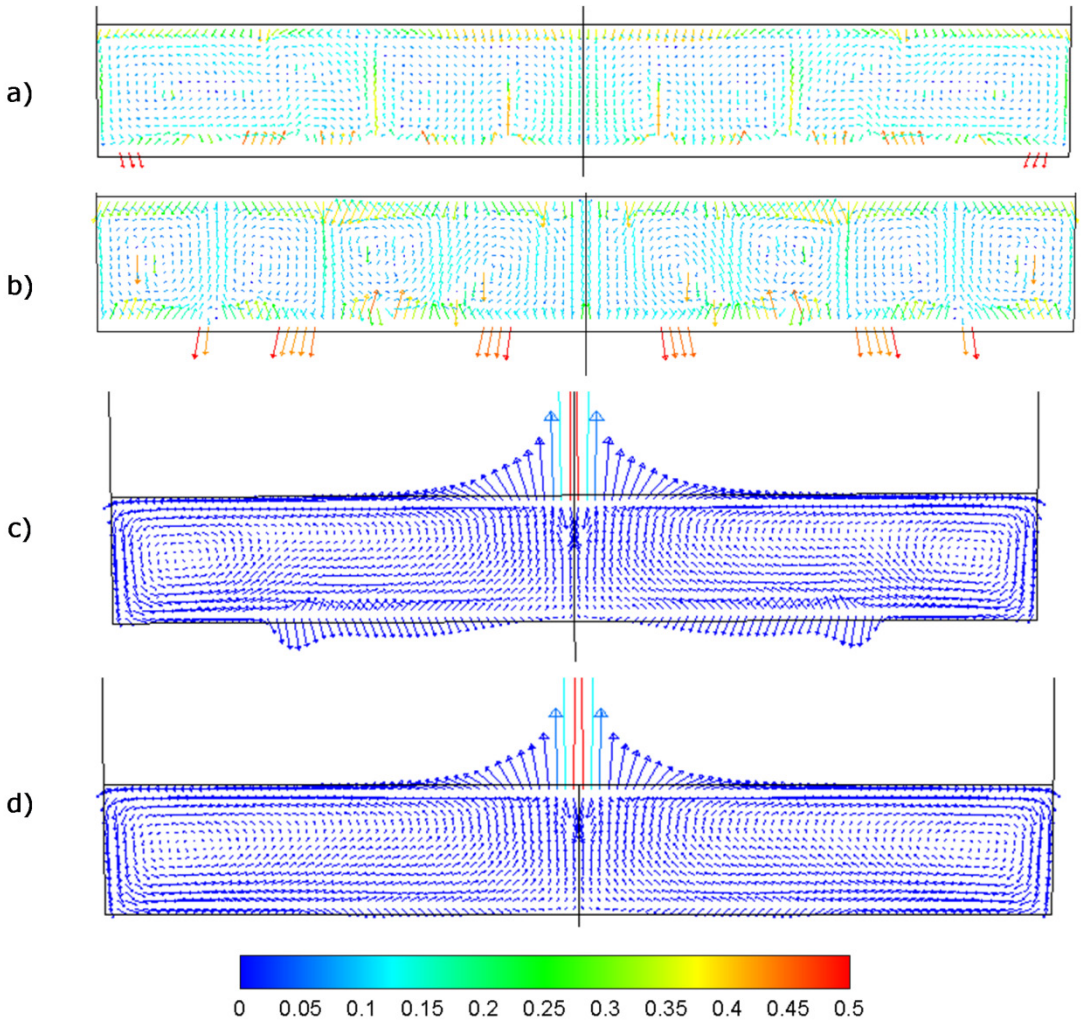

Figure 4.21. Velocity vectors [m/s] for the molten aluminum at the end of the melting process: a) Case 1; b) Case 2; c) Case 3; d) Case 4

From preceding results, it is clear that differences in local temperature and liquid fraction are important, but not so overall figures, such as melting time and overall liquid fraction, Figure 4.13.

4.5.5 Energy balance

Table 4.4 presents the energy balance of the transient process for the five cases computed, along with estimated data for the experimental assay. The energy balance reduces to the statement that estimated input thermal energy (55 % of measured electrical input) plus heat given away by the preheated refractory ladle equals heating and fusion energy of the aluminum load, plus heating of the crucible lid, heating of the air inside the cavity and accumulated heat losses to ambient. It should be noted that some of these terms can be determined experimentally only with a very large uncertainty. This is the case of losses from crucible walls and internal energy supplied by the refractory material, that are based (as discussed) on indicative surface temperatures or very localized inner material temperatures. The simulation developed achieves very good accuracy in all terms, but the relative character of empirical data should be taken into account, since computational methods are logically adapted to empirical input, as it has been explained.

Table 4.4: Terms of the energy balance (KJ) and time (s) for each computational case and experimental data

	Case 1	**Case 2**	**Case 3**	**Case 4**	**Case 5**	**Experimental**
Δ internal energy top	1517.6	863.9	1596.6	106.5	103.4	NA
Δ internal energy ladle	-3543.3	-3108	-3904.7	-2828.3	-2558.9	-2781.9
Δ internal energy load	10082	10081	10311.1	10455.8	9810.1	10621
Δ internal energy air	19.4	18.6	20	0	0	16
Input thermal energy	10211.3	9934.5	10129.9	9999.6	9511	10927.9
Lateral wall losses	2124.8	2070.8	2095.1	2257.4	2148.5	2802.1
Top wall losses	10.8	8.2	11.8	8.2	7.9	NA
Total time of the process	627	610	622	614	584	671

NA: Not available

4.5.6 Computational resources

Table 4.5 presents the consumed computational resources for each model, taking the cheapest case 5 as the basis for comparison.

Table 4.5: Consumed computational resource for each computational case

	Relative time to case 5
Case 1	2160
Case 2	1350
Case 3	600
Case 4	21.8
Case 5	1

The most accurate model (case 1) consumes 3.6 times the computational resources of the simplified case by effective coefficients (case 3). This latter is thus a good option to take into account the effects of radiation in this kind of furnaces. However, cases 3 and 4 present very similar results in basic parameters, such as operation temperature and melting time, and similar profiles for liquid fraction and velocity in the molten load. In this sense, considering that the time of calculation for case 3 is significantly higher than that of case 4, the use of the latter should be recommended for estimates in industrial problems where detailed calculation of flow in the molten load or radiation losses are not needed. Although simulations in case 5 are 20 times less demanding than case 4, inaccurate results are obtained even for overall magnitudes, which don't make advisable such strong simplifications of the calculation.

5. Numerical simulation of an aluminum holding furnace

An experimental prototype of holding furnace heated by an electrical resistances system is numerically simulated in this chapter. Models used take into account the same complexities presented in the simulations of the melting furnace, but in this case the models are 3D. As a first approach, the symmetry of the geometry is used to reduce the computational resources and only a quarter of domain is initially simulated. Nevertheless the predicted velocities for the flow in the molten load, suggest that the patterns induced by the convection effects have a three dimensional behavior. For this reason a new simulation with the full domain is carried out. Both simulations predict almost the same temperatures and energy distributions with different patterns of flow in the molten load. A chaotic behavior is predicted by the full domain approach for the movement of the aluminum bath, which correspond to problems of natural convention with small differences in temperature due to the high thermal conductivity of the material. The preheating of the furnace is the most important process involved since the high temperatures reached by the walls are used for the holding; simulations are focused on the unsteady heat transfer process of this device where the input power is performed by an on-off control. The background in numerical simulations of holding furnaces, the prototype analyzed, models used, main assumptions, methodology of the simulations, results obtained and comparison with experimental data are discussed in detail in the following sections.

5.1 State of the art in numerical simulations of holding furnaces

Some of the challenges that have prevented the intensive use of computational techniques in design of holding furnaces are the interactions gas-liquid-solid, conjugate heat diffusion through solid and fluid volumes, movement of the molten load, radiation heat transfer, 3D geometries and heating means. Additionally, the load material can present a phase change depending of the time and space when the heat supply is not enough. Therefore, for a comprehensive numerical simulation, high computational resources are required.

Only few publications have been made about numerical simulations in holding furnaces. Zhou et al. (2010) simulate combustion in an aluminum holding furnace; the model is three dimensional and considers the combustion in the chamber and its energetic interaction with the molten load. The furnace is simplified as a non-conjugate stationary problem and the momentum equations are not solved for the molten aluminum. Temperature predictions of the combustion space are compared with experimental measurements, but measurements are not presented for the molten bath. Pauty et al. (2000) present numerical simulations of holding and tilting processes in an aluminum furnace; in the holding process, the domain is considered two dimensional and conjugated in steady state; the heating is performed by a boundary condition of fixed temperature at the top of the molten load. Although the density of the molten aluminum is treated with the Boussinesq approximation, the load flow field never converged due to numerical oscillations and this is attributed to a source of turbulence that not was taken into account in the model. Darwish (1991) uses simplified correlations in order to model the heat transfer in an aluminum holding furnace in a 2D conjugated problem; the results predict a difference of the load temperature which is attributed to the shape of the furnace.

A transient scheme of a combustion process in a reverberatory aluminum holding furnace is simulated by Zhang et al. (2012). The model is three dimensional and considers a constant temperature (close to the melt temperature) in the interface

combustion/melt. In this approach the load is not considered. Tripathi et al. (2012) develop a numerical simulation of several transient processes for molten steel in a ladle, including the holding and transportation stages of the load. Any radiation loss from the load or furnace is considered as a boundary condition. The domain is modeled in a full 3D approach considering the conjugated interaction with the walls as a purely diffusive problem, i.e. the convection effects are not modeled. For this reason the estimated temperatures in the molten load present a marked thermal stratification. González et al. (2010a) analyze the fluid flow in the molten steel of an electric arc furnace. The domain is three dimensional and no conjugated and the temperatures of the walls are fixed to a value close to the liquidus temperature of low-carbon steel. The heating of the load is performed with a self-developed simplified model of heat transferred from the electrodes. The movement of the molten bath is induced by natural convection, whereby the Boussinesq approximation is employed to compute density differences. Juárez et al. (2009) evaluate the performance of different mechanical stirrers in a reverberatory furnace through an experimental study in a scaled prototype and a numerical simulation. The study is developed for water in isothermal conditions. The domain for the numerical approach is a simplification of the real prototype; the results are used to analyze details of the flow patterns.

Other numerical simulations have been developed for induction holding furnaces. In these cases, as in the melting furnaces, the Maxwell equations must be coupled to the fluid equations. The fluid flows are induced mainly by the Lorentz force rather than the buoyancy effects. Spitans et al. (2010) for 2D and Spitans et al. (2011) for 3D simulate the heating and movement of a molten material in an induction coreless furnace. The main aim of these works is to estimate the shape and dimensions of the meniscus induced by the Lorentz force. Therefore, the VOF model is used with the CFD approach and they are coupled to FEM code that solves the Maxwell equations. Courtessole and Etay (2013) present a similar work in a two axi-symmetrical domains for two immiscible liquids, a molten metal and a salt layer. The molten metal presents a meniscus and the interface is deformed, the equations are solved in a variable grid in three stages, in the first step the shape of the meniscus is computed with the electromagnetic equations

and the VOF model, in the second step a new mesh is computed with the predicted boundary, and finally, the flow equations are solved for the new domains separately. Kirpo et al. (2008) simulate the flow and thermal process inside a channel furnace for a material with melting point of 72 ºC. The model is three dimensional and the general velocity is compared with measurements in the channel using permanent magnet probes. The electromagnetic equations are modeled by FEM and are coupled to the CFD solution. The same scheme was used by Pavlovs et al. (2011) in order to simulate the flow and the temperature field in an industrial induction channel furnace with a widened channel branch and different iron yoke positions. The symmetry of the furnace was used to reduce the computational domain. In this case, the distributions of alloying additions into the melt were obtained using a Lagrangian approach. All these approaches exclude in their formulations the conjugated thermal interaction, the interaction with the air cavity and a comprehensive treatment of the heat losses.

5.2 Experimental configuration

5.2.1 Prototype description

The furnace consists of a composite of different refractory materials, which enclose a holding chamber and a heating chamber separated by a refractory layer. An array of electrical resistances is located in the heating chamber. The holding furnace was designed to kept aluminum in the range of 680-800 [°C]. Figure 5.1 shows photographs and a sectional view at the center plane of the furnace analyzed.

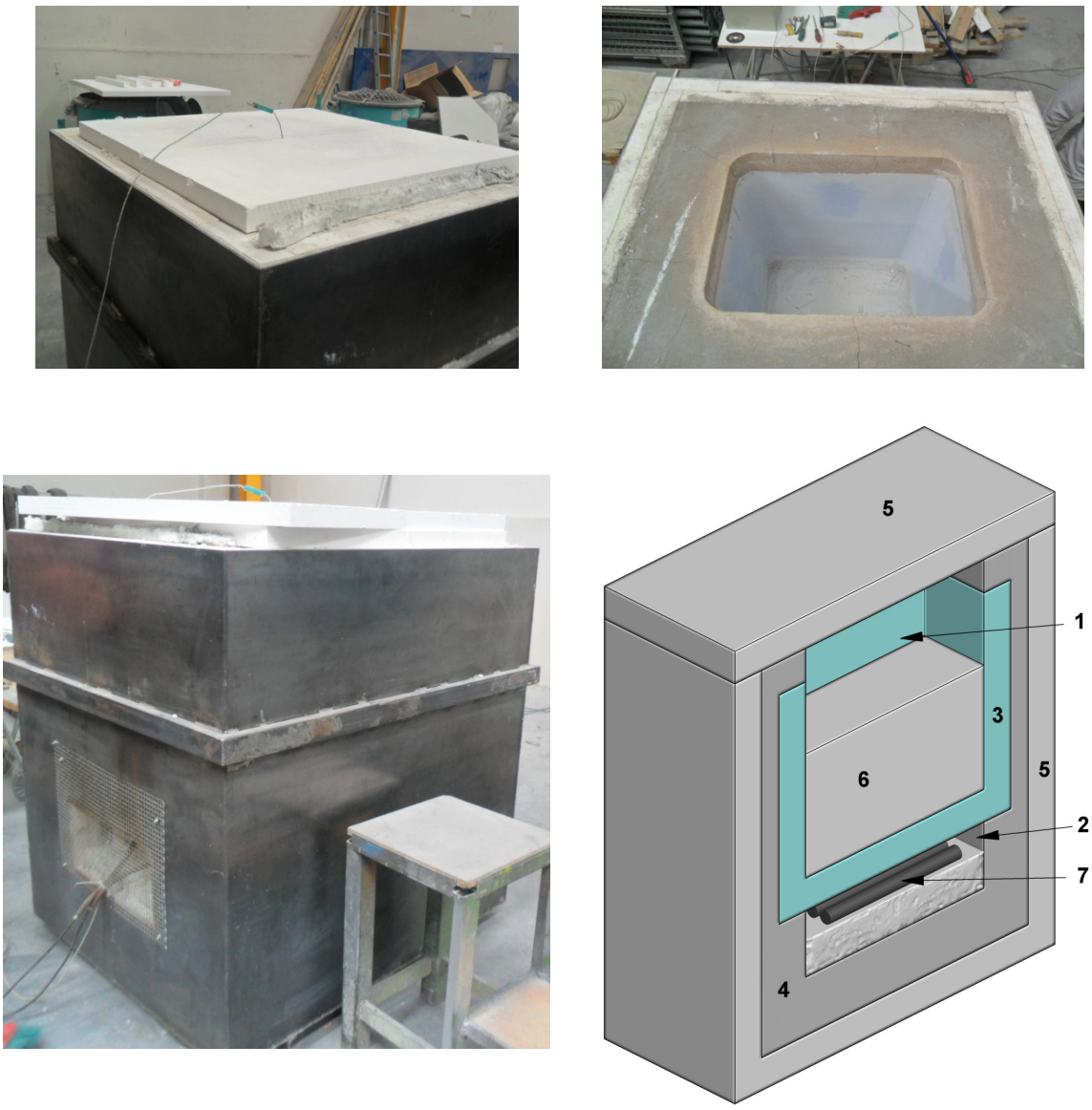

Figure 5.1. Photographs of the aluminum holding furnace and sectional view (1-holding chamber, 2-heating chamber, 3-layer of refractory material A, 4- layer of refractory material B, 5- layer of refractory material C, 6- aluminum load, 7- electrical resistances)

Additionally to the materials presented in Figure 5.1, two materials are located in the lateral walls of the furnace: a ceramic layer used as a supplementary insulation and a sheet of steel 1018 used as a protection for the refractory materials.

Figure 5.2 shows the array of electrical resistances used as the heating means.

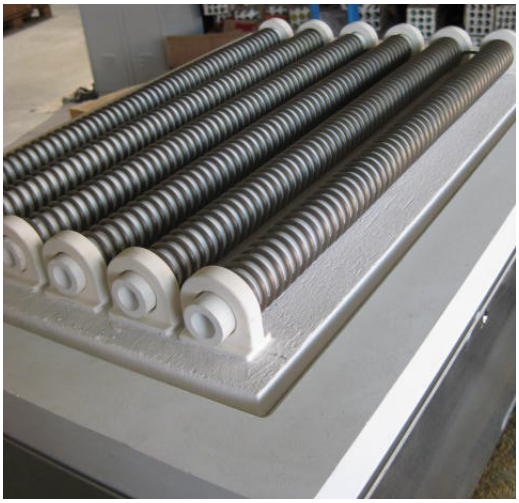

Figure 5.2. Photograph of the electrical resistances array

Experimental facilities and tests were provided and accomplished by Giesserei Instandsetzung Service 2003 S.L. (GIS 2003-Vilanova i la Geltrú, Barcelona) in the frame of the EDEFU project (EDEFU, 2010).

5.2.2 Dimensions and temperature measurements

The internal temperatures of the refractory walls have been measured through an array of thermocouples in four points at a height of 150 mm from the top of the furnace. An assembly made up of a thermocouple in a steel tube submerged in the molten metal is used to measure its temperature. The air temperatures inside the holding and heating cavities are measured through thermocouple probes installed in the respective chambers. The measurements of temperatures are taken under industrial conditions and have an estimated accuracy of ±2 ºC. Load weights and times can be considered exact in practical terms. Figure 5.3 shows the main dimensions of the furnace and the location of the temperature measurement points.

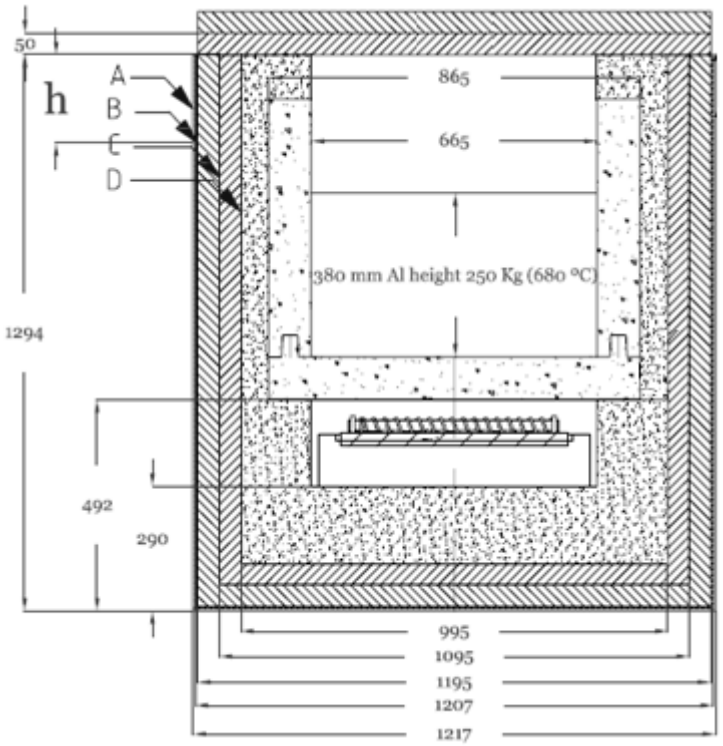

Figure 5.3. Dimensions of aluminum holding furnace (mm) and measurements points for the temperature (A-D) at a height h = 150 mm

5.2.3 Test protocol

The holding furnace is preheated by the electrical resistances until the refractory walls reach the operation temperature and the furnace becomes stable (12-15 days). The high temperatures of the refractory walls are used to maintaining the load above the melting point and avoid refractory damages due to cracking from thermal expansion. Molten aluminum is poured into the holding chamber and it is held for several hours. The power supply is a simple on-off control, which introduces a constant power until the resistances chamber reach a maximum operation temperature and then is turned off until a minimum operation temperature. This commutative power is employed in order to raise the refractory temperature and compensate the heat losses in the furnace.

5.3 MODEL DESCRIPTION

5.3.1 Assumptions and boundary conditions

Numerical simulation is undertaken with the commercial CFD code FLUENT. Pressure-velocity coupling is implemented by the SIMPLE algorithm, with the standard scheme for pressure interpolation. A first-order upwind scheme is adopted for spatial discretization. The criterion of numerical convergence by time step is to achieve a decrease of 1×10^{-3} in the absolute residuals of the continuity and momentum equations, and a decrease 1×10^{-6} in the absolute residual of the energy equation.

The load consisting in 250 kg of metal is assumed to fill the ladle uniformly from the bottom up to a specific height. The whole domain is closed: air infiltrations are neglected.

Air and molten aluminum move due to thermally induced density differences in the holding chamber. Corresponding Rayleigh numbers can be estimated as 8×10^{5} and 5×10^{7}, respectively. Since the first is relatively far to the critical value of 10^{9} usually given for external flows in air (Mills, 1992), whereas turbulence transition for liquid aluminum in confined spaces heating from all walls is not clear, laminar flow is considered for both sub-domains, which additionally reduces the computational resources required.

The treatment of the air in the resistances chamber is based in the purely diffusive transfer in the gas, with an augmented, effective thermal conductivity. Since details of the temperature distribution in the air of the resistances cavity are not relevant for the energy balance, this approach is used in order to save computational resources. The overall energy effect is suitably represented (see chapter 4-section 4.3.3.3). The fact that real heat transfer by convection and especially by radiation is more intense can be represented by an augmented thermal conductivity given by $k_{\text{eff}} = h_{eff} t_c$. Considering the resistances chamber as a box with an array of cylinders that represent the resistances, with a height equal to the distance between the electrical resistances and the top of the heating chamber (in this case: $t_c = 61\ mm$), and uniform surface temperatures of 1200 ºC

for the resistances and 800 ºC for the top and lateral walls of the resistance chamber, respectively, coefficients are estimated according to basic heat transfer calculations (Incropera and DeWitt, 1990). Results are $h_{conv} \approx$ 3.5 W/(m^{2}K), $h_{rad} \approx$ 231.7 W/(m^{2}K), $h_{eff} = h_{conv} + h_{rad} \approx$ 235.2 W/(m^{2}K), so that air conductivity is taken as k_{eff} = 14.35 W/(mK).

Heat losses from the external surface of the crucible to the surroundings are approximated as follows. The bottom is considered perfectly insulated. Lateral walls of the furnace are composed of two sheets of different materials: 1) A ceramic fiber layer, which is the final material in the refractory array. 2) A sheet of steel 1018. Both sheets have very small thickness in comparison with the other materials and thus would force an exaggerated grading of the mesh, which may lead to numerical convergence problems. In order to represent heat conduction in these small planar thicknesses without meshing the domains, a thin-wall model was used. In this model, a 1D heat conduction equation is solved to compute the thermal resistance imposed by the wall. The thermal resistance of the wall is $\Delta x/k$, where k is the conductivity of the wall material and Δx is the wall thickness. Heat transfer conditions and thermal circuit of the lateral walls are schematically represented in Figure 5.4.

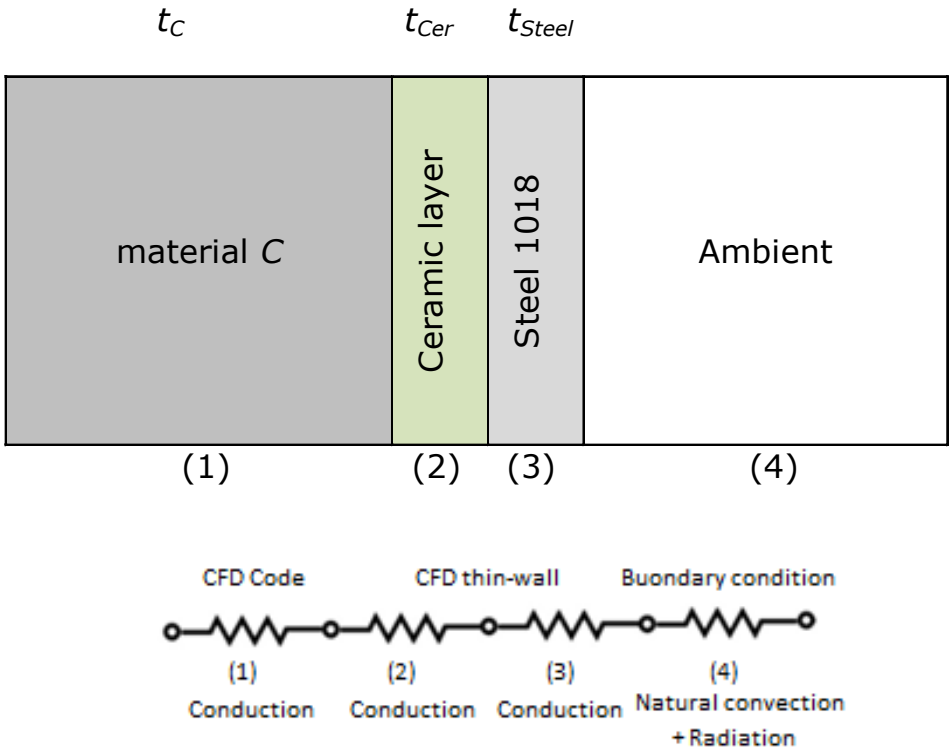

Figure 5.4. Heat transfer scheme and thermal circuit in the lateral walls of the crucible

Solving the equivalent circuit, the equivalent thermal conductivity for the ceramic and steel sheets is k_{eq} = 0.26 W/(mK). On the other hand, heat transfer by natural convection and radiation takes place. A constant, average heat transfer coefficient $h_{av} = h_{conv} + h_{rad}$ [W/(m^{2}K)] is estimated according to elementary heat transfer calculations (Incropera and DeWitt, 1990). For the convective coefficient h_{conv}, an empirical correlation for the ideal geometry of vertical walls is applied. Radiation is estimated through the formula giving the losses to a large (thus, black) radiative environment. Both coefficients depend on surface and ambient temperatures, assumed uniform and known. Values of 250ºC and 18ºC, respectively, are used, the former confirmed as representative of the typical average of numerical results for the surface temperature distribution. Total emissivity used is a typical value of 0.7 for non-polished surfaces. Calculation results in $h_{conv} \approx 7$ W/(m^{2}K), $h_{rad} \approx 11$ W/(m^{2}K), and thus $h_{av} \approx 18$ W/(m^{2}K).

Finally, the electrical resistances supplies a total constant input power (W_{input} = 11 kW) until the heating chamber reaches a temperature of 1000 ºC, then these are turned off until the temperature in the heating chamber drops to 995 ºC. The resistances are simplified as an array of cylinders. Since the internal temperature of the resistances is not of interest for the present simulations, the heat generation is imposed as a boundary condition in the cylinders faces; which is in fact the power input in the furnace: $w = W_{input}/NA_{res}$ = 28356.08 [W/m^2]. Where N is the number of resistances and A_{res} is the unitary volume.

The on-off control condition has been imposed in the resistances area by means of a User Defined Function (UDF) in FLUENT.

5.3.2 Geometry and materials

In order to reduce the computational cost and take advantage of the symmetry, only a quarter of the domain was simulated in a first approach. Since strong asymmetry was observed in the natural flow within the load, afterwards the full domain was simulated to compare the results obtained by both approaches. Figure 5.5 shows the geometries simulated for the cases of the quarter of domain and the full domain (translucent view),

that reproduce the refractory array of the real furnace. The air in the resistances chambers and holding chamber is not shown for clarity.

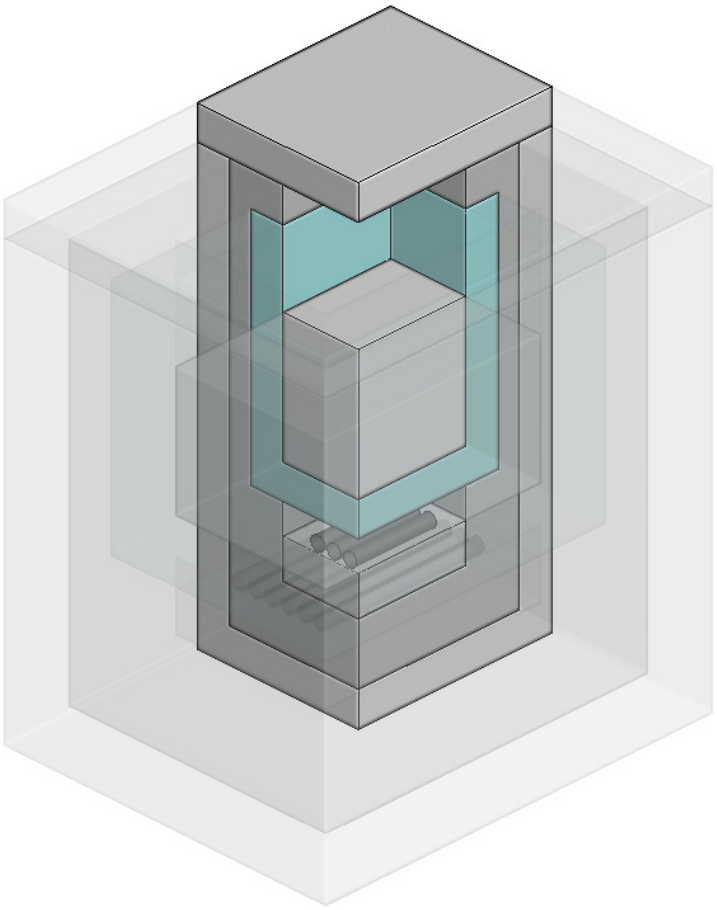

Figure 5.5. Geometry for the numerical simulations- Quarter of domain and full domain (translucent view)

The resistances used in the furnace are wire elements of the typical material "aluchrom". Table 5.1 shows the thermal properties for the solid parts in the furnace, while the thermo-physical properties of the aluminum load are summarized in Table 5.2.

Table 5.1: Thermal properties of solid parts

Material	Density kg/m^3	Specific heat (KJ/kg.K)	Thermal conductivity (W/m.K)
Refractory material A[a]	2563	0.690	8
Refractory material B[b,c]	1200	1.200	0.2
Refractory material C[b,d]	930	1.200	0.28
Ceramic layer[e]	160	1.088	0.143
Aluchrom[a,f]	7100	0.640	16
Steel 1018[g]	7800	0.489	50

[a] Goodfellow (2012); [b] Skamol (2010); [c] Dupré (2008); [d] Christy (2004); [e] Rath (2012); [f] Outokumpu (2008); [g] MatWeb (2012)

Table 5.2: Thermophysical properties of aluminum load

Density (kg/m^3)[a]	2700	T < 873 K
	-3.873T+5992	873 K < T < 933.15 K
	-0.3116T+2668	T > 933.15 K
Specific heat (kJ/kg.K)[b]	0.900	
Thermal conductivity (W/m.K)[b]	237	
Viscosity (kg/m.s)[a]	0.001	
Latent heat of fusion (kJ/kg)[b]	397	
Solidus Temperature (K)[c]	873	
Liquidus Temperature (K)[c]	933.15	

[a] Assael et al. (2006); [b] Brandt (1984); [c] Zeiger and Nielsen (2004)

5.3.3 Models

For the convective motion of the molten load and air filling up the holding chamber, the Navier Stokes equations corresponding to a fluid of variable density are solved, which takes into account buoyancy. Non-slip, or velocity continuity, is imposed on all interfaces. Energy conservation is solved in full domain, which is equivalent to a problem of heat conduction in solids and heat convection in air and liquid aluminum. The method used enforces temperature continuity and conservation of heat flux through interfaces. Due to the solidification potential of the molten aluminum, the enthalpy method is used in the load domain in order to detect phase change points. Thermal radiation is calculated for the air cavity by the S2S radiation model.

5.3.4 Meshing scheme

Due to the diverse complex phenomena involved, the implementation of the numerical simulations is very expensive in computational terms. Therefore, currently it is not feasible to carry out a grid convergence study, only a single mesh of 531150 cells and a single mesh of 2124600 cells are used for the approaches of quarter and full domain respectively. The whole mesh is structured except by the heating chamber that presents a complex geometry. Figure 5.6 shows the general grid and details of the heating chamber for the case of the quarter of domain; this mesh is reproduced in each symmetry plane for the full domain approach.

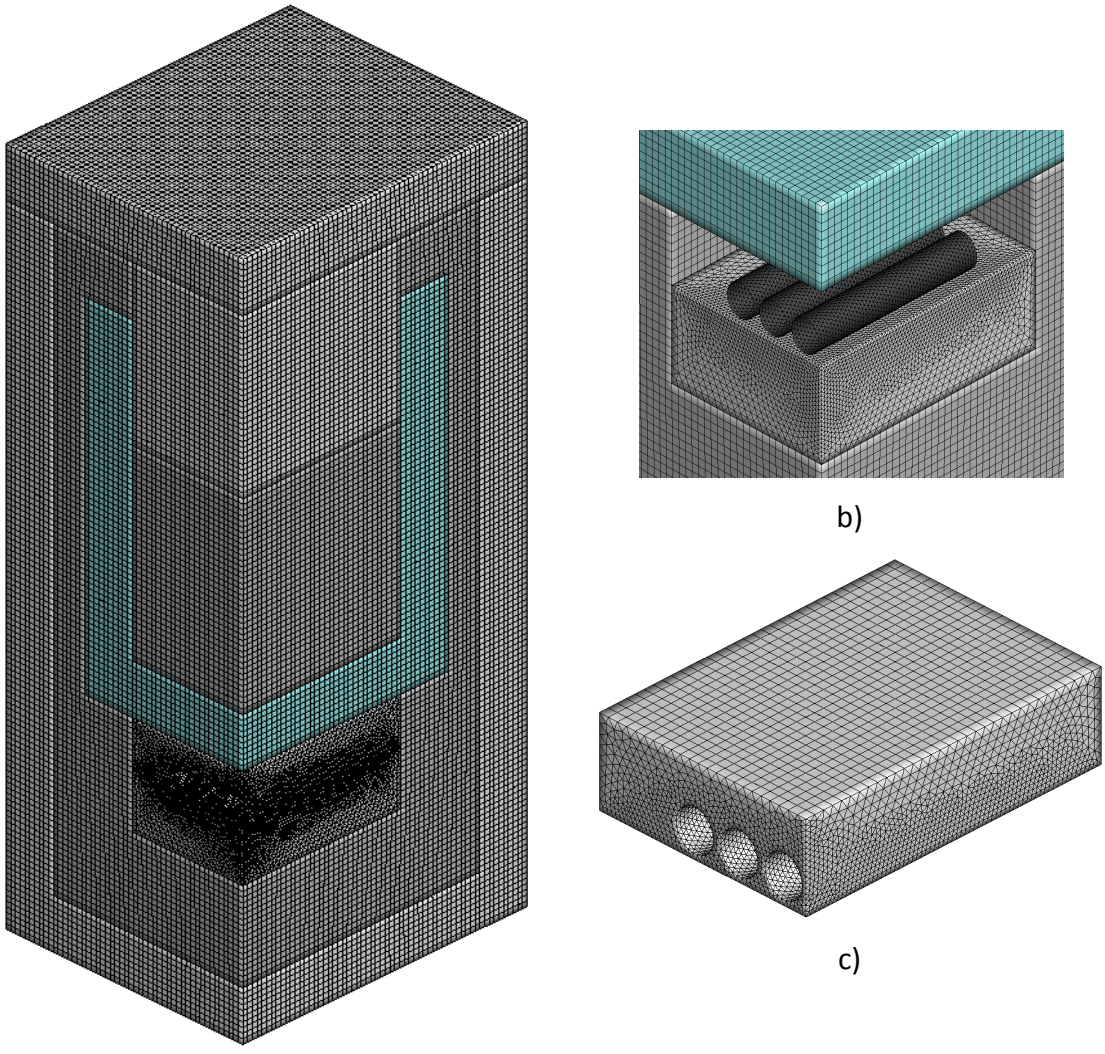

a)

b)

c)

Figure 5.6. Grid details-quarter of domain. a) General, b) Resistances, c) Air filling the resistances chamber

5.3.5 Numerical time step

In this work, iterative convergence at each time step is verified. Different values were tested, which resulted in that the required maximum value should be lower the complex the problem solved. The problem complexity increases by two factors: first, after the preheating process, a new material is added in the domain (molten load introduced after preheating process); second the on-off control prevents the use of a high value for the time step. Since in actual conditions the resistances are switched each 10 to 20 s approximately, the maximum time step used in the simulations is 3 s.

5.4 Results and discussion

5.4.1 Preheating stage

The process doesn't start from cold conditions but firstly the furnace is preheated by several days. In fact, this operation is the most important part of the process, since the high temperatures reached by the walls are used for the holding of molten aluminum. This imposes an initial internal energy content and a temperature distribution in the refractory material, and both should be taken into account. Therefore, firstly the preheating process is simulated, and its final state is taken as the initial one for the ensuing simulation of the holding of the molten load.

The holding chamber is filled with air in this part of the simulation; it is simulated along with all the others domains. The heat losses in walls and the heat input from the electrical resistances are taken into account by the boundary conditions defined before. The preheating process is accomplished until the furnace temperature becomes stable. Figure 5.7 shows the temperature profile in the furnace estimated in the simulations of the quarter and full domain for the preheating stage.

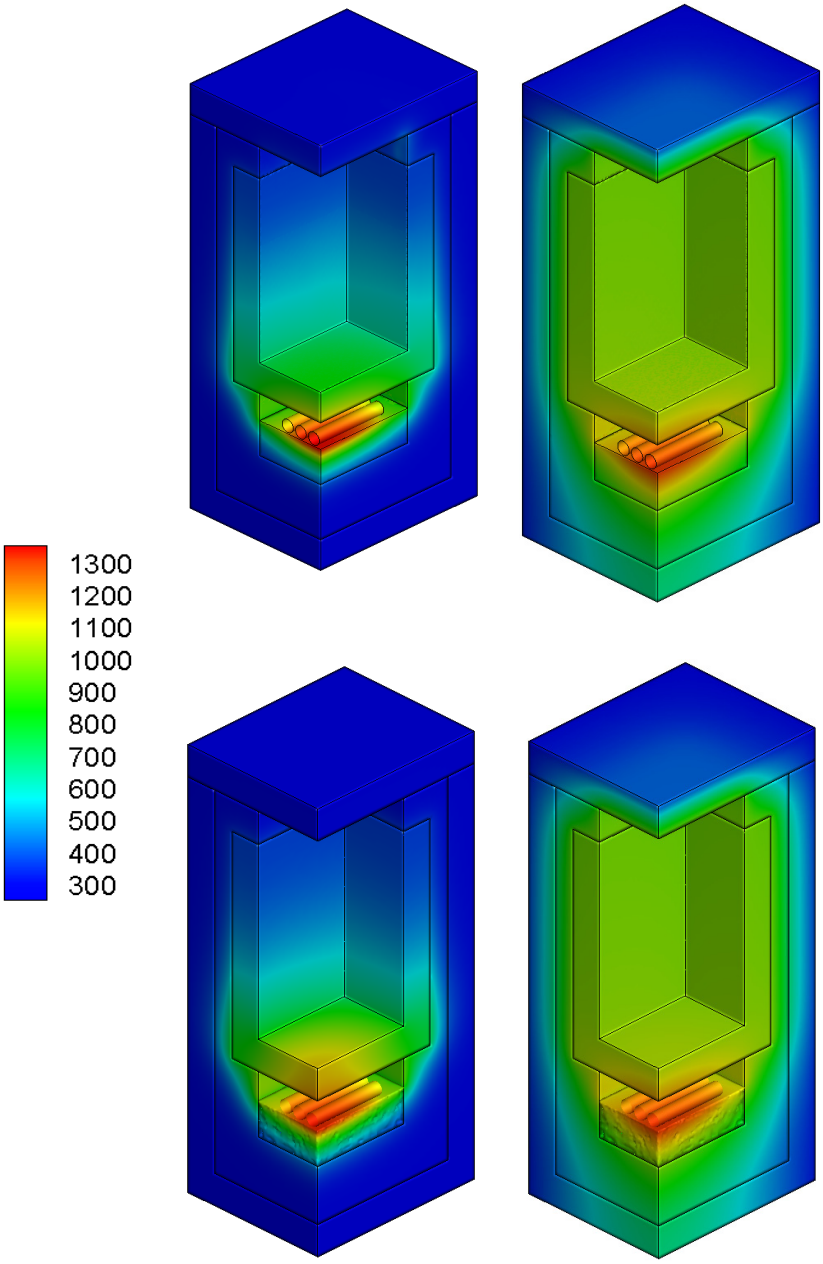

Figure 5.7. Temperature for preheating stage [K]. Up: quarter of domain. Down: full domain

5.4.2 Temperatures - holding process

After a stable solution from the preheating stage is obtained, the simulations are carried out for the holding process. In the real facilities, a load of 250 kg of aluminum is poured into the holding chamber in liquid state at 750 ºC. Then, the molten load is maintained

until the system achieves steady state. These conditions are reproduced in the numerical simulation. Results of the simulations show that the holding furnace can keep of the molten load at target temperature. Figure 5.8 shows the temperatures predicted by the numerical approaches in the furnace and load for the holding process.

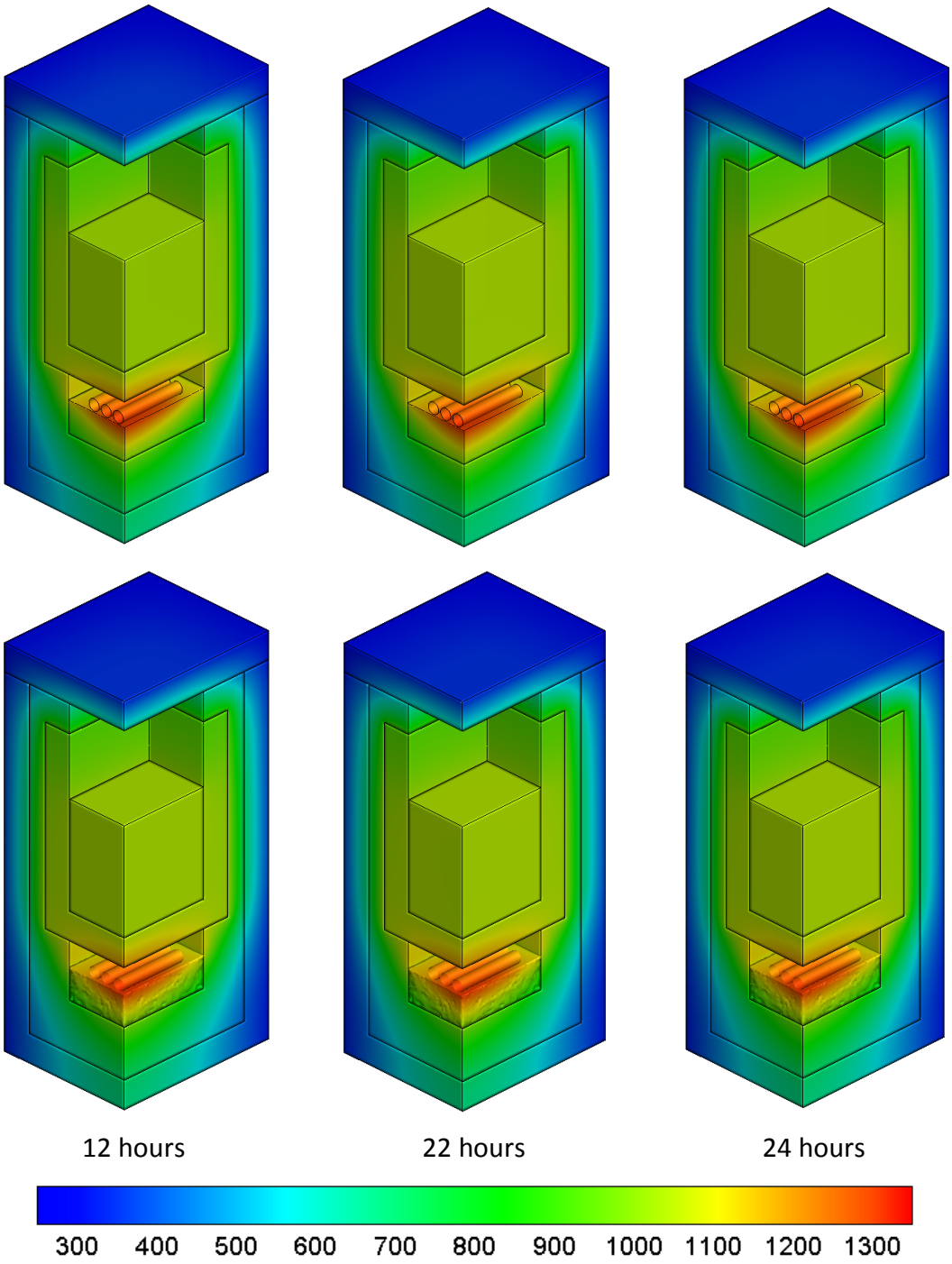

Figure 5.8. Temperature for holding stage [K]. Up: quarter of domain. Down: full domain

Figure 5.9 shows a comparison between the numerical predictions and measurements of the temperature profile in the walls; in this figure zero wall thickness indicates the internal wall and increases through the external refractory walls.

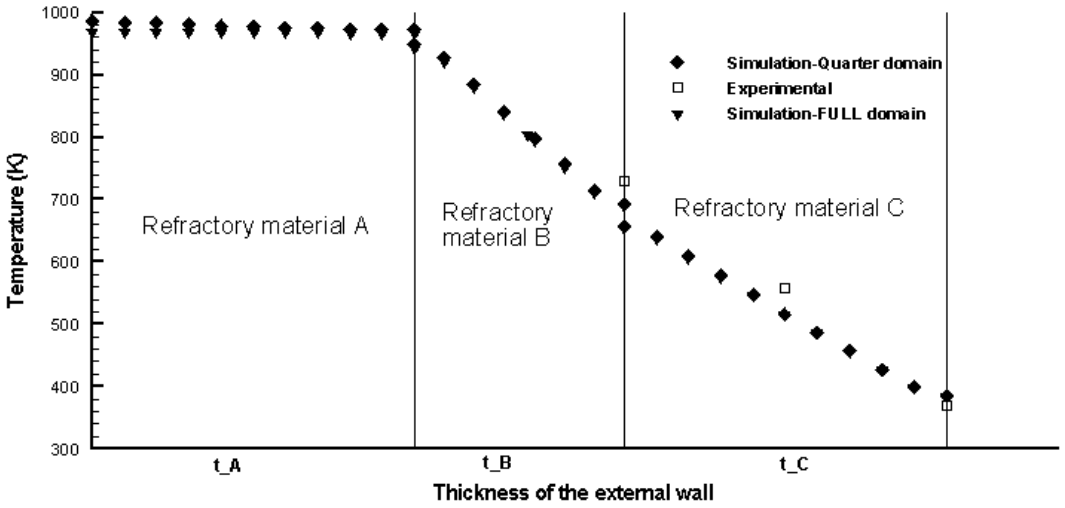

Figure 5.9. Wall temperature profile

Figure 5.7, Figure 5.8 and Figure 5.9 show the great similarities in temperature estimates for quarter and full domains approaches. As it is shown in Figure 5.8, the temperatures in the load are very homogeneous; in fact, the difference between the maximum and minimum temperatures is always less than 5 ºC. The temperature difference between holding and resistance chambers is 200 ºC. According to the experimental temperature measurements shown in Figure 5.9, the process was simulated within a reasonable agreement with real conditions considering the complexity of the simulation. Even though the low variation in temperature of the load and the almost constant condition of the refractory parts, it was not possible to obtain a steady state solution for the molten load.

5.4.3 Energy balance

The holding process is accomplished in almost steady state conditions; therefore the energy balance doesn't include changes in the internal energies in internal parts (refractories, load, air in cavities). The energy balance reduces to the statement that

estimated input thermal energy plus equals heat losses to ambient. For the two cases computed, the distribution of the losses is divided in approximately 83% by the external lateral walls and in approximately 17% by the top of furnace

5.4.4 Convection effects

The homogeneity of the temperatures presented in this device is an effect highly desirable in aluminum holding furnaces (Zhou et al., 2010); it is mainly produced due to the convection effects (Tripathi et al., 2012). Figure 5.10 shows the vertical velocity profiles and velocity vectors for the molten aluminum. Figure 5.11 shows the variation of several iso-surfaces of vertical velocity for the holding process.

Figure 5.10 and Figure 5.11 show the unsteady behavior of the movement in the molten load. The quarter of domain approach predicts higher velocities than the full domain, off course with a symmetrical pattern. On the other hand, the full domain approach predicts a pattern highly three dimensional. Therefore, even though the similarity in the thermal performance estimated in both approaches, the internal flow is strongly limited by the symmetric simplifications. In order to determine the features of the flow, four control points are located on a plane at half height of the load: 1) center line of the furnace, 2) center of thin wall 3) corner of the furnace; 4) center of the thick wall. In each, Z-velocity (vertical velocity) and temperature are continuously registered for a representative simulation time. Figure 5.12 shows the location of these control points in the quarter of domain; these same points are used for the full domain with a comparison purpose.

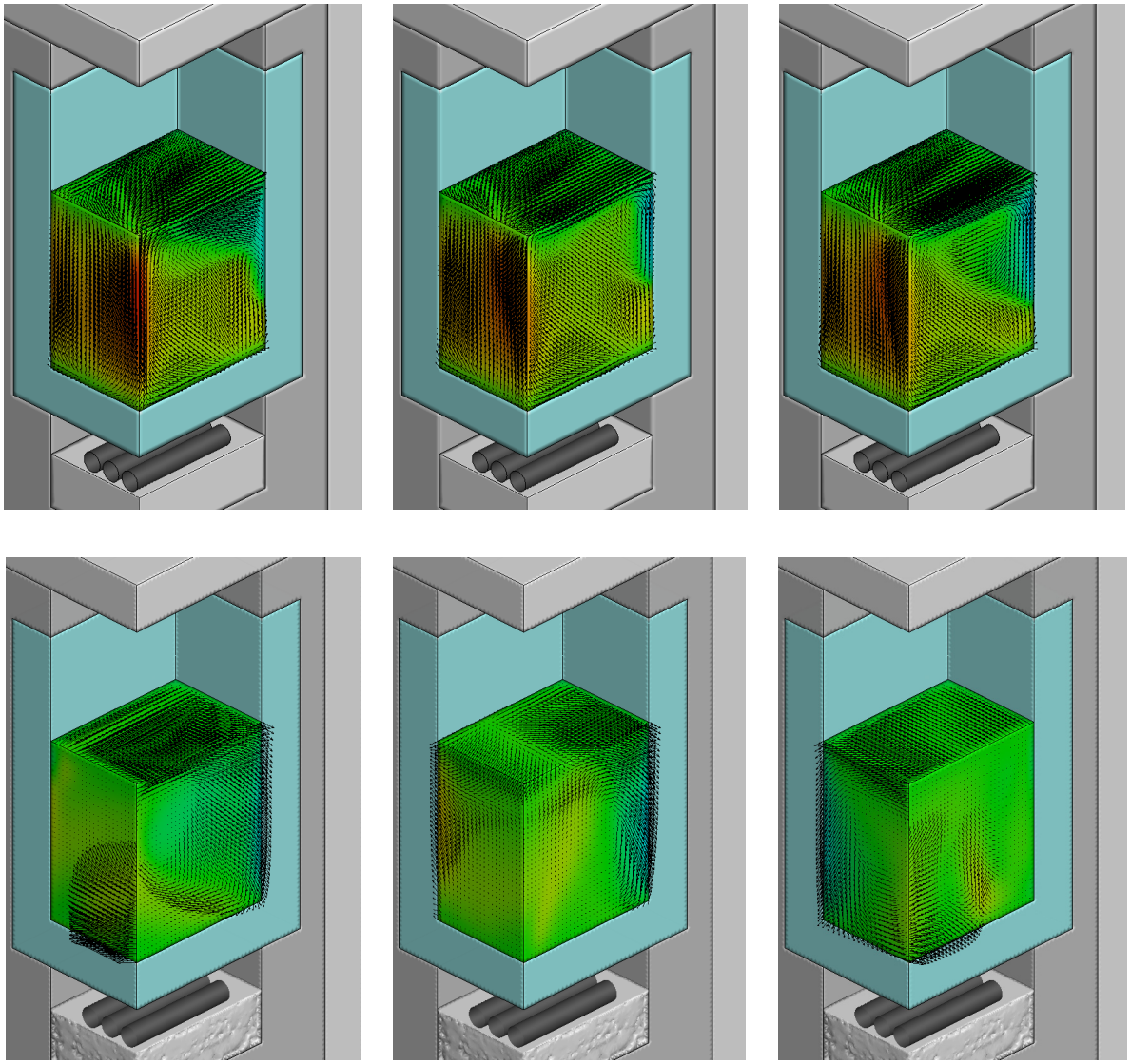

Figure 5.10. Vertical velocity profile [m/s] and velocity vector for the molten aluminum.

Up: quarter of domain. Down: full domain

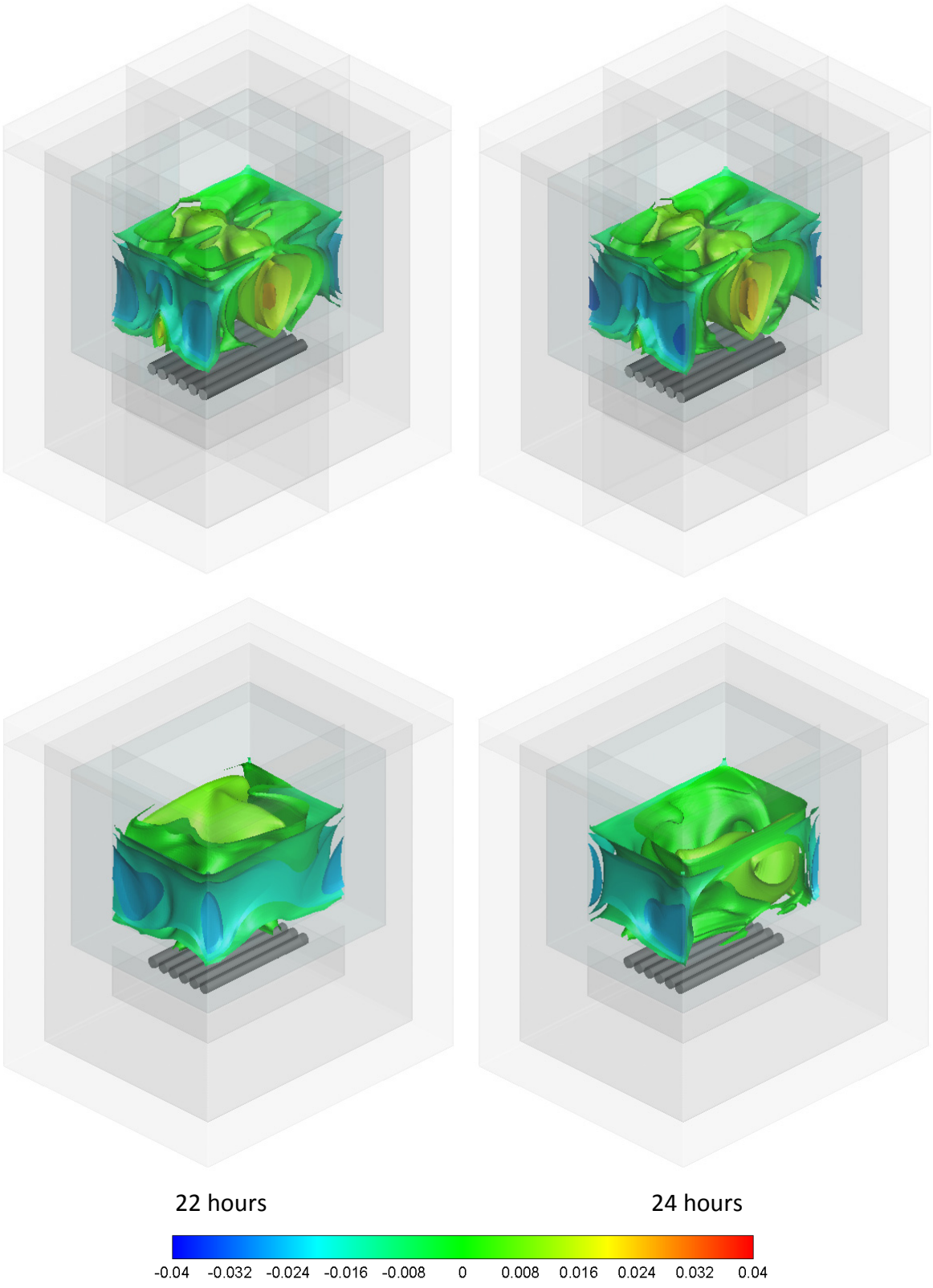

Figure 5.11. Iso-surfaces of vertical velocity for the molten aluminum. Up: quarter of domain. Down: full domain

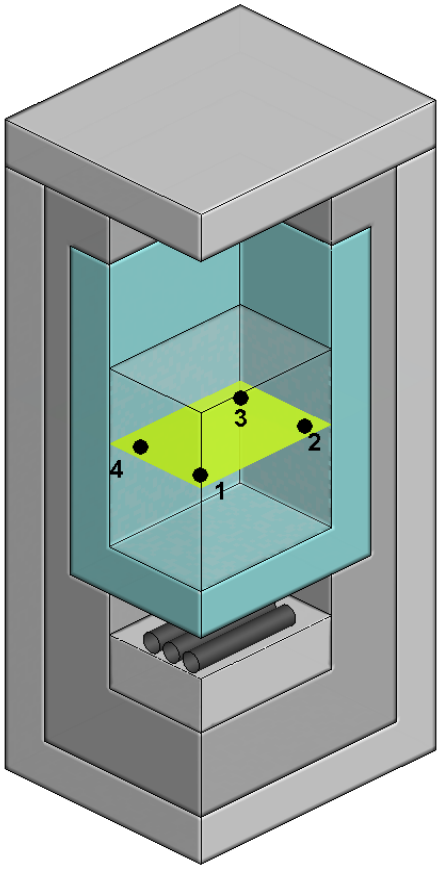

Figure 5.12. Location of control points for the molten load

Figure 5.13 and Figure 5.14 show the z-velocities and temperatures registered respectively, in the control points for both the quarter and full domain approaches.

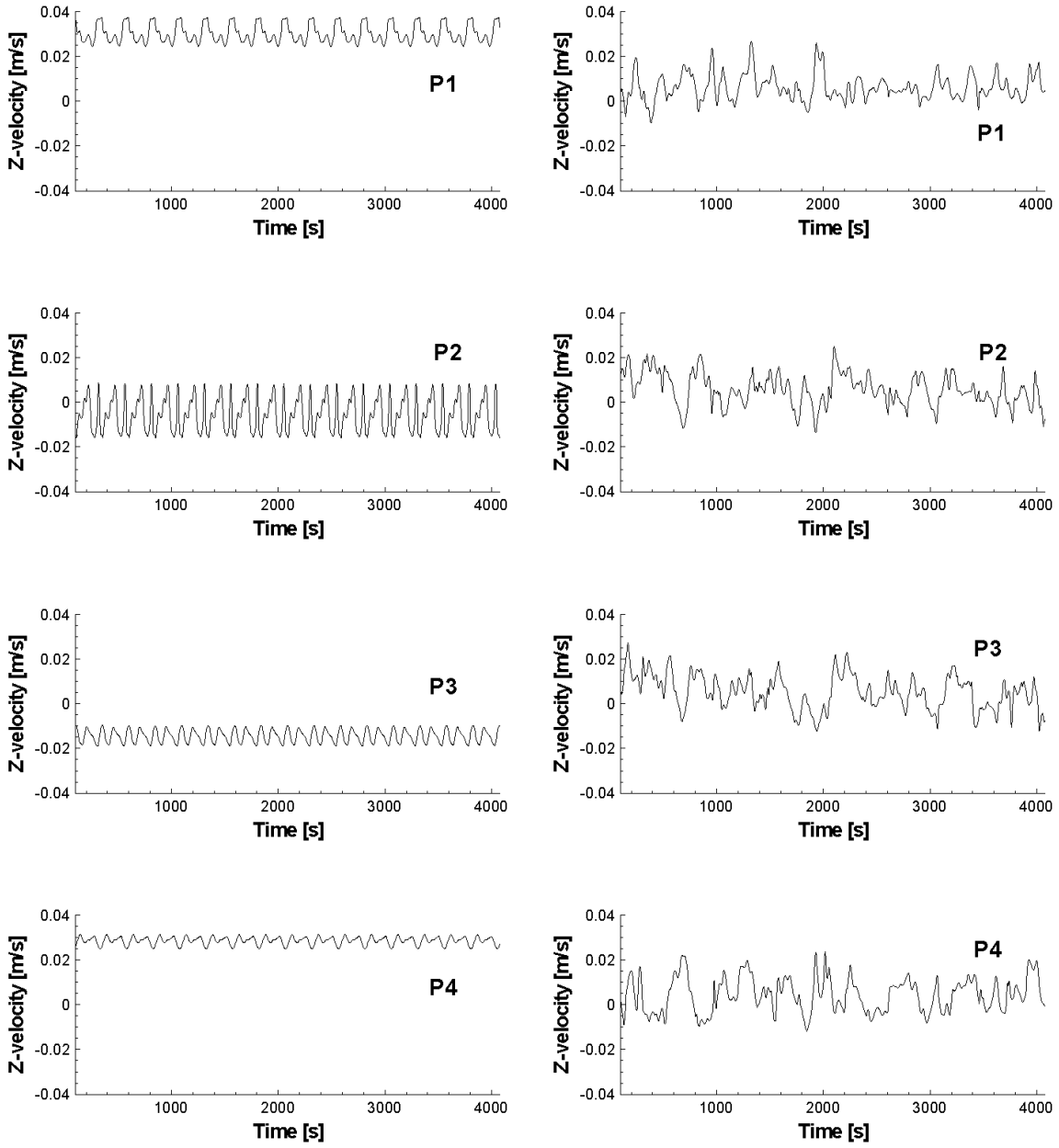

Figure 5.13. Z-velocities registered (m/s) in control points P1-P4. Left: quarter of domain. Right: full domain

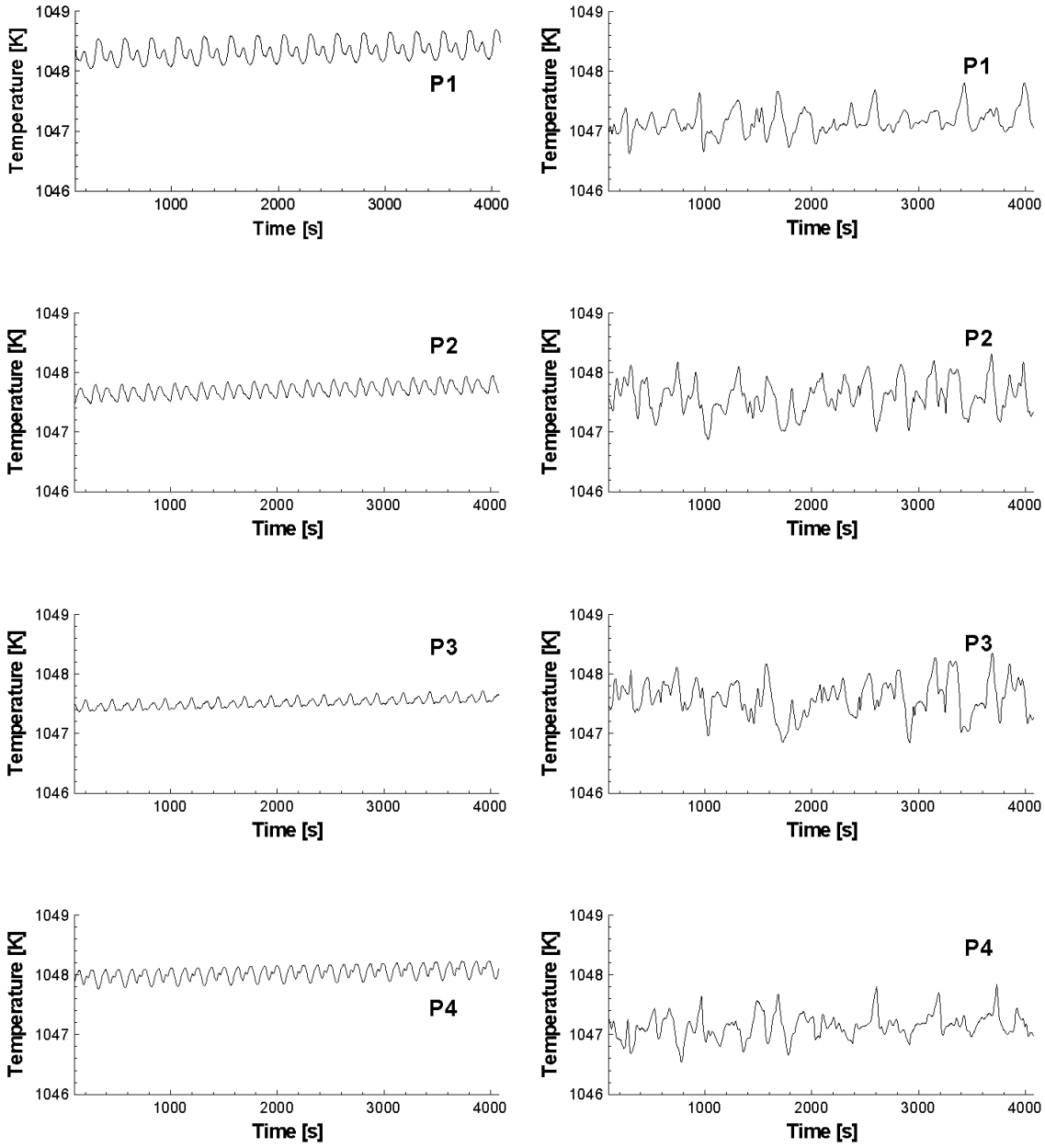

Figure 5.14. Temperatures registered (K) in control points P1-P4. Left: quarter of domain. Right: full domain

A pure periodic behavior is predicted by the simulations of the quarter of domain in each control point, whereas for the full domain also an oscillatory behavior is predicted, but in this case the signal seems not to be purely periodical. Velocities in the molten load vary significantly between both simulations. Load temperatures estimated by the quarter of domain approach are slightly higher than that of the full domain approach; nevertheless the difference can be neglected in practical terms for industrial

applications. In order to obtain the dominant frequencies in the flow of the molten load, the Fast Fourier Transform (FFT) (Brigham, 1988) is applied to the registers in time of the Z-velocity and temperatures for each control point. They are shown in Figure 5.15 and Figure 5.16 respectively.

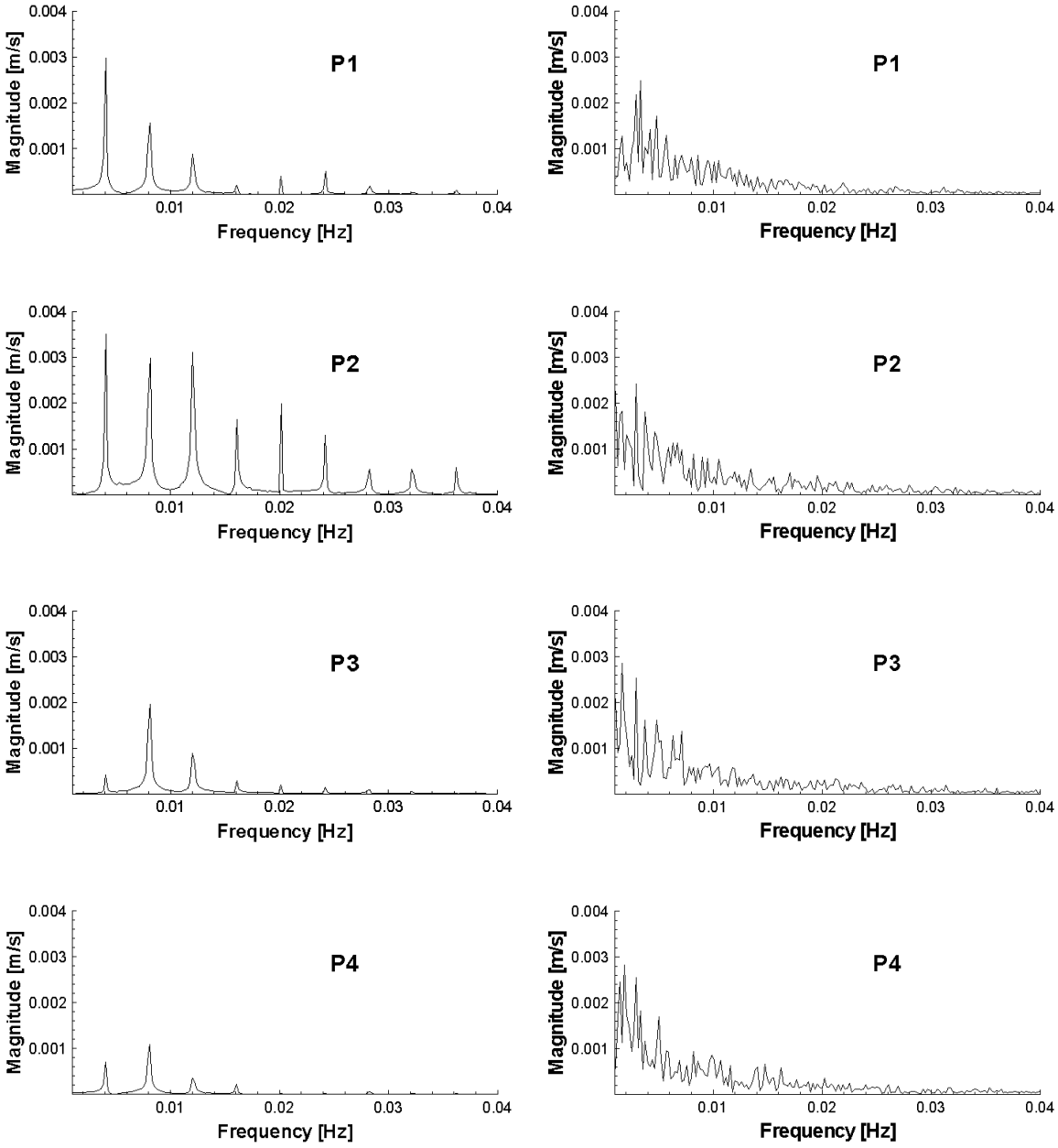

Figure 5.15. FFT for Z-velocities registered in control points P1-P4. Left: quarter of domain. Right: full domain

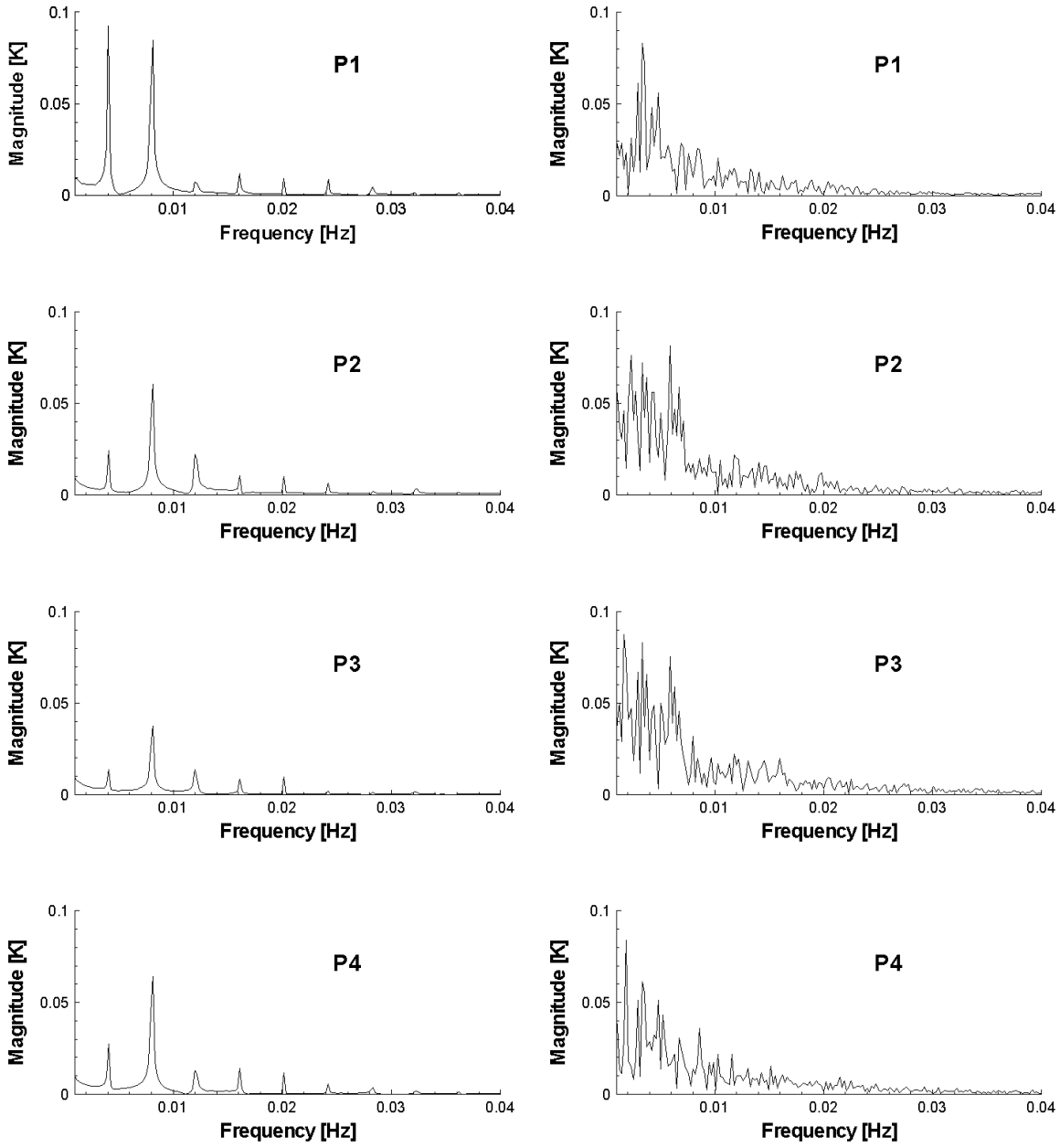

Figure 5.16. FFT for Temperatures registered in control points P1-P4. Left: quarter of domain. Right: full domain

In accordance with previous observations, it is shown that the simulation of a quarter of domain tends to produce discrete frequency peaks, whereas the spectra are more continuous and rich when the full domain is considered. The oscillatory responses are not related to the on-off control mode that operates at much higher frequency (ca. 0.05-0.1 Hz).

Behaviors presented in both approaches are usually observed in natural-convection systems as a result of their intrinsic instability. The general theory of flows induced by natural convection is presented in classic literature as the work of Gebhart (1988). It has been establishes that in natural convective problems the flow remains steady until a critical Rayleigh. When Rayleigh number is increased several transitional appear, from steady, including periodic, seudo-periodic, chaotic and finally turbulent behavior. The transition of each stage is conditioned additionally by the fluid characteristics (Prandtl number).

At small Pr, the flow has been observed to be unsteady at very low Rayleigh numbers. Since the accurate measurements of velocities and temperature are very difficult for liquid metals, the transition of the flow regimes are not yet comprehensive covered. Due to the advantages of the measurements at temperatures close to the ambient, some studies have been developed for mercury and gallium (Pr=0.02-0.025) in horizontal enclosures, in which a turbulent regimen is developed above $Ra > 2 \times 10^4$. On the other hand, the transition from laminar to turbulent regimes is predicted to arise at lower Ra when Pr is low (Gebhart, 1988).

The aim of the simulations presented is the use of the models in industrial applications; these have included a practical approach of the overall system, i.e. conjugated problem with refractory walls, heating means, heat losses, etc. Literature of flows induced by natural convection considers simplified domains in order to use smaller mesh sizes and achieve Direct Numerical Simulation (DNS) conditions, which is not the objective of this work. According to the spatial resolution for a DNS of Grötzbach (1983), the grid size for the load domain under the holding furnace conditions ($Pr \approx 0.003$ and $Ra \approx 5 \times 10^7$), should be approximately of 1000x1750x1223 elements instead of the 38x66x46 elements used here. Considering that the simulations of the holding furnace for the full domain approach has required 6 months of wall clock time, the recommended range for the spatial discretization (Chillà and Schumacher, 2012, Grötzbach, 1983) in DNS to solve all the flows scales is prohibitively expensive for the current purposes.

It is thus clear that flow results of our simulation don't constitute a proper solution of the problem, since we have assumed unsteady (laminar) flow without enough spatial resolution to replicate the details. However, thermal results, as we have seen, appear perfectly reliable and useful for industrial application. On the other hand, the model can predict chaotic behavior, even for the full domain in a range of frequencies (no discrete frequencies), which is very curious and points to the field of Rayleigh-Benard flows. In this regard, some authors have presented their works in convection problems in liquid metals, especially for mercury and gallium. Verzicco and Camussi (1997) present 3D numerical simulations of the transitions from the onset of convection to fully developed turbulence flow, in a cylindrical cell and in mercury; they found that the flow remained steady up to Ra $\approx 2.11 \times 10^4$ when an oscillatory instability is observed. As the Rayleigh number is further increased, this oscillatory regime evolves towards a more complex state with more frequencies in the time oscillations (Ra $\approx 2.75 \times 10^4$ - 3×10^4) and finally the turbulent state is achieved (Ra $\approx 3.75 \times 10^4$), where the formation of more subharmonics tends to fill the spectrum. These behaviors coincide with our predictions of periodic and chaotic movement obtained in the quarter and full domain approaches of the holding furnace, respectively. These results are obtained in the present work even though both simulations have the same Rayleigh number. This is difficult to explain, although it points to the difference in the aspect ratios (length/height), since the transition in flows also depends on the geometry of the fluid vessel, as is pointed out by Crunkleton et al. (2006), who presented numerical simulations of the transition from steady to oscillatory flow for a very low Prandtl number fluid (Pr = 0.008) in rectangular enclosures with different aspect ratios; they found that the flows in cavities with higher heights are more stables than that in geometries with high aspect ratios. This conclusion is in agreement with the results obtained here and it is supported by several authors, such as Puits et al. (2013) or Bailon-Cuba et al. (2010) in analysis with air, experimental and numerical respectively. Hof et al. (2004) present an experimental and numerical simulation of the oscillatory convection in molten gallium for a rectangular cavity, where the metal is heated from lateral walls; they obtain oscillatory behavior for very low Rayleigh numbers. On the other hand, Lee and Park (2012) have presented a 2D numerical analysis on natural convection in an enclosure having a vertical thermal

gradient with a square insulator inside; with this configuration they obtained in a fluid with Pr = 0.01 periodic and pseudo periodic behaviors with Ra = 10^5 and Ra = 10^6 respectively. These studies are also simplified domains compared with the present holding furnace; but they indicate that a chaotic behavior is expected with the current conditions. In this sense, the assumption of a symmetry boundary condition in this kind of applications prevents the correct prediction of the convection effects due to suppression of three dimensional expansions.

A clear future work would be to perform simulations with a turbulence model in order to compare the results with the current approach. Our simulations make perfectly clear that pulsating and chaotic flow can be numerically generated for molecular transport. Then, perhaps more details would appear if such an URANS scheme is implemented. Nevertheless, in practical terms, the homogeneity of the temperature inside the load makes the current approaches good enough for industrial purposes. In addition, the currently measurement techniques applied to aluminum furnaces, don't allow a detailed characterization of the internal flow. Nevertheless, as it was presented in chapter 4, it is necessary to take into account the movement of the load for the thermal simulation in furnaces, in order to prevent over estimations of temperatures.

6. Summary and conclusions

Numerical studies of the thermal performance of two different furnaces have been completed: 1) a new prototype of aluminum melting furnace; 2) a new prototype of aluminum holding furnace. These devices are a key factor in secondary aluminum production. Models used takes into account heat conduction in solid parts, convection in air and molten aluminum, interactions between gas-liquid-solid zones, phase change of the load and radiation heat transfer. With the objective to develop a calculating tool to assist in the design and scaling-up of industrial furnaces, several calculation strategies are tested concerning their computational economy and their accuracy in computing different key parameters. Estimations of temperatures in furnaces are compared with experimental measurements taken in real prototypes in typical operation cycles. The models employed show the capability to estimate the most important parameters in the operations of the furnaces; many of them are difficult to obtain with the current measurement techniques, e.g. the melting rate (melting furnace), power utilization, load and refractory temperatures and their time evolution, flow patterns in the molten bath and distribution of heat losses. Furthermore, results obtained in this work present the potential of numerical approaches, to support the experimental procedures to understand the different phenomena involved in melting and holding furnaces. The predicted values appear to be satisfactory considering the complexity of the simulations.

6.1 Melting furnace

Numerical simulations of a new prototype of aluminum melting furnace have been discussed in detail, including the assumptions taken into account, the methodology

followed in the numerical analysis and results. Taking advantage of the symmetry of the furnace, the models have been simplified to a 2D axisymmetric domain.

In order to determine the reduction in both computational expense and accuracy of the simulations, five computational cases using successively simplified models have been studied to simulate the losses from the load to the interior cavity of the furnace by radiation and convection. Case 1: thermal radiation modeled with the S2S radiation model and air convection fully modeled. Case 2: radiation no modeled and air convection fully modeled. Case 3: purely diffusive transfer in the gas, with an augmented, effective thermal conductivity. Case 4: air in cavity not modeled. Case 5: air in cavity not modeled and load heated by pure conduction.

Cases 1-4, show the same behavior in the prediction of the melting rate and their differences are negligible. Nevertheless, cases 3 and 4 cannot predict the full convection effects shown by cases 1 and 2. Predictions of the temperature for the domain are similar for the cases 1 to 4. All those results seem very reasonable and in agreement with empirical observations and analytical models. Results obtained by the pure conduction approach (case 5) show that in industrial applications, the simplification of no dependency with temperature for the density leads to overestimates in temperature, and thus to unrealistic results.

Case 1 uses 1.6 times of the computational resources than case 2; case 2 uses 2.25 times of the computational resources than the case 3; case 3 uses 27.52 times of the computational resources than case 4; finally, case 4 uses 21.8 times of the computational resources than the case 5. With the assumptions taken in cases 3 and 4, it is possible to perform initial estimates of the process (e.g. melting time and molten temperature), but neglecting the full convection effects between the air and load, that may be important for a comprehensive analysis. The main drawback of the most comprehensive approach (case 1) is their high computational cost, but it can be compensated with the current computer resources, which allow the analysis of a case in few days.

The computational advantage of simplified models (cases 2-5 vs. case 1) must be considered for each specific application. Difference in computational times is very significant, so that purpose and number of simulations required should be always considered. Predictions and cost of the simplified simulations have been discussed and compared, which could assist in this respect.

6.2 Holding furnace

Three dimensional unsteady state simulations have been presented with the purpose to estimate the thermal behavior in a holding furnace heated by an electrical resistances system. Assumptions, followed methodology and a discussion of the main results obtained have been presented at length.

As a first approach, the symmetry of the geometry has been used to reduce the computational resources and only a quarter of domain has been initially simulated. Nevertheless, the predicted velocities for the flow in the molten load suggest that the patterns induced by the convection effects have a three dimensional behavior. For this reason a new simulation with the full domain has been performed.

The numerical simulations show that the holding furnace can keep the temperature of the molten load above the melting point, in a very homogeneous temperature distribution in the load and in an almost constant operational condition. The temperatures predicted seem very reasonable and agree well with empirical observations taken in a real prototype for a typical operation cycle.

Temperature distribution and energy fluxes predicted by the two cases computed are almost the same. Nevertheless, the flow patterns in molten aluminum differ greatly between both approaches. Benchmarking of the holding furnace with simplified problems of natural convection, allows to pointing out that the expected flow pattern in the molten load, should looks like that obtained with the full domain; therefore, a main conclusion is that the symmetry condition prevents the full develop of the flow patterns in furnaces with quasi-steady state heating systems. The works of flows induced by

natural convection considers simplified domains in order to use smaller mesh sizes and achieve DNS conditions, but the requirements to solve all the turbulence scales is prohibitively expensive for the current industrial purposes.

Even for the homogeneous temperatures presented in the furnace, the models show the capacity to estimate complex patterns of movement inside the molten load caused by the convection effects. These behaviors are usually observed in natural convection systems as a result of their intrinsic instability. Many publications have been presented in metals with fusion points close to ambient temperature, simplified geometries and controlled boundary conditions, but, due to the difficulty in measurements in industrial aluminum furnaces, currently it is not feasible a detailed characterization of the internal flow, and there is no bibliographical reference about this subject for this kind of devices.

In practical terms, the homogeneity of the temperature inside the load makes that the current approaches are good enough for industrial purposes. Convection effect does not appear to have a major impact on the global energy balance, but it is necessary take into account the movement in the molten load to avoid over prediction in the temperature. Likewise, the unstable patterns preclude obtaining a steady state solution.

6.3 Perspectives for future work

Considering the results of the present thesis, a natural next step is the validation of the methodologies employed with comprehensive experimental data. Nevertheless, a rigorous experimental validation for the numerical simulations of melting and holding furnaces must include the accurate measurements of velocities and temperatures in the molten load, but these kinds of experimental rigs are not currently available for metal industrial furnaces and of course, it exceed the scopes and objectives of the present work or derived research lines.

Simplifications considered for this thesis must be reduced as a future work. Firstly, more complex models will be included in the solution, i.e. turbulence models, three dimensional and not simplified geometries, or more refined grids. These problems will

be solved as the computational resources increase. Secondly, several phenomena can be incorporated for a more complete analysis, e.g. chemical reactions for interactions with alloy materials and oxidation of the load, the influence of the scrap sources (composition, shape and size) and evolution of metallurgical effects; to this end, several submodels must be coupled within the CFD solution. Finally, a combination of different physics can be added to the present solution; as an example, currently the volume expansion of the metal is typically solved with the VOF method, but this technique is very difficult to implement in conjugated problems and it is not available in commercial solvers; multiphysics codes present a growing opportunity to compute this and other kind of phenomena combinations.

Actually, future work will be mainly centered on capture the essential information required in industrial furnaces. The compromise between the economy of the models and the quality of the prediction must be judiciously analyzed for any particular application. While the computational resources and the commercial codes become enough comprehensive, fast and accessible to not qualified personnel, the numerical simulations will be used in order to develop simplified reduced models, which allow a quick evaluation of key parameters in industrial furnaces.

7. Resumen y conclusiones

Estudios numéricos de desempeño térmico para dos diferentes hornos han sido llevados a cavo: 1) un nuevo prototipo de horno de fundición de aluminio; 2) un nuevo prototipo de horno de mantenimiento de aluminio. Estos son dispositivos clave en la producción de aluminio secundario. Los modelos utilizados tienen en cuenta la conducción de calor en las partes sólidas, la convección en el aire y el aluminio fundido, las interacciones entre las zonas gas-líquido-sólido, el cambio de fase de la carga y la transferencia de calor por radiación. Con el objetivo de desarrollar una herramienta de cálculo para ayudar en el diseño y escalamiento de hornos industriales, se han evaluado diferentes estrategias de cómputo en relación a la economía computacional y la precisión en el cálculo de diferentes parámetros clave. Las estimaciones de las temperaturas en los hornos se comparan con mediciones experimentales realizadas en prototipos reales en ciclos de operación típicos. Los modelos empleados muestran la capacidad de estimar los parámetros más importantes en el funcionamiento de los hornos; muchos de ellos son difíciles de obtener con las técnicas actuales de medición, por ejemplo, la velocidad de fusión (horno de fusión), la utilización de energía, temperaturas de la carga y refractarios y su evolución en el tiempo, patrones de flujo en el baño y la distribución de las pérdidas de calor. Además, los resultados obtenidos en este trabajo presentan el potencial de los métodos numéricos, para ayudar a los procedimientos experimentales en la comprensión de los diferentes fenómenos involucrados en la operación de hornos de fusión y mantenimiento. Los valores estimados se ven satisfactorios teniendo en cuenta la complejidad de las simulaciones.

7.1 Horno de fundición

Se ha discutido en detalle las simulaciones numéricas de un nuevo prototipo de horno de fusión de aluminio, incluyendo las suposiciones realizadas, la metodología seguida en el análisis numérico y los resultados. Utilizando la simetría del horno, los modelos se han simplificado a un dominio axisimétrico 2D.

Con el fin de determinar la reducción tanto en consumo computacional y exactitud de las simulaciones, se han estudiado cinco casos computacionales utilizando modelos sucesivamente simplificados, para simular las pérdidas de la carga a la cavidad interior del horno por radiación y convección. Caso 1: radiación térmica modelada con el modelo de radiación S2S y convección de aire totalmente modelada. Caso 2: radiación no modelada y convección de aire totalmente modelada. Caso 3: transferencia puramente difusiva en el gas, con una aumentada conductividad térmica efectiva. Caso 4: aire en la cavidad no modelado. Caso 5: aire en la cavidad no modelado y calentamiento de la carga por conducción pura.

Los casos 1-4, muestran el mismo comportamiento en la predicción de la velocidad de fusión y sus diferencias son insignificantes. Sin embargo, los casos 3 y 4 no pueden predecir los efectos de convección completos mostrados por los casos 1 y 2. Las predicciones de la temperatura para el dominio son similares para los casos 1 a 4. Estos resultados parecen razonables y están de acuerdo con las observaciones empíricas y modelos analíticos. Los resultados obtenidos por el enfoque de conducción pura (caso 5), muestran que en aplicaciones industriales, la simplificación de ninguna dependencia con la temperatura para la densidad, conduce a una sobreestimación de la temperatura, y por lo tanto a resultados poco realistas.

El caso 1 utiliza 1.6 veces más recursos computacionales que el caso 2; el caso 2 utiliza 2.25 veces más recursos computacionales que el caso 3; el caso 3 utiliza 27.52 veces más recursos computacionales que el caso 4; finalmente, el caso 4 utiliza 21.8 veces los recursos de cómputo que el caso 5. Con las hipótesis tomadas en los casos 3 y 4, es posible llevar a cabo estimaciones iniciales del proceso (por ejemplo, tiempo de fusión y

temperatura de la carga), pero no se tienen en cuenta los efectos completos de convección entre el aire y la carga, lo cual puede ser importante para un análisis de detalle. El principal inconveniente del enfoque más exhaustivo (caso 1) es su alto costo computacional, pero esto puede ser compensado con los recursos de cómputo actuales que permiten el análisis de un caso en pocos días.

La ventaja computacional de los modelos simplificados (casos 2-5 vs. caso 1) debe ser considerada para cada aplicación específica. La diferencia en el tiempo de computación es muy importante, por lo que el propósito y el número de simulaciones necesarias deben ser siempre considerados. En este trabajo se han discutido y comparado las predicciones y el costo computacional de las simulaciones simplificadas, lo cual podría ayudar a una decisión en este sentido.

7.2 Horno de mantenimiento

Se han presentado simulaciones tridimensionales en estado transitorio con el propósito de estimar el comportamiento térmico en un horno de mantenimiento calentado por un sistema de resistencias eléctricas. Se han detallado las suposiciones asumidas, metodología seguida y una discusión de los principales resultados obtenidos.

Como una primera aproximación, la simetría de la geometría se ha utilizado para reducir los recursos computacionales requeridos y sólo un cuarto de dominio ha sido simulado inicialmente. Sin embargo, las velocidades estimadas en el flujo de la carga fundida, sugieren que los patrones inducidos por los efectos de convección tienen un comportamiento tridimensional. Por esta razón se ha realizado una nueva simulación con el dominio completo.

Las simulaciones numéricas muestran que el horno de mantenimiento puede sostener la temperatura de la carga fundida por encima del punto de fusión, en una distribución de temperatura muy homogénea en la carga y en un estado de operación casi constante. Las temperaturas estimadas son muy razonables y concuerdan con las observaciones empíricas realizadas en un prototipo real para un ciclo de operación típico.

La distribución de temperaturas y flujos de energía estimados por los dos casos son casi los mismos. Sin embargo, los patrones de flujo del aluminio fundido difieren en gran medida entre los dos enfoques. La evaluación comparativa del horno de mantenimiento con problemas simplificadas de convección natural, permite señalar que el patrón de flujo esperado en la carga fundida, debe ser similar a la obtenida con el dominio completo, por lo tanto, una conclusión principal es que la condición de simetría impide el pleno desarrollo de los patrones de flujo en hornos con sistemas de calefacción de estado cuasi-estacionario. Los trabajos de flujos inducidos por convección natural consideran dominios simplificados con el fin de utilizar tamaños de malla más pequeños y lograr condiciones de DNS, pero los requisitos para resolver todas las escalas de la turbulencia es prohibitivamente costoso para los propósitos industriales actuales.

Incluso para las temperaturas homogéneas presentadas en el horno, los modelos muestran la capacidad de estimar patrones complejos de movimiento dentro de la carga fundida causado por los efectos de convección. Estos comportamientos se observan generalmente en sistemas de convección natural como resultado de su inestabilidad intrínseca. Diferentes publicaciones han sido presentadas en metales con puntos de fusión cerca de la temperatura ambiente, geometrías simplificadas y condiciones de frontera controladas; pero, debido a la dificultad en las mediciones en hornos industriales de aluminio, actualmente no es posible una caracterización detallada del flujo interno, y no existe ninguna referencia bibliográfica sobre este tema para este tipo de dispositivos.

En términos prácticos, la homogeneidad de la temperatura en el interior de la carga hace que los enfoques actuales sean lo suficientemente buenos para fines industriales. El efecto de convección no parece tener un impacto importante en el balance energético global, pero es necesario tener en cuenta el movimiento de la carga fundida para evitar la sobre estimación de la temperatura. Asimismo, los patrones transitorios en la carga imposibilitan la obtención de una solución de estado estacionario.

7.3 Perspectivas para trabajo futuro

Teniendo en cuenta los resultados de la presente tesis, el paso siguiente natural es la validación de las metodologías empleadas con datos experimentales completos. Sin embargo, una validación experimental rigurosa para las simulaciones numéricas de hornos de fusión y mantenimiento, debe incluir las medidas exactas de velocidades y temperaturas en la carga fundida, pero este tipo de plataformas experimentales no están disponibles actualmente para hornos industriales de metal, y por supuesto, supera el alcance y objetivos del presente trabajo o de líneas de investigación derivadas.

Las simplificaciones consideradas para esta tesis deben ser reducidas como un trabajo futuro. En primer lugar, se incluirán modelos más complejos en la solución, es decir, modelos de turbulencia, geometrías tridimensionales y no simplificadas, o mallas más refinadas. Estos problemas se resolverán a medida que aumentan los recursos computacionales disponibles. En segundo lugar, diferentes fenómenos pueden ser incorporados para un análisis más completo, por ejemplo, reacciones químicas para las interacciones con materiales de aleación y la oxidación de la carga, influencia de las fuentes de chatarra (composición, forma y tamaño) y evolución de efectos metalúrgicos; para este fin , varios submodelos deben ser acoplados dentro de la solución de CFD. Por último, una combinación de diferentes físicas se puede añadir a la presente solución; como un ejemplo, actualmente la expansión de volumen del metal es típicamente solucionada con el método VOF, pero esta técnica es muy difícil de en problemas conjugados y no se encuentra disponible en códigos comerciales; los códigos multifísicos presentan una oportunidad en crecimiento para calcular este y otro tipo de combinaciones de fenómenos.

Realmente, el trabajo futuro se centrará principalmente en la captura de información esencial requerida en hornos industriales. El compromiso entre la economía de los modelos y la calidad de la predicción debe ser cuidadosamente analizado para cualquier aplicación particular. Mientras los recursos computacionales y códigos comerciales se vuelven lo suficientemente integrales, rápidos y accesibles a personal no calificado, las simulaciones numéricas se utilizarán para el desarrollo de modelos reducidos

simplificados, que permitan una rápida evaluación de los parámetros clave en hornos industriales.

References

ABBASSI, A. & KHOSHMANESH, K. 2008. Numerical simulation and experimental analysis of an industrial glass melting furnace. *Applied Thermal Engineering,* 28**,** 450-459.

AHN, S., BEAMAN, J. J., WILLIAMSON, R. L. & MELGAARD, D. K. 2009. Model-Based Control of Electroslag Remelting Process Using Unscented Kalman Filter. *Journal of Dynamic Systems, Measurement, and Control,* 132**,** 011011-011011.

AL-ABIDI, A. A., BIN MAT, S., SOPIAN, K., SULAIMAN, M. Y. & MOHAMMED, A. T. 2013. CFD applications for latent heat thermal energy storage: a review. *Renewable and Sustainable Energy Reviews,* 20**,** 353-363.

ALEXIADES, V. & SOLOMON, A. D. 1993. *Mathematical Modeling of Melting and Freezing Processes*, HEMISPHERE PUBLISHING CORPORATION.

ANSYS 2012. ANSYS FLUENT 14.0 User's Guide.

ARASU, A. V. & MUJUMDAR, A. S. 2012. Numerical study on melting of paraffin wax with Al2O3 in a square enclosure. *International Communications in Heat and Mass Transfer,* 39**,** 8-16.

ARZPEYMA, N., WIDLUND, O., ERSSON, M., OUML, NSSON, P. & AUML 2013. Mathematical Modeling of Scrap Melting in an EAF Using Electromagnetic Stirring. *ISIJ International,* 53**,** 48-55.

ASSAEL, M. J., KAKOSIMOS, K., BANISH, R. M., BRILLO, J., EGRY, I., BROOKS, R., QUESTED, P. N., MILLS, K. C., NAGASHIMA, A., SATO, Y. & WAKEHAM, W. A. 2006. Reference Data for the Density and Viscosity of Liquid Aluminum and Liquid Iron. *Journal of Physical and Chemical Reference Data,* 35**,** 285-300.

ASSIS, E., KATSMAN, L., ZISKIND, G. & LETAN, R. 2007. Numerical and experimental study of melting in a spherical shell. *International Journal of Heat and Mass Transfer,* 50**,** 1790-1804.

BAILON-CUBA, J., EMRAN, M. S. & SCHUMACHER, J. 2010. Aspect ratio dependence of heat transfer and large-scale flow in turbulent convection. *Journal of Fluid Mechanics,* 655**,** 152-173.

BAYLISS, C. The Aluminium Story. International Aluminium Congress, 2012 São Paulo.

BELHAMADIA, Y., KANE, A. S. & FORTIN, A. 2012. An enhanced mathematical model for phase change problems with natural convection. *International Journal of Numerical Analysis & Modeling, Series B*.

BELT, C. K., GOLCHERT, B. M., KING, P. E., PETERSON, R. D. & TESSANDORI, J. L. 2006. Industrial application of DOE energy savings technologies to aluminum melting. *Light Metals***,** 881-885.

BEN-DAVID, O., LEVY, A., MIKHAILOVICH, B. & AZULAY, A. 2013. 3D numerical and experimental study of gallium melting in a rectangular container. *International Journal of Heat and Mass Transfer,* 67**,** 260-271.

BERMÚDEZ, A., GÓMEZ, D., MUÑIZ, M. C. & SALGADO, P. 2007a. A FEM/BEM for axisymmetric electromagnetic and thermal modelling of induction furnaces. *International Journal for Numerical Methods in Engineering,* 71**,** 856-878.

BERMÚDEZ, A., GÓMEZ, D., MUÑIZ, M. C. & SALGADO, P. 2007b. Transient numerical simulation of a thermoelectrical problem in cylindrical induction heating furnaces. *Advances in Computational Mathematics,* 26**,** 39-62.

BERMÚDEZ, A., GÓMEZ, D., MUÑIZ, M. C., SALGADO, P. & VÁZQUEZ, R. 2009. Numerical simulation of a thermo-electromagneto-hydrodynamic problem in an induction heating furnace. *Applied Numerical Mathematics,* 59**,** 2082-2104.

BERMÚDEZ, A., GÓMEZ, D., MUÑIZ, M. C. & VÁZQUEZ, R. 2011. A thermo-electrical problem with a nonlocal radiation boundary condition. *Mathematical and Computer Modelling,* 53**,** 63-80.

BERMÚDEZ, A. & OTERO, M. V. 2004. Numerical solution of a three-dimensional solidification problem in aluminium casting. *Finite Elements in Analysis and Design,* 40**,** 1885-1906.

BERMÚDEZ, A., REALES, C., RODRÍGUEZ, R. & SALGADO, P. 2010. Numerical analysis of a finite-element method for the axisymmetric eddy current model of an induction furnace. *IMA journal of numerical analysis,* 30**,** 654-676.

BOIN, U. M. J. & BERTRAM, M. 2005. Melting standardized aluminum scrap: A mass balance model for europe. *JOM,* 57**,** 26-33.

BRANDT, J. L. 1984. Properties of pure aluminum. *In:* HATCH, J. E. (ed.) *Aluminum: Properties and Physical Metallurgy.* Ohio: American Society for Metals.

BRIGHAM, E. O. 1988. *The Fast Fourier Transform and Its Applications*, Prentice Hall.

CADAVID, F., HERRERA, B. & AMELL, A. 2010. Numerical simulation of the flow streams behavior in a self-regenerative crucible furnace. *Applied Thermal Engineering,* 30**,** 826-832.

CARBOSANLUIS. 2007. *Carbo San Luis* [Online]. Available: http://www.carbosanluis.com.ar/REFRACT CSL -2007.pdf Last accessed 11 Dec 2013].

CD-ADAPCO 2004. STAR-CCM+ documentation. Version 6.02.

COLOMBO, V., CONCETTI, A., GHEDINI, E., DALLAVALLE, S. & VANCINI, M. 2008. Understanding plasma fluid dynamics inside plasma torches through advanced modeling. *Plasma Science, IEEE Transactions on,* 36**,** 389-402.

COURTESSOLE, C. & ETAY, J. 2013. Flows and mass transfers in two superimposed liquid layers in an induction furnace. *International Journal of Heat and Mass Transfer,* 65**,** 893-906.

CRUNKLETON, D. W., NARAYANAN, R. & ANDERSON, T. J. 2006. Numerical simulations of periodic flow oscillations in low Prandtl number fluids. *International Journal of Heat and Mass Transfer,* 49**,** 427-438.

CHANG, L. Z. & LI, B. Z. 2008. Numerical simulation of temperature fields in electroslag remelting slab ingots. *Acta Metallurgica Sinica (English Letters),* 21**,** 253-259.

CHAU, S. W. & HSU, K. L. 2011. Modeling steady axis-symmetric thermal plasma flow of air by a parallelized magneto-hydrodynamic flow solver. *Computers & Fluids,* 45**,** 109-115.

CHAU, S. W., HSU, K. L., LIN, D. L., CHEN, J. S. & TZENG, C. C. 2007. Modeling and experimental validation of a 1.2 MW DC transferred well-type plasma torch. *Computer Physics Communications,* 177**,** 114-117.

CHAU, S. W., LU, S. Y. & WANG, P. J. 2011. Modeling of axis-symmetric steam plasma flow in a non-transferred torch. *Computer Physics Communications,* 182**,** 152-154.

CHILLÀ, F. & SCHUMACHER, J. 2012. New perspectives in turbulent Rayleigh-Bénard convection. *The European Physical Journal E,* 35**,** 1-25.

CHOUDHARY, M. K., VENUTURUMILLI, R. & HYRE, M. R. 2010. Mathematical Modeling of Flow and Heat Transfer Phenomena in Glass Melting, Delivery, and Forming Processes. *International Journal of Applied Glass Science,* 1**,** 188-214.

CHRISTY. 2004. *Catalogue: Christy refractories* [Online]. Available: http://www.christyco.com/refractories.html Last accessed 28 Dec 2013].

DARWISH, S. M. H. 1991. The finite-element modeling of aluminum holding furnaces. *JOM,* 43**,** 36-38.

DARZI, A. R., FARHADI, M. & SEDIGHI, K. 2012. Numerical study of melting inside concentric and eccentric horizontal annulus. *Applied Mathematical Modelling,* 36**,** 4080-4086.

DAS, S. K. 2007. Improving Energy Efficiency in Aluminum Melting, DE-FC07-01ID14023. United States of America: Secat, Inc. University of Kentucky.

DAS, S. K. 2008. Aluminum melting furnace design optimization to improve energy efficiency by integrated modeling. United States of America: Center for Aluminum Technology, University of Kentucky.

DAVIES, S. B., MASTERS, I. & GETHIN, D. T. 2013. Numerical Modelling of a Rotary Aluminum Recycling Furnace. *Recycling of Metals and Engineered Materials.* John Wiley & Sons, Inc.

DELLAROCCA, A., FANTUZZI, M., BATTAGLIA, V. & MALFA, E. 2012. Advanced design methods for rotary hearth furnaces. *Steel Times International,* 36.

DHAIDAN, N. S., KHODADADI, J. M., AL-HATTAB, T. A. & AL-MASHAT, S. M. 2013a. Experimental and numerical investigation of melting of NePCM inside an annular container under a constant heat flux including the effect of eccentricity. *International Journal of Heat and Mass Transfer,* 67**,** 455-468.

DHAIDAN, N. S., KHODADADI, J. M., AL-HATTAB, T. A. & AL-MASHAT, S. M. 2013b. Experimental and numerical investigation of melting of phase change material/nanoparticle suspensions in a square container subjected to a constant heat flux. *International Journal of Heat and Mass Transfer,* 66**,** 672-683.

DHAIDAN, N. S., KHODADADI, J. M., AL-HATTAB, T. A. & AL-MASHAT, S. M. 2013c. Experimental and numerical study of constrained melting of n-octadecane with CuO nanoparticle dispersions in a horizontal cylindrical capsule subjected to a constant heat flux. *International Journal of Heat and Mass Transfer,* 67**,** 523-534.

DÍAZ, I. O., ABAD, P. & MOLINA, A. 2013. Design of a day tank glass furnace using a transient model and steady-state computation fluid dynamics. *Applied Thermal Engineering,* 52**,** 555-565.

DOEBELIN, E. O. 1990. *Measurement systems: application and design*, McGraw-Hill.

DUPRÉ. 2008. *Catalogue: Dupré minerals* [Online]. Available: http://www.dupreminerals.com/en/ Last accessed 28 Dec 2013].

DUTIL, Y., ROUSSE, D. R., SALAH, N. B., LASSUE, S. & ZALEWSKI, L. 2011. A review on phase-change materials: Mathematical modeling and simulations. *Renewable and Sustainable Energy Reviews,* 15**,** 112-130.

EDEFU. 2010. *EDEFU Project: New Designs of Ecological Furnaces* [Online]. Available: http://www.edefu.eu/ Last accessed 11 Dec 2013].

EL QARNIA, H., DRAOUI, A. & LAKHAL, E. K. 2013. Computation of melting with natural convection inside a rectangular enclosure heated by discrete protruding heat sources. *Applied Mathematical Modelling,* 37**,** 3968-3981.

ERNST, K., KOPAINSKY, J. & MAECKER, H. 1973. The Energy Transport, Including Emission and Absorption, in N2-Arcs of Different Radii. *Plasma Science, IEEE Transactions on,* 1**,** 3-16.

FARAJI, M. & EL QARNIA, H. 2010. Numerical study of melting in an enclosure with discrete protruding heat sources. *Applied Mathematical Modelling,* 34**,** 1258-1275.

FERZIGER, J. H. & PERIĆ, M. 2002. *Computational Methods for Fluid Dynamics*, Springer London, Limited.

GEBHART, B. 1988. *Buoyancy-Induced Flows And Transport*, Hemisphere Publishing Corporation.

GLEIZES, A., GONZALEZ, J. J. & FRETON, P. 2005. Thermal plasma modelling. *Journal of Physics D: Applied Physics,* 38**,** R153.

GLEIZES, A., GONZALEZ, J. J., LIANI, B. & RAYNAL, G. 1993. Calculation of net emission coefficient of thermal plasmas in mixtures of gas with metallic vapour. *Journal of Physics D: Applied Physics,* 26**,** 1921.

GLEIZES, A., RAHMANI, B., GONZALEZ, J. & LIANI, B. 1991. Calculation of net emission coefficient in N2, SF6 and SF6-N2 arc plasmas. *Journal of Physics D: Applied Physics,* 24**,** 1300.

GOLCHERT, B. M., ZHOU, C., QUENETTE, A., HAN, Q. & KING, P. E. 2005. Combustion space modeling of an aluminum furnace. *Light Metals***,** 887-892.

GONZALEZ, J. J., FRETON, P. & GLEIZES, A. 2002. Comparisons between two- and three-dimensional models: gas injection and arc attachment. *Journal of Physics D: Applied Physics,* 35**,** 3181.

GONZALEZ, J. J., LAGO, F., FRETON, P., MASQUÈRE, M. & FRANCERIES, X. 2005. Numerical modelling of an electric arc and its interaction with the anode: part II. The three-dimensional model—influence of external forces on the arc column. *Journal of Physics D: Applied Physics,* 38**,** 306.

GONZÁLEZ, O. J. P., RAMÍREZ, A., MARCO A. & CONEJO, A. N. 2010a. Effect of Arc Length on Fluid Flow and Mixing Phenomena in AC Electric Arc Furnaces. *ISIJ International,* 50**,** 1-8.

GONZÁLEZ, O. J. P., RAMÍREZ, A., MARCO A. & CONEJO, A. N. 2010b. Mathematical Modeling of the Melting Rate of Metallic Particles in the Electric Arc Furnace. *ISIJ International,* 50**,** 9-16.

GOODFELLOW. 2012. *Catalogue: Goodfellow* [Online]. Available: http://www.goodfellow.com Last accessed 28 Dec 2013].

GREEN, J. A. S. 2007. *Aluminum Recycling and Processing for Energy Conservation and Sustainability*, ASM International.

GRINYS, T., TAMULEVIČIUS, S., MOCKEVIČIUS, I. & ANDRULEVIČIUS, M. 2007. Probe Temperature Measurements and Optical Emission Spectroscopy in Vacuum Plasma Spraying Process Control. *MATERIALS SCIENCE-MEDZIAGOTYRA,* 13**,** 346-350.

GRÖTZBACH, G. 1983. Spatial resolution requirements for direct numerical simulation of the Rayleigh-Bénard convection. *Journal of Computational Physics,* 49**,** 241-264.

GUO, D. & IRONS, G. A. 2008. Modelling of steel scrap movement. *Applied Mathematical Modelling,* 32**,** 2041-2049.

HACHEM, E., JANNOUN, G., VEYSSET, J., HENRI, M., PIERROT, R., POITRAULT, I., MASSONI, E. & COUPEZ, T. 2013. Modeling of heat transfer and turbulent flows inside industrial furnaces. *Simulation Modelling Practice and Theory,* 30**,** 35-53.

HAN, S. H., BAEK, S. W. & KIM, M. Y. 2009. Transient radiative heating characteristics of slabs in a walking beam type reheating furnace. *International Journal of Heat and Mass Transfer,* 52**,** 1005-1011.

HANNOUN, N., ALEXIADES, V. & MAI, T. Z. 2005. A reference solution for phase change with convection. *International Journal for Numerical Methods in Fluids,* 48**,** 1283-1308.

HOF, B., JUEL, A., ZHAO, L., HENRY, D., HADID, H. B. & MULLIN, T. 2004. On the onset of oscillatory convection in molten gallium. *Journal of Fluid Mechanics,* 515**,** 391-413.

HONGJIE, Y., GANG, L., ZELIN, X., PING, Z. & ZHUO, C. Numerical simulation on combustion process and optimization of structure for the reclaimed copper reverberatory furnace. Intelligent System Design and Engineering Application (ISDEA), 2012 Second International Conference on, 2012. IEEE, 1063-1066.

HU, H. & ARGYROPOULOS, S. A. 1996. Mathematical modelling of solidification and melting: A review. *Modelling and Simulation in Materials Science and Engineering,* 4**,** 371-396.

HUR, M., HYUNG HWANG, T., TAE JU, W., MIN LEE, C. & HONG, S. H. 2001. Numerical analysis and experiments on transferred plasma torches for finding appropriate operating conditions and electrode configuration for a waste melting process. *Thin Solid Films,* 390**,** 186-191.

INCROPERA, F. P. & DEWITT, D. P. 1990. *Fundamentals of heat and mass transfer*, Wiley.

IWAO, T., IWASE, K., TASHIRO, S., TANAKA, M. & YUMOTO, M. 2008. Numerical simulation of argon twin torch plasma arc for high heating efficiency. *Vacuum,* 83**,** 34-38.

JBI. 2013. *Jamaica Bauxite Institute: Bayer Process* [Online]. Available: http://jbi.org.jm/pages/bayer_process Last accessed 11 Dec 2013].

JONES, B. J., SUN, D., KRISHNAN, S. & GARIMELLA, S. V. 2006. Experimental and numerical study of melting in a cylinder. *International Journal of Heat and Mass Transfer,* 49**,** 2724-2738.

JONES, R. T., BARCZA, N. A. & CURR, T. R. 2001. *Plasma Developments in Africa* [Online]. Available: http://www.mintek.co.za/Pyromet/Plasma/Plasma.htm Last accessed 11 Dec 2013].

JUÁREZ, R., FLORES, A., MACIAS, E. & REYES, N. 2009. Análisis del comportamiento de flujo de fluidos en un horno de reverbero agitado con diferentes impulsores, mediante la modelación física y numérica. *Revista de metalurgia,* 45**,** 384-396.

KELKAR, K. M., PATANKAR, S. V. & MITCHELL, A. Computational modeling of the electroslag remelting (esr) process used for the production of ingots of high-performance alloys. Proceeding in International Symposium on Liquid metal Processing and Casting, Santa Fe, USA, 2005. 137-144.

KHANTHAL. 2011. *Catalogue: Khanthal* [Online]. Available: http://www.kanthal.com/ Last accessed 11 Dec 2013].

KHARICHA, A., LUDWIG, A. & WU, M. 2005. Shape and stability of the slag/melt interface in a small dc ESR process. *Materials Science and Engineering: A,* 413–414**,** 129-134.

KHARICHA, A., LUDWIG, A. & WU, M. 2011. 3D simulation of the melting during an industrial scale electro-slag remelting process. *LMPC,* 2011**,** 41-48.

KHODADADI, J. M. & ZHANG, Y. 2001. Effects of buoyancy-driven convection on melting within spherical containers. *International Journal of Heat and Mass Transfer,* 44**,** 1605-1618.

KHOEI, A. R., MASTERS, I. & GETHIN, D. T. 2003. Numerical modelling of the rotary furnace in aluminium recycling processes. *Journal of Materials Processing Technology,* 139**,** 567-572.

KING, P. E., GOLCHERT, B. M., LI, T., HASSAN, M. & HAN, Q. 2005a. Energy efficient operation of aluminum furnaces. Albany Research Center (ARC), Albany, OR; Argonne National Laboratory (ANL), Argonne, IL; University of Kentucky, Lexington, KY;; Oak Ridge National Laboratory (ORNL), Oak Ridge, TN.

KING, P. E., HAYES, M., LI, T., HAN, Q., HASSAN, M. & GOLCHERT, B. 2005b. Design and operation of an experimental reverberatory aluminum furnace. Albany Research Center (ARC), Albany, OR.

KIRPO, M., JAKOVIČS, A., NACKE, B., BAAKE, E. & LANGEJUERGEN, M. 2008. LES of Heat and Mass Exchange in Induction Channel Furnaces. *Przegląd Elektrotechniczny,* 84**,** 154-158.

LACROIX, M. & VOLLER, V. R. 1990. Finite Difference Solutions of Solidification Phase Change Problems: Transformed Versus Fixed Grids. *Numerical Heat Transfer, Part B: Fundamentals,* 17**,** 25-41.

LAGO, F., GONZALEZ, J. J., FRETON, P. & GLEIZES, A. 2004. A numerical modelling of an electric arc and its interaction with the anode: Part I. The two-dimensional model. *Journal of Physics D: Applied Physics,* 37**,** 883.

LANGEJÜRGEN, M., KIRPO, M., JAKOVICS, A. & BAAKE, E. 2008. Numerical simulation of mass and heat transport in induction channel furnaces. *International Scientific Colloquium-Modelling for Electromagnetic Processing.* Hannover, Germany.

LEE, J. R. & PARK, I. S. 2012. Numerical analysis for prandtl number dependency on natural convection in an enclosure having a vertical thermal gradient with a square insulator inside. *Nuclear engineering and technology,* 44**,** 283-296.

LI, B., WANG, F. & TSUKIHASHI, F. 2012. Current, Magnetic Field and Joule Heating in Electroslag Remelting Processes. *ISIJ International,* 52**,** 1289-1295.

LI, T., HASSAN, M., KUWANA, K., SAITO, K. & KING, P. 2006. Performance of secondary aluminum melting: Thermodynamic analysis and plant-site experiments. *Energy,* 31**,** 1769-1779.

LI, T., KING, P. E., HASSAN, M., KUWANA, K. & SAITO, K. 2005. *An analytical furnace model for optimizing aluminum melting furnaces*.

LI, T. X., HASSAN, M., KUWANA, K., SAITO, K., VISWANATHAN, S., HAN, Q. & KING, P. E. 2003. *Thermodynamic analyses of energy utilization and pollutant formation control in secondary aluminum melting furnaces*.

LOGAR, V., DOVŽAN, D. & ŠKRJANC, I. 2011. Mathematical Modeling and Experimental Validation of an Electric Arc Furnace. *ISIJ International,* 51**,** 382-391.

LOGAR, V., DOVŽAN, D. & ŠKRJANC, I. 2012a. Modeling and Validation of an Electric Arc Furnace: Part 1, Heat and Mass Transfer. *ISIJ International,* 52**,** 402-412.

LOGAR, V., DOVŽAN, D. & ŠKRJANC, I. 2012b. Modeling and Validation of an Electric Arc Furnace: Part 2, Thermo-chemistry. *ISIJ International,* 52**,** 413-423.

LOGAR, V. & ŠKRJANC, I. 2012a. Development of an Electric Arc Furnace Simulator Considering Thermal, Chemical and Electrical Aspects. *ISIJ International,* 52**,** 1924-1926.

LOGAR, V. & ŠKRJANC, I. 2012b. Modeling and Validation of the Radiative Heat Transfer in an Electric Arc Furnace. *ISIJ International,* 52**,** 1225-1232.

LONGEON, M., SOUPART, A., FOURMIGUÉ, J.-F., BRUCH, A. & MARTY, P. 2013. Experimental and numerical study of annular PCM storage in the presence of natural convection. *Applied Energy,* 112**,** 175-184.

MAHDAOUI, M., KOUSKSOU, T., BLANCHER, S., AIT MSAAD, A., EL RHAFIKI, T. & MOUQALLID, M. 2013. A numerical analysis of solid–liquid phase change heat transfer around a horizontal cylinder. *Applied Mathematical Modelling*.

MATWEB. 2012. *MatWeb data base* [Online]. Available: www.matweb.com Last accessed 28 Dec 2013].

MEI, S., XIE, J., JIN, M. & HAN, D. Numerical simulation in combustion space of an oil fired float glass furnace. System Simulation and Scientific Computing, 2008. ICSC 2008. Asia Simulation Conference-7th International Conference on, 2008. IEEE, 1091-1094.

MENCINGER, J. 2004. Numerical simulation of melting in two-dimensional cavity using adaptive grid. *Journal of Computational Physics,* 198**,** 243-264.

MILLS, A. F. 1992. *Heat Transfer*, Irwin.

MUCHOVÁ, L. & EDER, P. 2010. End-of-waste Criteria for Aluminium and Aluminium Alloy Scrap: Technical Proposals. Luxembourg: Joint Research Centre, Institute for Prospective Technological Studies.

MURPHY, A. 1993. Diffusion in equilibrium mixtures of ionized gases. *Physical Review E,* 48**,** 3594.

MURPHY, A. B. 2001. Thermal plasmas in gas mixtures. *Journal of Physics D: Applied Physics,* 34**,** R151.

NABERTHERM. 2013. *Catalogue: Nabertherm GmbH* [Online]. Available: http://www.nabertherm.com/ Last accessed 11 Dec 2013].

NAFARIZAL, N., RAHMAT, S., NADZLIN, T. & IBRAHIM, T. 2009. An introduction to optical emission spectroscopy and laser-aided spectroscopy techniques for low-temperature plasma analyses. *Engineering and Technology***,** 1-4.

NAGHIZADEH-KASHANI, Y., CRESSAULT, Y. & GLEIZES, A. 2002. Net emission coefficient of air thermal plasmas. *Journal of Physics D: Applied Physics,* 35**,** 2925.

NIECKELE, A. O., NACCACHE, M. F. & GOMES, M. S. 2004. Numerical modeling of an industrial aluminum melting furnace. *Journal of Energy Resources Technology,* 126**,** 72-81.

NIECKELE, A. O., NACCACHE, M. F. & GOMES, M. S. P. 2011. Combustion performance of an aluminum melting furnace operating with natural gas and liquid fuel. *Applied Thermal Engineering,* 31**,** 841-851.

OUTOKUMPU. 2008. *Catalogue: Outokumpu VDM* [Online]. Available: http://www.thyssenkrupp-vdm.com/ Last accessed 28 Dec 2013].

PATEL, A. D. & KELKAR, K. M. 2009. New Insights into the electro-slag remelting process using mathematical modeling. *TMS, United States: The Minerals, Matals & Materials Society***,** 69-76.

PAUTY, E., LABOUDIGUE, B. & ETAY, J. 2000. Numerical simulation of the flow and the solid transport when tilting a holding furnace. *Metallurgical and Materials Transactions B,* 31**,** 207-214.

PAVLOVS, S., JAKOVIČS, A., BAAKE, E., NACKE, B. & KIRPO, M. 2011. LES modelling of turbulent flow, heat exchange and particle transport in industrial induction channel furnaces. *Magnetohydrodynamics,* 47**,** 399-412.

PENMETSA, S., LI, T., KING, P. E. & SAITO, K. 2005. Scale modeling of aluminum melting furnaces. University of Kentucky, Lexington, KY;; Albany Research Center (ARC), Albany, OR.

POPE, S. B. 2000. *Turbulent Flows*, Cambridge University Press.

PORTER, D. A. & EASTERLING, K. E. 1992. *Phase Transformations in Metals and Alloys, Third Edition (Revised Reprint)*, Taylor & Francis.

POULIKAKOS, D. 1994. *Conduction Heat Transfer*, Prentice Hall.

PRASAD, V. V. S. & RAO, A. S. 2000. Electroslag Melting for Recycling Scrap of Valuable Metals and Alloys. *Recycling of Metals and Engineered Materials.* John Wiley & Sons, Inc.

PUITS, R. D., RESAGK, C. & THESS, A. 2013. Thermal boundary layers in turbulent Rayleigh–Bénard convection at aspect ratios between 1 and 9. *New Journal of Physics,* 15**,** 013040.

RATH. 2012. *Catalogue: Rath* [Online]. Available: http://www.rath-usa.com/pds-ceramic-fiber-paper.html Last accessed 28 Dec 2013].

RÜCKERT, A. & PFEIFER, H. Numerical Modelling of the Electroslag Remelting Process. METAL 2007: 16 th International Metallurgical and Materials Conference, 2007.

RÜCKERT, A. & PFEIFER, H. 2009. Mathematical modelling of the flow field, temperature distribution, melting and solidification in the electroslag remelting process. *Magnetohydrodynamics,* 45**,** 527-533.

SAMARSKII, A. A., VABISHCHEVICH, P. N., ILIEV, O. P. & CHURBANOV, A. G. 1993. Numerical simulation of convection/diffusion phase change problems—a review. *International Journal of Heat and Mass Transfer,* 36**,** 4095-4106.

SARANI, A., NIKIFOROV, A. Y. & LEYS, C. 2010. Atmospheric pressure plasma jet in Ar and Ar/H2O mixtures: Optical emission spectroscopy and temperature measurements. *Physics of Plasmas (1994-present),* 17**,** -.

SCANLON, T. J. & STICKLAND, M. T. 2004. A numerical analysis of buoyancy-driven melting and freezing. *International Journal of Heat and Mass Transfer,* 47**,** 429-436.

SCHLESINGER, M. E. 2006. *Aluminum Recycling*, Taylor & Francis.

SCHMITZ, C. 2006. *Handbook of Aluminium Recycling*, Vulkan.

SHARIFI, N., ROBAK, C. W., BERGMAN, T. L. & FAGHRI, A. 2013. Three-dimensional PCM melting in a vertical cylindrical enclosure including the effects of tilting. *International Journal of Heat and Mass Transfer,* 65**,** 798-806.

SISMANOGLU, B. N., AMORIM, J., SOUZA-CORRÊA, J. A., OLIVEIRA, C. & GOMES, M. P. 2009. Optical emission spectroscopy diagnostics of an atmospheric pressure direct current microplasma jet. *Spectrochimica Acta Part B: Atomic Spectroscopy,* 64**,** 1287-1293.

SKAMOL. 2010. *Catalogue: Skamol* [Online]. Available: http://www.skamol.com/ Last accessed 28 Dec 2013].

SPITANS, S., JAKOVIČS, A., BAAKE, E. & NACKE, B. 2010. Numerical modelling of free surface dynamics of conductive melt in induction crucible furnace. *Magnetohydrodynamics,* 47**,** 317-328.

SPITANS, S., JAKOVIČS, A., BAAKE, E. & NACKE, B. 2011. Numerical modelling of free surface dynamics of melt in an alternate electromagnetic field. *Magnetohydrodynamics,* 47**,** 461-473.

SPX. 2013. *Catalogue: SPX-Thermal product solution* [Online]. Available: http://www.thermalproductsolutions.com/ Last accessed 11 Dec 2013].

STRIKOMELTER. 2013. *Catalogue: StrikoWestofen group* [Online]. Available: http://www.strikowestofen.com/ Last accessed 11 Dec 2013].

SWAMINATHAN, C. R. & VOLLER, V. R. 1992. A general enthalpy method for modeling solidification processes. *Metallurgical Transactions B,* 23**,** 651-664.

SWAMINATHAN, C. R. & VOLLER, V. R. 1993. On the enthalpy method. *International Journal of Numerical Methods for Heat & Fluid Flow,* 3**,** 233-244.

SWAMINATHAN, C. R. & VOLLER, V. R. 1997. Towards a general numerical scheme for solidification systems. *International Journal of Heat and Mass Transfer,* 40**,** 2859-2868.

TAN, F. L., HOSSEINIZADEH, S. F., KHODADADI, J. M. & FAN, L. 2009. Experimental and computational study of constrained melting of phase change materials (PCM) inside a spherical capsule. *International Journal of Heat and Mass Transfer,* 52**,** 3464-3472.

TANAKA, M. & LOWKE, J. J. 2007. Predictions of weld pool profiles using plasma physics. *Journal of Physics D: Applied Physics,* 40**,** R1.

TENDERO, C., TIXIER, C., TRISTANT, P., DESMAISON, J. & LEPRINCE, P. 2006. Atmospheric pressure plasmas: A review. *Spectrochimica Acta Part B: Atomic Spectroscopy,* 61**,** 2-30.

TOTTEN, G. E. & MACKENZIE, D. S. 2003a. *Handbook of Aluminum: Vol. 1: Physical Metallurgy and Processes*, Taylor & Francis.

TOTTEN, G. E. & MACKENZIE, D. S. 2003b. *Handbook of Aluminum: Volume 2: Alloy Production and Materials Manufacturing*, Taylor & Francis.

TRELLES, J. P., CHAZELAS, C., VARDELLE, A. & HEBERLEIN, J. V. R. 2009. Arc Plasma Torch Modeling. *Journal of Thermal Spray Technology,* 18**,** 728-752.

TRIPATHI, A., SAHA, J. K., SINGH, J. B. & AJMANI, S. K. 2012. Numerical Simulation of Heat Transfer Phenomenon in Steel Making Ladle. *ISIJ International,* 52**,** 1591-1600.

TSESMELIS, K. The role of recycling in aluminium sustainability: a quantitative approach. 20th Int'l recycled aluminium conference, 2012 Salzburg, Austria.

ÜNLÜ, N. & DROUET, M. G. 2002. Comparison of salt-free aluminum dross treatment processes. *Resources, Conservation and Recycling,* 36**,** 61-72.

VERZICCO, R. & CAMUSSI, R. 1997. Transitional regimes of low-Prandtl thermal convection in a cylindrical cell. *Physics of Fluids (1994-present),* 9**,** 1287-1295.

VIDALAIN, G., GOSSELIN, L. & LACROIX, M. 2009. An enhanced thermal conduction model for the prediction of convection dominated solid–liquid phase change. *International Journal of Heat and Mass Transfer,* 52**,** 1753-1760.

VOLLER, V., BRENT, A. & REID, K. 1988. Computational Modelling Framework for Analysis of Metallurgical Solidification Processes and Phenomena. *The Institute of Metals***,** 378-380.

VOLLER, V. R. 1997. An Overview of Numerical Methods for Solving Phase-Change Problems. *Advances in Numerical Heat Transfer.*

VOLLER, V. R., CROSS, M. & MARKATOS, N. C. 1987. An enthalpy method for convection/diffusion phase change. *International Journal for Numerical Methods in Engineering,* 24**,** 271-284.

VOLLER, V. R. & PRAKASH, C. 1987. A fixed grid numerical modelling methodology for convection-diffusion mushy region phase-change problems. *International Journal of Heat and Mass Transfer,* 30**,** 1709-1719.

VOLLER, V. R. & SWAMINATHAN, C. R. 1991. General Source-Based Method for Solidification Phase Change. *Numerical Heat Transfer, Part B: Fundamentals,* 19**,** 175-189.

VOLLER, V. R., SWAMINATHAN, C. R. & THOMAS, B. G. 1990. Fixed grid techniques for phase change problems: A review. *International Journal for Numerical Methods in Engineering,* 30**,** 875-898.

WANG, H.-X., CHEN, X., CHENG, K. & PAN, W. 2007. Modeling study on the characteristics of laminar and turbulent argon plasma jets impinging normally upon a flat plate in ambient air. *International Journal of Heat and Mass Transfer,* 50**,** 734-745.

WANG, H.-X., CHENG, K., CHEN, X. & PAN, W. 2006. Three-dimensional modeling of heat transfer and fluid flow in laminar-plasma material re-melting processing. *International Journal of Heat and Mass Transfer,* 49**,** 2254-2264.

WANG, J.-M., XU, P., YAN, H.-J., ZHOU, J.-M., LI, S.-X., GUI, G.-C. & LI, W.-K. 2013. Burner effects on melting process of regenerative aluminum melting furnace. *Transactions of Nonferrous Metals Society of China,* 23**,** 3125-3136.

WANG, J.-M., YAN, H.-J., ZHOU, J.-M., LI, S.-X. & GUI, G.-C. 2012. Optimization of parameters for an aluminum melting furnace using the Taguchi approach. *Applied Thermal Engineering,* 33–34**,** 33-43.

WANG, P.-J., TZENG, C.-C. & LIU, Y. 2010a. Thermal Temperature Measurements of Plasma Torch by Alexandrite Effect Spectropyrometer. *Advances in Optical Technologies,* 2010.

WANG, S., FAGHRI, A. & BERGMAN, T. L. 2010b. A comprehensive numerical model for melting with natural convection. *International Journal of Heat and Mass Transfer,* 53**,** 1986-2000.

WEBER, V., JARDY, A., DUSSOUBS, B., ABLITZER, D., RYBÉRON, S., SCHMITT, V., HANS, S. & POISSON, H. 2009. A Comprehensive Model of the Electroslag Remelting Process: Description and Validation. *Metallurgical and Materials Transactions B,* 40**,** 271-280.

WIDLUND, O., SAND, U., HJORTSTAM, O. & ZHANG, X. 2011. Modeling of Electric Arc Furnaces (EAF) with electromagnetic stirring. ABB Metallurgy.

WORD-ALUMINIUM. 2013. *International Aluminium Institute* [Online]. Available: http://www.world-aluminium.org Last accessed 11 Dec 2013].

WU, Y. K. & LACROIX, M. 1995. Numerical simulation of the melting of scrap metal in a circular furnace. *International Communications in Heat and Mass Transfer,* 22**,** 517-525.

XIHAI, L., WANG JUNQING, J. W., GAO JIANJUN, Z. L. & ZL, T. 2011. Simulation of electro-slag re-melting process of 120 t large ingot for nuclear power station and its application.

ZEIGER, H. & NIELSEN, H. 2004. Constitución y propiedades de los materiales de aluminio. *In:* HUFNAGEL, W. (ed.) *Manual del aluminio.* Reverté.

ZHANG, J.-Q., ZHOU, N.-J. & ZHOU, S.-H. 2012. Combustion and energy balance of aluminum holding furnace with bottom porous brick purging system. *Journal of Central South University,* 19**,** 200-205.

ZHANG, Y., BARR, P. V. & RAY MEADOWCROFT, T. 2008. Continuous scrap melting in a short rotary furnace. *Minerals Engineering,* 21**,** 178-189.

ZHOU, B., YANG, Y., REUTER, M. A. & BOIN, U. M. J. 2006. Modelling of aluminium scrap melting in a rotary furnace. *Minerals Engineering,* 19**,** 299-308.

ZHOU, N.-J., ZHOU, S.-H., ZHANG, J.-Q. & PAN, Q.-L. 2010. Numerical simulation of aluminum holding furnace with fluid-solid coupled heat transfer. *Journal of Central South University of Technology,* 17**,** 1389-1394.